Aero-Mechanical Coupling in a High-Speed Compressor

Scott C. Morris and Thomas C. Corke

Final Technical Report

by the
University of Notre Dame
Notre Dame, Indiana

for the
Air Force Office of Scientific Research
Contract No. FA9550-07-1-0166

UND-SM10-0338
February 2010

REPORT DOCUMENTATION PAGE

Form Approved
OMB No. 0704–0188

1. REPORT DATE *(DD–MM–YYYY)*	2. REPORT TYPE	3. DATES COVERED *(From — To)*
28–02–2010	Final	1 January 2007 — 30 November 2009

4. TITLE AND SUBTITLE

Aero-Mechanical Coupling in a High-Speed Compressor

5a. CONTRACT NUMBER

FA9550-07-1-0166

5b. GRANT NUMBER

5c. PROGRAM ELEMENT NUMBER

6. AUTHOR(S)

Scott C. Morris and Thomas C. Corke

5d. PROJECT NUMBER

5e. TASK NUMBER

5f. WORK UNIT NUMBER

7. PERFORMING ORGANIZATION NAME(S) AND ADDRESS(ES)

The department of Aerospace and Mechanical engineering
University of Notre Dame
Hessert Laboratory for Aerospace Research
Notre, Dame, IN 46545

8. PERFORMING ORGANIZATION REPORT NUMBER

UND-SM10-0338

9. SPONSORING / MONITORING AGENCY NAME(S) AND ADDRESS(ES)

Air Force Office of Scientific Research
875 N. Randolf Street
Suite 324, Room 3112
Arlington, VA 22203-1768

10. SPONSOR/MONITOR'S ACRONYM(S)

11. SPONSOR/MONITOR'S REPORT NUMBER(S)

12. DISTRIBUTION / AVAILABILITY STATEMENT

Approval for public release; distribution is unlimited.

13. SUPPLEMENTARY NOTES

The views, opinions and/or findings contained in this report are those of the authors and should not be construed as an official U.S. Government position, policy or decision, unless so designated by other documentation.

14. ABSTRACT

This report describes the results of several studies which sought to improve the understanding of coupling between the fluid and structures which are common in modern, high-speed axial compressors. There were two major areas of focus. The first was the development of measurement technique specifically for the study of these phenomena, termed Blade Image Velocimetry (BIV). The technique can measure fluid and structural velocity fields simultaneously and a demonstration of the utility of these measurements is provided for a flat plate undergoing flutter. The theory of the technique is presented with an empirically validated analysis of measurement error. The results of the application of BIV to a high-speed axial compressor are also presented. The second area of focus was the investigation of an isolated compressor blade in a high Mach number flow. The steady vibration amplitude, aerodynamic damping and impulse response were investigated. A complex interdependence was observed for these quantities for variations in flow conditions and blade structural properties.

15. SUBJECT TERMS

Fluid-structure interactions, turbomachinery, aeroelasticity, BIV, PIV

16. SECURITY CLASSIFICATION OF:			17. LIMITATION OF ABSTRACT	18. NUMBER OF PAGES	19a. NAME OF RESPONSIBLE PERSON
a. REPORT	b. ABSTRACT	c. THIS PAGE			19b. TELEPHONE NUMBER *(include area code)*
U	U	U	UU	96	

Standard Form 298 (Rev. 8–98)
Prescribed by ANSI Std. Z39.18

Contents

EXECUTIVE SUMMARY

This report describes the results of several studies which sought to improve the understanding of coupling between the fluid and structures which are common in modern, high-speed axial compressors. There were two major areas of focus. The first was the development of measurement technology specifically for the study of these phenomena. The measurement technique which was developed was termed Blade Image Velocimetry (BIV) and could measure fluid and structural velocity fields simultaneously. The BIV technique improved upon previous approaches in that a large amount of data could be acquired with a high degree of accuracy using a non-contact measurement system. The ability to characterize the structural dynamics of compressor blades using non-contact measurement technology is important because these structures are typically low mass and lightly damped. The result is that the dynamics of the blades are sensitive to sensors which must be physically attached. The second area was the investigation of the response of an isolated compressor blade in a high Mach number flow. The objective of this study was the characterization of the blade response at flow conditions which are similar to those found in modern compressors. The advantage to this approach was the ability to isolate the influence of parameters which would otherwise be obscured by a more complex system.

The BIV technique can acquire fluid and structural velocity fields simultaneously. These measurements can yield insight into the flow field which would be difficult to obtain using conventional approaches. A practical demonstration of this ability is presented for a flat plate undergoing flutter. The theory relating the structural velocity obtained by BIV to the modal amplitude of vibration is presented. A theoretical analysis of measurement error is also presented with the results of a series of bench-top validation experiments. Good agreement was found between the theoretical predictions and experimentally measured errors. The technique was also applied to a high speed axial compressor. The results indicated that BIV can obtain accurate estimates of blade tip velocity at realistic compressor operating speeds.

The response of a compressor blade in high Mach number flow was characterized by the blade vibration amplitude, aerodynamic damping and response to a mechanical impulse. The effects of angle of attack, Mach number, blade stiffness and tip gap were investigated. The results revealed a complex dependence upon all parameters investigated. It was observed that increases in blade stiffness reduce the steady vibration amplitude and the aerodynamic damping. The presence of an end-wall also reduced the amplitude of vibration and the aerodynamic damping. Finally, it was observed that the response of the blade to a mechanical impulse exhibited significantly higher damping than the estimated aerodynamic damping.

1 INTRODUCTION

This final report describes the results of a three-year effort at the University of Notre Dame involving the direct measurements of blade vibration in rotating and stationary experiments. The objectives were to develop and apply a new measurement technique, namely Blade Image Velocimetry (BIV), and apply this technique in order to further the understanding of aeroelastic phenomena in turbomachinery.

The fan and compressor sections of an engine are particularly susceptible to non-synchronous vibrations (NSV), where the frequency of the motions is not related to a multiple of the engine rotational frequency, or engine order. One reason for this is related to stage matching effects in multi-stage compressors. The operating point of the front stages during low and mid-speed opera- tion can deviate significantly from the aerodynamic design point, leading to part or full span stall (Day (1993)). Although the downstream stages of the compressor maintain overall system stability through these speeds, the stages that are subjected to transient stall can undergo significant unsteady blade forces and vibration. Accurate prediction of blade vibrations is clearly important in the design process, as well as for health management of deployed engines.

A simplified schematic of the major components constituting a single stage axial compressor are shown in figure 1. The gas passes through the inlet guide vanes, which set the incidence angle of the rotor blades. Energy is transferred to the flow as it passes through the rotor blades. The gas is discharged from the rotor to another set of stators (not pictured).

There are two fundamental types of dynamic aeroelastic interactions that can be distinguished based on the exchange of energy between the fluid and the structure. The interactions which result in the transfer of energy from the structure to the flow are referred to as aerodynamic damping. Aeroelastic excitation results in energy transfer from the flow to the structure. The aeroelastic excitation of compressor blades can arise from many sources. Figure 1(b) summarizes a few of these sources which are found in modern axial compressors. The source of aeroelastic excitation can be divided into two categories based on the fluid-structural coupling. The categories are forced excitation and self-excitation. The term forced excitation is intended to represent the unsteady forces applied to the compressor blades due to unsteady inflow conditions (e.g., wake passing) or outflow conditions (e.g., stator pressure disturbances). The term self-excitation refers to the aerodynamic loads that are implicitly dependent upon the motion of the blade. Under resonant-like conditions this usually referred to as blade flutter.

An example of forced excitation is the interaction between the rotor blades and the wakes from the stators. The stator wakes cause an unsteady loading of the rotors whose frequency is proportional to the shaft speed of the machine and the number of stators (the number of excitations per revolution, N, is referred to as the N^{th} engine order). Strong vibrations are expected to occur when the loading frequency coincides with a resonant frequency of a rotor blade. The relationship between the forcing and resonant blade frequencies as a function of compressor shaft speed are visualized using a Campbell diagram. An example of a typical Campbell diagram is shown in figure 2.

In a self-excited system, the aerodynamic excitation is implicitly dependent upon the motion of the structure. The conditions which result in this coupling depend on a variety of factors, such as fluid properties, blade material, flow velocity and blade geometry. An example is unsteady shock motion, commonly found in high-speed axial compressors. The motion of a blade (relative to its neighbors) alters the geometry of the flow passage between the blades. Changes in geometry alter the location of the passage shock and the aerodynamic load imposed on the blade. The change in load

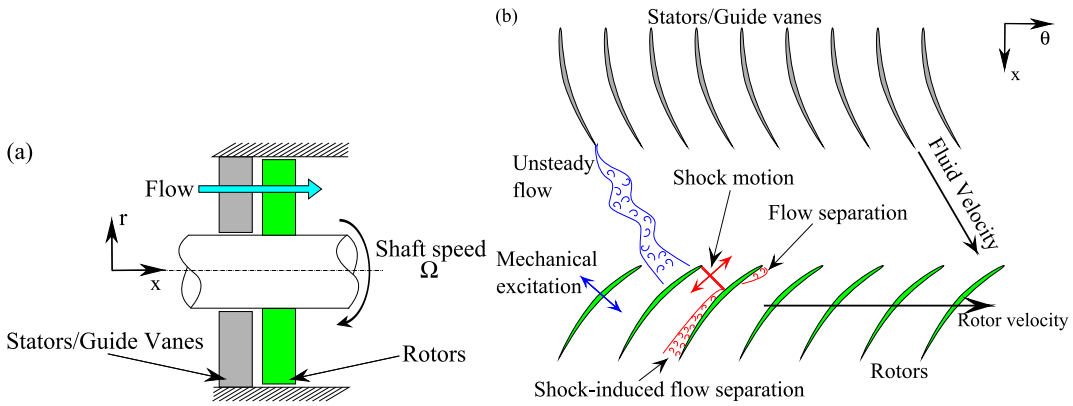

Figure 1: Sketch of a single stage axial compressor. (a) Sketch of an axial compressor cross-section. (b) Cascade representation of an axial compressor with potential sources of aeroelastic excitation.

causes the blade to vibrate and thus a feedback loop between the structure and the fluid is established. The result is a net transfer of energy from the fluid to the structure. Unless there is an external source of energy dissipation, such as structural damping, this energy transfer will continue to increase the blade vibration amplitude until failure. These types of interactions are classified as "flutter" and figure 3 shows regions where a particular compressor may be susceptible to these types of phenomena.

The aerodynamic damping of axial compressor blades is generally difficult to predict. The flow mechanisms which contribute to the dissipation of structural vibration energy can be similar to those which cause aeroelastic self-excitation. In modern axial compressors, aerodynamic damping is the dominant structural vibration energy dissipation mechanism. Therefore, an understanding of the mechanisms which result in aerodynamic damping is critical to accurate blade structural response predictions. The sparse knowledge base of aerodynamic damping of axial compressor blades, especially in the vicinity of the flutter boundary, has resulted in conservative blade designs and the avoidance of regions where flutter may occur.

A review of the current work regarding axial-turbomachinery aeroelastic studies will be presented in the following section. This will include a description of the current knowledge regarding aeroelastic behavior (from both experiment and simulation) as well as a review of the experimental methods. An overview of the research program completed under this project will then be presented. The objective of this program was be to expand the knowledge of the physics governing aeroelastic phenomena through the development of BIV in both stationary and rotating experiments.

1.1 A review of modern turbomachinery aeroelasticity

There are three main research fields in turbomachinery aeroelasticity. They are theoretical, numerical simulations and experimental measurements. Although this study will be focused on experimental aeroelasticity, it is useful to review the state of the art with respect to both theoretical and numerical simulations. Theoretical aeroelastic studies will be distinguished from numerical simulations by their use of relatively few analytic functions to describe the flow field. This is in contrast to numerical simulations where the entire domain must be discretized and a numerical solution found at every point.

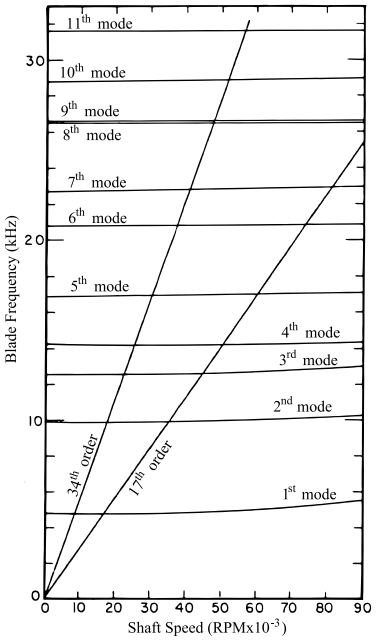

Figure 2: Campbell diagram for forced response of a rotor blade from 34 stators. From Japikse and Baines Japikse and Baines (1994).

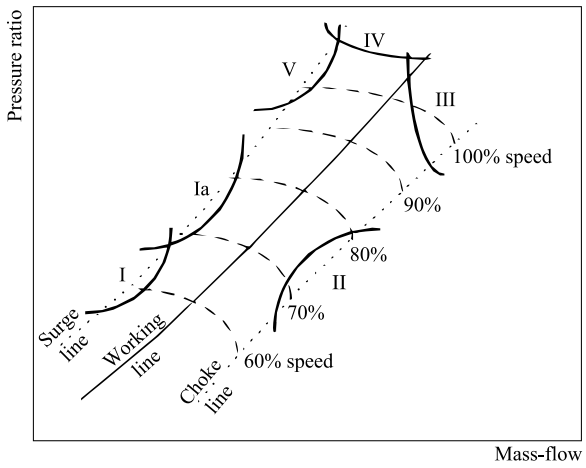

Figure 3: Axial compressor characteristic map with flutter regions. I. subsonic/transonic stall flutter, Ia. system mode instability, II. choke stall flutter, III. low incidence supersonic flutter, IV. high incidence supersonic flutter, V. supersonic bending flutter. From Marshal and Imregun Marshall and Imregun (1996).

1.1.1 Theoretical Studies

Theoretical aeroelastic studies represent the most fundamental aeroelastic analysis available for routine use. There are many necessary simplifying assumptions, but these analyses can yield predictive trends with minimal computational effort. The general approach will be discussed in this section along with a few examples and a discussion of their limitations.

There are two important aspects to a theoretical consideration of axial compressor aeroelasticity: the unsteady aerodynamics and the structural dynamics. The unsteady aerodynamics of an axial compressor are typically approximated by considering a cascade of airfoils, as shown in figure 3. The unsteady aerodynamic forces and moments are calculated by decomposing the flow field into a steady (with respect to time) component and an unsteady component. The analysis is simplified by assuming that the effect of the flow unsteadiness is small and thus linearizable. The blades are assumed to be vibrating with an identical motion (e.g. first bending) and a harmonic time dependence. However, adjacent blades can be vibrating out of phase. This phase difference is known as the interblade phase angle (IBPA). Solutions to the unsteady flow field are formulated within the framework of unsteady potential flow theory. The unsteady aerodynamics are handled by enforcing the Kutta condition and allowing vorticity to be shed from the airfoil trailing edge. This is done to account for changes in airfoil lift associated with the unsteady flow. The blade aerodynamics are approximated by a flat plate, however more complex shapes can be accounted for by yet smaller perturbations about this initial unsteady flow (cf. Atassi and Akai (1980), Akai and Atassi (1980)). Chapter 8 of Dowell (2005) and chapters 2-7 of Platzer and Carta (1987) provide a detailed account of theoretical turbomachinery aeroelasticity models.

The structure is typically assumed to be constructed from a linear-elastic solid with homogeneous, isotropic material properties. The structural dynamics are usually found using a Rayleigh-Ritz approach. In general, the blades are assumed to have no structural damping, such that the stability of the system depends upon the unsteady aerodynamics. Chapters 2-4 of Bisplinghoff et al. (1996) present a comprehensive review of these approaches for single wings and blades while chapters 13-15 of Platzer and Carta (1988) give an advanced discussion of theoretical structural dynamics in the context of axial turbomachinery. The coupling between the unsteady aerodynamics and structure dynamics is accomplished by LaGrange's equation. The generalized coordinates are typically associated with the structure, whereas the generalized forces/moments are associated with the unsteady aerodynamics. Chapter 19 of Platzer and Carta (1988) provides a detailed discussion regarding the formulation of the aeroelastic equations of motion for axial turbomachinery models of varying sophistication.

Flutter is addressed by examining the eigenvalues of the aeroelastic system for a harmonic blade motion. The boundary between stable aeroelastic response and flutter is defined as the locus of flow conditions for which there is a net transfer of energy from the flow to the structure over one cycle of vibration. At these particular flow conditions, the aeroelastic system is said to be unstable. Thus, fluid mechanisms which lead to flutter will be referred to as destabilizing, whereas mechanisms which suppress flutter will be stabilizing.

Note that theoretical models do not predict self-limiting behavior. The unsteady aerodynamic forces have a linear dependence on the amplitude of vibration. As a result, the amplitude of vibration grows unbounded once the blade is set to flutter. However, it is useful to examine the factors which tend to destabilize the aeroelastic system.

The reduced frequency, defined as

$$\omega^\star \equiv \frac{\pi f c}{U_\infty}, \tag{1}$$

is the ratio between the period of time required for a fluid particle to advect over 1/2 of the blade chord to the period of blade vibration. Here f is the frequency of vibration, c the chord of the blade and U_∞ is the free-stream fluid velocity. The reduced frequency plays a strong role in determining the stability of the compressor blade vibrations. Flutter tends to occur at low reduced frequencies ($O(0.1)$). Within the range of $10^{-2} \leq \omega^\star \leq 1$, the unsteady aerodynamic loads have a component which is in phase with the blade vibration velocity. As a result, there is a significant energy exchange from the flow to the structure within this reduced frequency range.

The interblade phase angle (IBPA) is also a strong determinant of system stability. Recall that the IBPA describes the relative phase difference in vibration between adjacent blades. The flow disturbance associated with the adjacent blade motion induces an unsteady load with a similar phase lag. The IBPA can vary from 0 to 2π in discrete angles only (due to the discrete number of blades). As a result, for every IBPA for which the induced loads contribute to the stability of the blade motion there is a corresponding IBPA where the loads are destabilizing. In practice, it is difficult to specify the IBPA of a rotor a priori. Therefore, the total damping for the individual blade must be sufficiently large to accommodate the induced loads due to adjacent blades at the least stable IBPA (cf. Chapter 19 of Platzer and Carta (1988)).

There is a fundamental dependence on the type of structural motion: plunging motions (translation normal to the blade chord) are typically more stable in low speed flow than pitching (rotation of the blade) motions. That having been said, the effect of a non-zero static imbalance*can either enhance or reduce system stability(Akai and Atassi (1980)). Finally, there are fundamental changes in the aeroelastic stability of the cascade as the Mach number increases(Verdon and Caspar (1984), Goldstein et al. (1977)). Specifically, the presence and motion of shock waves on the surface of the blade can be destabilizing for blade motion which would otherwise be stable for subsonic flow.

A disadvantage of theoretical aeroelastic studies is the linearization of the fluid dynamics. This approach is incapable of capturing strong nonlinearities such as separation (including airfoil stall and shock-induced) and large airfoil motions. Note that these theoretical studies capture well the mechanisms leading up to flutter, but it is pointed out that during flutter many of the assumptions are violated (such as the small unsteadiness). Numerical simulations have been developed over the last four decades to address these shortcomings. A summary of the general approach as well as a few studies will be presented in the next section.

1.1.2 Numerical Simulations

Numerical simulations, where the aeroelastic system is discretized in both space and time, have constituted a large area of research over the last few decades. This field of study has advantages over theoretical studies because its implementation requires fewer restrictive assumptions. A summary of a few approaches used in numerical simulations will be given along with some general trends. This section will conclude by presenting some of the known issues regarding these simulations.

Similar to theoretical approaches, numerical simulations must address the unsteady aerodynamics and structural dynamics. In addition, the discrete meshes associated with the fluid and structure must be coupled appropriately. The

*The chordwise separation between the center of gravity and the elastic axis

formulation of this coupling may not be trivial (Farhat et al. (1998)). The unsteady aerodynamics are usually simulated using a finite volume formulation and either an Euler or Unsteady Reynolds-Averaged Navier-Stokes (URANS) approach. It should be noted that Large-Eddy Simulation (LES) studies have been performed (Ferrand et al. (2006)), but the computational burden currently restricts their use to academic studies. The flow is typically split into a nonlinear steady component and a linearized unsteady component (Marshall and Imregun (1996)), however fully nonlinear analyses are becoming more common.

The structural dynamics are simulated using a Finite Element Method. The incorporation of the structural dynamics into the aeroelastic system is accomplished by considering a small set of free-vibration modes with an assumed harmonic time-dependence. The fluid mesh is typically deformed using an algebraic dependence to account for blade motion. There are two approaches used to address the time-evolution of the spatially discretized aeroelastic system. One approach is to discretize the system in time and integrate the equations of motion. This approach is the most general way to attack the problem, but requires that a large amount of data be stored. Another approach assumes that the flow variables have a harmonic dependence in time but are allowed to vary in space (Chen et al. (2002)). Using this approach, the flow variables can be approximated by a spatially varying fourier series in time, thus substantially reducing the computational effort (Hall et al. (2002)).

The most significant result of the application of numerical simulations is the identification of self-limiting aeroelastic behavior in axial compressors. This is a direct result of the nonlinear approach (Hall et al. (2002), Sanders et al. (2004)). There are several mechanisms which can lead to self-limiting behavior. The periodic stalling of airfoils in a cascade (an effect of rotating stall, cf. Hoying et al. (1999) and Cameron (2007)) can result in amplitude-limited, quasi-periodic blade vibrations (Abdel-Rahim et al. (1993)). The interaction between shocks and the boundary layer is another mechanism which can lead to limit cycle oscillations. Shocks are generally destabilizing for blades undergoing bending oscillations, but tend to be stabilizing for torsional motion. However, shock induced flow separation tends to destabilize the torsional oscillations (Vahdati et al. (2001), Thermann and Niehuis (2006), Hall et al. (2002)). Finally, the interaction between adjacent blade rows can significantly influence the stability of the cascade (Hall and Ekici (2005)).

Although numerical simulations offer a substantial amount of insight regarding the physics of self-limiting behavior of aeroelastic phenomena, there are still many areas which require improvement. The single largest issue is the accurate simulation of viscous effects. The unsteady aerodynamics are dependent upon accurately capturing the effect of turbulence and boundary layer separation, yet even steady flow simulations which are routinely used for aeroelastic studies cannot reliably predict these phenomena (Grüber and Carstens (2001), Thermann and Niehuis (2006)). The result is that simulations are performed as a postprocessing step as a supplement to experimental measurements (Sanders et al. (2004)). At the present time, it is unfeasible to routinely execute simulations which can resolve the nonlinear viscous effects which characterize self-limiting behavior in axial compressors. Consequently, there is a strong demand for experimental characterization of the nonlinear aspects of the axial compressor aeroelastic system.

1.1.3 Experimental aeroelasticity of axial compressors

Experimental studies of axial compressor aeroelasticity can yield much insight of the physics without the need for simplifying assumptions. However, successful implementation currently requires large investments in both time and equipment. This high cost has been the primary motivation for both theory and numerical simulations. It should be

noted that the current limitations of the previous two approaches implies that the successful development of an axial compressor may require multiple experimental investigations to identify and suppress potentially dangerous aeroelastic resonances which were not previously predicted (Srinivasan (1997)).

There are two main areas of research in experimental axial compressor aeroelasticity. These are the development of new measurement technology and the experimental investigations. The need for new measurement technology is motivated by the complex aeromechanical environment in which modern axial compressors operate. Experimental investigations are critical to aeromechanical design validation. These studies can reveal aeroelastic excitation which are not predicted using theoretical or numerical models. The remainder of this literature review will focus on recent developments in these two areas of research.

1.1.4 Experimental Methods

The complex aeromechanical environment which characterizes modern axial compressors necessitates specialized measurement technology. Specifically, measurements must characterize the dynamics of a system where the structure has both a low mass and low internal damping, rotating at high speed and is operating in a highly unsteady, generally nonlinear aerodynamic environment. There are two aspects of this system which need to be characterized by measurements. They are the unsteady aerodynamics and the structural dynamics. The technology associated with both structural dynamics measurement and unsteady flow can be classified based upon the method by which measurements are made. Two categories will be distinguished: direct and non-contact. Direct measurement technology will be considered as technology where the sensor is in direct contact with the system to be measured. Hot wires/films, pressure transducers, strain gages and accelerometers are examples of direct measurement technology. Particle Image Velocimetry (PIV), Laser Doppler Velocimetry (LDV) and Blade Tip Timing (BTT) are examples of non-contact measurement technology. Although there are many measurement technologies which have been applied to axial compressors, this review will only focus on four. They are surface-mounted pressure transducers, strain gages, Blade Tip Timing (BTT) and Particle Image Velocimetry (PIV). The first three represent the most common measurement techniques used in experimental compressor aeroelasticity. The last technique, PIV, is included because it has specific abilities which make it an ideal measurement system for aeroelastic studies. A brief discussion of these measurement techniques in the context of axial compressor aeroelastic measurements will be the topic of this section.

The measurement technology for unsteady flow has been developed extensively. Sieverding et al. (2000) presents a review of conventional direct measurement technology while chapter 14 of Tropea et al. (2007) provide a detailed review of both direct and non-contact flow measurement technology. In the context of experimental aeroelastic studies, the most popular unsteady flow measurement technology is high frequency surface mounted pressure transducers (cf. chapter 9 of Platzer and Carta (1987) and chapter 20 of Platzer and Carta (1988), Gill et al. (2004), Buffum et al. (1996), Kobayashi Kobayashi (1990) and Belz and Hennings (2006)). The sensors are characterized by their small size and high frequency response. They are typically recessed into the surface of the compressor blades so as to mimic the original aerodynamics. The advantage of this approach is that a direct measurement of unsteady pressure distribution (as well as forces and moments) can be obtained in a time-resolved manner. However, there are a number of disadvantages. Spatial resolution of the unsteady blade surface pressure is limited by the physical size of the pressure transducer/pressure taps. The information available only characterizes the behavior of the flow in the vicinity of the blade surface. Although this is

useful in predicting aeroelastic stability, it may not yield much information regarding the source of the surface pressure fluctuations. The application of surface mounted pressure transducers to rotating structures requires that both power and data be transmitted between a stationary data acquisition system and the rotating sensors. Traditionally, this is accomplished through slip-rings, although wireless approaches are becoming more popular. Finally, the installation of these sensors on a flexible blade can alter the structural dynamics. This can influence the measured unsteady pressure distribution.

Particle Image Velocimetry (PIV) is a non-contact measurement technique which is typically used for obtaining planar velocity fields of fluids (Raffel et al. (2007)). The technique utilizes a specialized CCD camera and a laser to estimate the displacement of particles dispersed in the fluid flow. The displacement of the particles between two images acquired by the CCD camera divided by the time lag between the first and second image yields an estimate of the flow velocity. This technique has been used to successfully characterize the quasi-steady axial compressor flow environment (cf. Wernet (1997), Gorrell and Copenhaver (2006) and chapter 14 of Tropea et al. (2007)), primarily because of its ability to acquire a large amount of flow velocity information in a non-intrusive manner with minimal equipment (in most cases the only sensor to be calibrated is the CCD camera). Despite these advantages, it has not been widely integrated into axial compressor aeroelastic studies. The proposed research will utilize PIV as the primary measurement technique to investigate the physics behind self-limiting aeroelastic oscillations. In the next chapter, a method will be presented which allows for the acquisition of simultaneous fluid and structure velocity estimation using a conventional single camera PIV system.

In contrast to flow measurement technology, there are few techniques available for the characterization of the structural dynamics of axial compressors. The review article of Al-Bedoor (2002) provides a survey of the current technology applied to blade vibration measurement. The most common direct measurement technology is the strain gage. Similar to surface pressure transducers, the sensors are typically recessed to preserve the aerodynamic shape of the blade. Few sensors are necessary to deduce the entire motion of the blade. This technology remains attractive because it represents the most reliable approach to obtaining accurate, time-resolved measurements of the blade motion. The drawbacks of this approach are similar to those found with the surface pressure measurements. Specifically, the transmission of power and data between the rotating sensor and stationary data acquisition system is not trivial. In addition, the machining required to recess the gages to be flush with the surface of the blade can change the structural dynamics.

Blade Tip Timing (BTT) is a non-contact structural vibration measurement technology which has gained popularity over the last 40 years. Heath and Imregun (1998) and Lawson and Ivey (2005) provide a detailed description of this measurement technique. The concept of measurement will be summarized briefly. A set of proximity sensors are installed into the outer casing in a circumferential pattern. The proximity sensors can either be capacitive (Lawson and Ivey (2005)) or optical (Zellinski and Ziller (2000)). The sensors are installed such that they detect when a blade tip passes by the sensor location. The average time required for a blade tip to move from one sensor location to another is known by the shaft speed of the rotor, the radius of the rotor at the tip and the circumferential distance between the two sensors. Any deviations from this average time indicates blade motion with respect to the hub. The advantage of this method over conventional strain gages is that the rotor does not need to be modified and installation only requires a few holes to be drilled in the outer casing. The output from this measurement system is a time-series of blade tip displacement.

The sampling frequency of the method depends on the shaft speed of the compressor and the circumferential separation of the sensors. The sampling frequency is typically much lower than the frequency of blade vibration, and as a result modes are distinguished by observing their aliased frequencies (Zellinski and Ziller (2000)). One unique issue with this measurement system is the difficulty in obtaining amplitude and frequency estimates when the blade vibration frequency is an integer multiple of the shaft speed (a condition known as synchronous resonance). Data processing algorithms based on linear regression principles have been proposed to overcome this limitation (Heath (2000), Gallego-Garrido et al. (2007)). The accuracy of the vibration amplitude measurement can be comparable to strain-gage measurements under controlled circumstances (Lawson and Ivey (2005)). However, the presence of noise as well as the assumptions used in data processing can reduce the accuracy substantially)Carrington et al. (2001), Lawson and Ivey (2005)).

1.1.5 Experimental Studies

The remainder of this literature review will focus on several case-studies of axial compressor aeroelastic stability. These case studies will elucidate flow mechanisms which contribute to the overall stability of the blade vibrations. The studies were performed with the objective of determining the flow mechanisms which can lead to blade flutter. Knowledge of the interaction between these mechanisms and the blades will help yield insight into the origins of the experimentally-observed self-limiting behavior once a blade is set to flutter.

An example of a complete aeroelastic investigation of an axial compressor rotor operating at high Mach number and high incidence was presented by Stargardter in chapter 20 of Platzer and Carta (1988). This type of flutter occurs in regions I and Ia of figure 3. The following observations can be made regarding this particular form of flutter. Blade flutter manifests itself as a high amplitude oscillatory vibration whose frequency is usually not an integer multiple of the rotor shaft speed. The blades are excited in the first torsion mode. Flutter is typically preceded by stall-induced aeroelastic oscillations. These stall-induced oscillations, commonly known as buffeting, have a random amplitude and excite the first bending mode of the blades. The distribution of aerodynamic forcing is concentrated near the leading edge on the suction side of the blades. It is observed that this type of flutter requires that supersonic flow exist over some portion of the blade, suggesting that shocks which oscillate in both strength and chordwise position are present during flutter. Finally, it was observed that flutter occurred only for a narrow range of reduced frequencies.

Kobayashi (1990) studied the aeroelastic response of an annular cascade in transonic flow. The blades were forced to oscillate in first torsion about the mid-chord. This investigation was concerned with the effects of reduced frequency, inlet Mach number and interblade phase angle on the unsteady aerodynamic forces observed on the blades. In contrast to the study by Stargardter, Kobayashi was concerned with the physics of supersonic unstalled torsional flutter, a condition which is characterized by high operating speed and low compressor backpressure (region III of figure 3). A common feature of this system is the presence of a shock whose chordwise position along the suction side of the blade oscillates in time. The mean location of this oscillating shock was aft of the torsional axis of rotation. Measurements of unsteady surface pressure indicate that the suction side aft of this axis and the pressure side upstream of this axis were responsible for the unstable aerodynamic forcing, whereas the rest of the airfoil surface was stabilizing. The effect of changing the reduced frequency of the airfoil oscillations significantly influenced the aerodynamic forcing on the suction surface. Increasing the reduced frequency tended to increase the stability of the aeroelastic system. This was attributed to a decrease in the magnitude of the shock oscillations associated with high frequency pitching oscillations.

Buffum et al. (1996) also studied the stability of torsional oscillations of a cascade. However, the inlet Mach number was much lower than the previous two studies (M=0.5). The effect of mean incidence angle were investigated for a constant interblade phase angle of 180^o. There was a region of separated flow extending from the leading edge to about 30% chord along the suction side of the blades. This separation region resulted in strong aerodynamic forcing of the blades. The largest contribution to the unstable forcing of the blade occurred within the separation region near the leading edge. In contrast, a stabilizing forcing was observed in the region where the flow reattached. The effect of increasing the reduced frequency was to magnify the forcing. In general, this caused a decrease in cascade stability. This study indicates that the unsteady flow associated with the initial separation point can have a strong destabilizing effect.

Srinivasan (1997) presents a review of many turbomachinery aeroelasticity case studies. Similar to the work of Stargardter, the emphasis is on the complete aeroelastic system in the context of industrial design. There are a few mechanisms associated with the structural dynamics which may contribute to the self-limiting behavior of compressor blades. The first is the disk mistuning, whereby the frequencies of vibration of adjacent blades for a given blade vibration mode are not identical. If done correctly, the intentional mistuning of a rotor can increase the stability of the system. The overall effect is to decrease the influence of the interblade phase angle on the aeroelastic stability of the blade vibrations. It should be noted that optimal mistuning will yield a rotor whose stability is governed by the stability of the individual blades. However, mistuning can result in inordinately large vibrations due to forced response. External sources of damping (such as Coulombic damping associated with sliding solid surfaces) can be an important (although nonlinear) source of energy dissipation.

Belz and Hennings (2006) studied the effect of reduced frequency on the stability of torsional oscillations in a transonic annular cascade. The investigation considered two flow conditions which resulted in substantially different shock structures. A transonic reference case had a passage shock which extended from the leading edge of the pressure side to between 25% and 35% chord on the suction side. The flutter case, in which the inlet Mach number was increased slightly, resulted in a passage shock at 25%-35% chord on the pressure side and 65%-85% chord on the suction side. In both cases, the shocks were observed to be both stabilizing and destabilizing, dependent upon the interblade phase angle and the surface of the airfoil on which they acted. For the transonic reference case, it was found that the shock had a stabilizing influence on the pressure side but a slight destabilizing influence on the suction side. The transonic reference case was stable. In contrast, the intersection of the shock on the suction side for the flutter case was consistently responsible for the destabilization of the cascade. This configuration was most unstable when the interblade phase angle was around 90^o.

There are two aeroelastic phenomena common to the case studies presented here. In general, the flutter of axial compressor blades is determined by the interaction of shocks and flow separations. Although the behavior of these mechanisms are known up to the point of flutter, relatively little is known about the interaction of these mechanisms beyond the flutter boundary. It is probable that these mechanisms are partially responsible for the self-limiting behavior which has been observed in axial compressors. A detailed understanding of the physics responsible for this self-limiting behavior may yield useful insight information regarding the aeromechanical design of compressor blades for flutter resistance.

1.2 Research Outline

The motivation for this research program was to improve the understanding of the aeroelastic phenomena which influence the dynamics of the modern compressor. An understanding of these phenomena will lead to more accurate prediction of blade structural loads with improvements in compressor performance, durability and efficiency. A review of the literature has shown that the aeroelastic interactions of compressor blades near their design point can be estimated fairly well by a number of approaches, including semi-analytic theories and numerical simulations. However, the non-linear interactions between the flow and the blades which occur at off-design conditions are difficult to predict and poorly understood. These non-linear interactions, such as unsteady shock motion and flow separation, can either excite or damp blade vibrations. An understanding of these interactions are of critical importance in predicting the unsteady blade loads at off-design conditions. The degree to which these interactions excite or damp blade vibrations depend upon many factors, such as the Mach number, angle of attack and the eigen-modes of blade vibration.

The objectives of this research program were met by developing BIV specifically for the empirical characterization of the non-linear aeroelastic interactions typical of modern axial compressors, and to apply these technologies to several canonical systems. The systems which were studied were designed to isolate the effects of various aspects common to modern axial compressors, such as compressibility, three-dimensional flow and annular cascade effects.

The Blade Image Velocimetry (BIV) utilized equipment common to PIV systems and is capable of measuring both fluid and structural velocity simultaneously. This capability is critical in the characterization of the non-linear aeroelastic system typical of modern axial compressors because of the coupled nature of the fluid and structure. Section 2 describes the fundamental theory of the BIV technique, a practical demonstration of the simultaneous acquisition of fluid and structural velocity, and the experimental validation of the error analysis. Section 3 describes the practical implementation of the BIV technique to the measurement of rotor blade vibration on a transonic axial compressor. Included in this section is a discussion of a few issues that are unique to the application of BIV to high-speed turbomachinery.

An investigation of the aeroelastic response of an isolated compressor blade at high Mach number is presented in section 4. This investigation studied the effect of Mach number, angle of attack, blade stiffness and tip gap on the amplitude of blade vibration and the effective aerodynamic damping. The response of the blade to a mechanical impulse was also investigated. The study of the interactions between the blade and non-linear flow structures of a canonical system can provide insight into the fundamental physics which would otherwise be obscured by a more complex system.

2 FUNDAMENTALS OF BLADE IMAGE VELOCIMETRY

2.1 Introduction

The majority of experimental turbomachinery aeroelastic studies use vibration sensors which must be directly affixed to the structure. These sensors can yield time-resolved, accurate estimates of the blade vibration amplitude. However, their implementation is not trivial. Specifically, the transmission of both power and data between a stationary data acquisition system and a rotating sensor must be addressed. Additionally, the modification of the fluid and structural dynamics of the blade must be addressed. The use of non-contact measurement systems can negate most of the effects. However, the non-contact techniques currently employed in axial compressor structural dynamics studies can be inaccurate. Therefore, as part of this research program, a new measurement technique has been developed to address this problem.

A technique is presented for simultaneous measurement of fluid velocity and structural vibration using standard Particle Image Velocimetry (PIV) equipment. The CCD camera was focused on particles in the flow as well as surface features on the free end of a cantilevered beam. This non-contact approach to measuring structural velocity enables acquisition of these data on rotating and translating structures. The development of this technique was motivated by the need for accurate, non-contact blade vibration measurements in turbomachinery. Measurements of blade vibration amplitude on the rotors are both critical to engine aeromechanical design validation and are difficult to obtain. The simultaneous acquisition of fluid velocity will provide information about the aerodynamic forcing and aerodynamic damping of the blade vibratory motion. Since the objective of the technique was to obtain blade velocities using digital images, the technique is referred to as Blade Image Velocimetry (BIV). This paper will focus on the advantages, limitations, and uncertainty of BIV. The present implementation of PIV for fluid velocity is standard, and will only be considered in the context of combined BIV/PIV measurements.

Vibration measurement techniques can be broadly categorized as either contact or non-contact. Contact measurement techniques utilize sensors which are directly attached to the vibrating structure such as accelerometers and strain gages. These sensors can modify the dynamics of the structure and an individual sensor can only measure structural motion at one spatial location. Measurements on rotating structures typically require telemetry or slip rings in order to record the data on stationary acquisition systems. Non-contact measurement techniques such as Laser Doppler Vibrometry (LDV) (Bell and Rothberg (2000), Claveau et al. (1996)) and fiber optic interferometry (Dib et al. (2004), Alayli et al. (2004)) do not influence the dynamics of the system. These techniques can be "scanned" in order to obtain the spatial information that is required to estimate the amplitude of various eigenmodes of the vibration. These methods are not well suited for measurements on rotating structures given that they yield information at a small number of spatial locations only when there is a clear line of sight between the sensor and the structure. The accurate determination of three-dimensional structural motion using these data can be difficult. Harris and Piersol (2002) provide a review of various vibration measurement techniques.

Digital Image Correlation (DIC) is a general technique that utilizes two successive images of a structure or flow field in order to estimate displacement. The method often partitions the image into interrogation zones for which a spatial correlation algorithm is applied. This results in a two-component displacement vector in the plane of the image at each interrogation zone. The displacement is related to the velocity field by the time difference between the images (Raffel et al. (2007)). The implementation of DIC for both static and dynamic strain measurements has been reviewed by Hild

and Roux (2006).

Photogrammetry is another technique which estimates structural displacement from images. The similar technique, Videogrammetry, is the Photogrammetric technique applied to a time series of images (Pappa et al. (2003)). Photogrammetry is often used to reconstruct three dimensional motion from two-dimensional images. The technique measures the motion of a few markers whose locations with respect to the camera are known. The mapping between the measured two-dimensional displacement (seen by the camera) and the three-dimensional model deformation is determined by calibration (Burner et al.). The fundamentals of Photogrammetry have been reviewed by Liu et al. (2000), Pappa et al. (2003) describe some practical examples related to aerospace applications.

Previous measurements have been made that obtain simultaneous acquisition of fluid and structural velocity using a correlation based approach. For example, Breuer et al. (2001) used a standard PIV system to obtain fluid and structural displacement on a silicon microturbine. The extremely small size precluded the use of conventional vibration measurements. The structural motion was obtained by tracking the the intersection of the PIV laser light sheet with the surface of the blade. DIC algorithms were used to estimate the degree of rotor whirl from these data. Gomes and Lienhart (2006) also utilized PIV equipment to measure structural velocity. Their objective was to obtain a set of high fidelity measurements for aeroelastic code validation. The structural velocity measurement was similar to that employed by Breuer *et al.* In both cases, the features used in the correlation algorithms were generated from the intersection of the laser light sheet and a solid surface.

The main difference between the techniques discussed and the present BIV measurements is the application of a small paint "dots" to the structure in order to mimic the seeding images that are typically found in conventional PIV measurements. This allowed standard correlation algorithms to be employed in order to determine the structural velocity. There are a number of advantages to this approach. First, the BIV provides a spatial distribution of structural and fluid velocity simultaneously (in a plane). Secondly, the PIV algorithms are convenient to use and provide an extremely accurate estimate of the true structural velocity. These measurements were acquired at a relatively low temporal frequency, and so the technique is fundamentally different from point measurements of strain or vibration velocity where high frequency time series data are recorded. However, the measured spatial distribution of structural position and velocity allows for the determination of the instantaneous amplitude of the vibration modes when a priori knowledge of the the three-dimensional eigen-mode shapes is available.

A description of the general implementation of combined BIV/PIV will be presented in the following section along with a demonstration which shows the aeroelastic response of a flat plate in incompressible flow. This will be followed by a detailed analysis of the accuracy of the PIV algorithms for measuring the structural velocity. The calculations used for the determination of the modal amplitude as well as the associated uncertainty analysis will then be provided. This will be followed by an experimental validation of BIV using a conventional scanning LDV system with harmonic forcing.

2.2 PIV/BIV implementation

2.2.1 Aeroelastic demonstration of simultaneous PIV/BIV

Implementation of the BIV technique used a standard single camera PIV system Raffel et al. (2007). A schematic of the setup used in the present experiments is shown in Figure 4. The model shown is a cantilevered beam which nominally

represents a generic axial compressor blade geometry.

The coordinate system is defined by the x, y and z vector directions that are oriented in the chord-wise, span-wise and blade normal directions, respectively. A dual-cavity Nd:YAG laser light source was focused into a 1 mm thick light sheet in order to illuminate the fluid plane of interest. The sheet was oriented at a small angle relative to the tip plane such that the tip was illuminated. Note that if the camera can not focus on the fluid plane of interest and the blade tip at the same time, a two-camera system would need to be employed. A random pattern of matte white paint "dots" were applied to the tip of the cantilevered beam. This pattern was designed to mimic that of a seeded flow typical of conventional PIV so that the same vector calculation algorithms could be employed without modification. The CCD camera was synchronized to the laser trigger to obtain two consecutive images of the vibrating blade and seed particles in the fluid. Standard correlation algorithms were then used to obtain the velocity field contained in the image that included both the fluid motion and the blade tip motion.

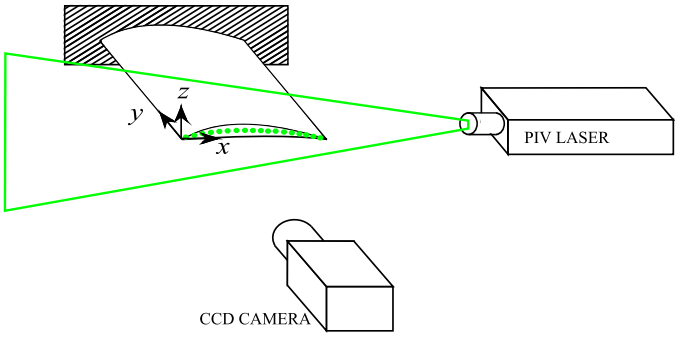

Figure 4: Sketch of a stationary "blade" and measurement points.

The simultaneous acquisition of fluid and structural velocity fields was demonstrated using a thin flat plate undergoing flutter. The 6061-T6 aluminum plate had a thickness of 0.50 mm, a chord of 78 mm, and a span of 189 mm. The plate was positioned in the test section of an open jet wind tunnel at a nominal angle of 20° relative to the incoming flow. The free-stream fluid velocity was 12 m/s. This resulted in large amplitude oscillations of the plate. The frequency of oscillation was obtained from a conventional Laser Doppler Vibrometer (LDV) system, and was found to be 53 Hz. The reduced frequency, defined by $\omega^\star = \pi f c/(U_\infty)$, was 1.08 where c is the chord length, f is the frequency of oscillation, and U_∞ is the free stream velocity. The CCD camera field of view was 84×84 mm resulting in a spatial resolution of 24.3 pixels/mm. The camera was calibrated using a standard PIV calibration plate using a 3$^{\text{rd}}$ order polynomial fit with an RMS of ≈ 0.08 pixel.

Figure 5 shows a sample image acquired by the PIV camera as well as the computed velocity vectors. The x'-z' coordinates are oriented such that the free-stream fluid velocity is in the x' direction. The vectors representing the structural velocity (colored red) are scaled by a factor of 50 with respect to the fluid velocity vectors. All images were processed using LaVision's DaVis software suite. The images were first filtered using a Sobel edge detection filter. Local intensity fluctuations were minimized using a sliding background subtraction algorithm. The BIV calculation consisted of a three iteration multipass approach using progressively smaller square windows. The interrogation windows used on the first pass were 64×64 pixels in size weighted with an axisymmetric Gaussian weighting function (the weighting function had no preferential direction with respect to the image). The overlap between interrogation windows was 50%.

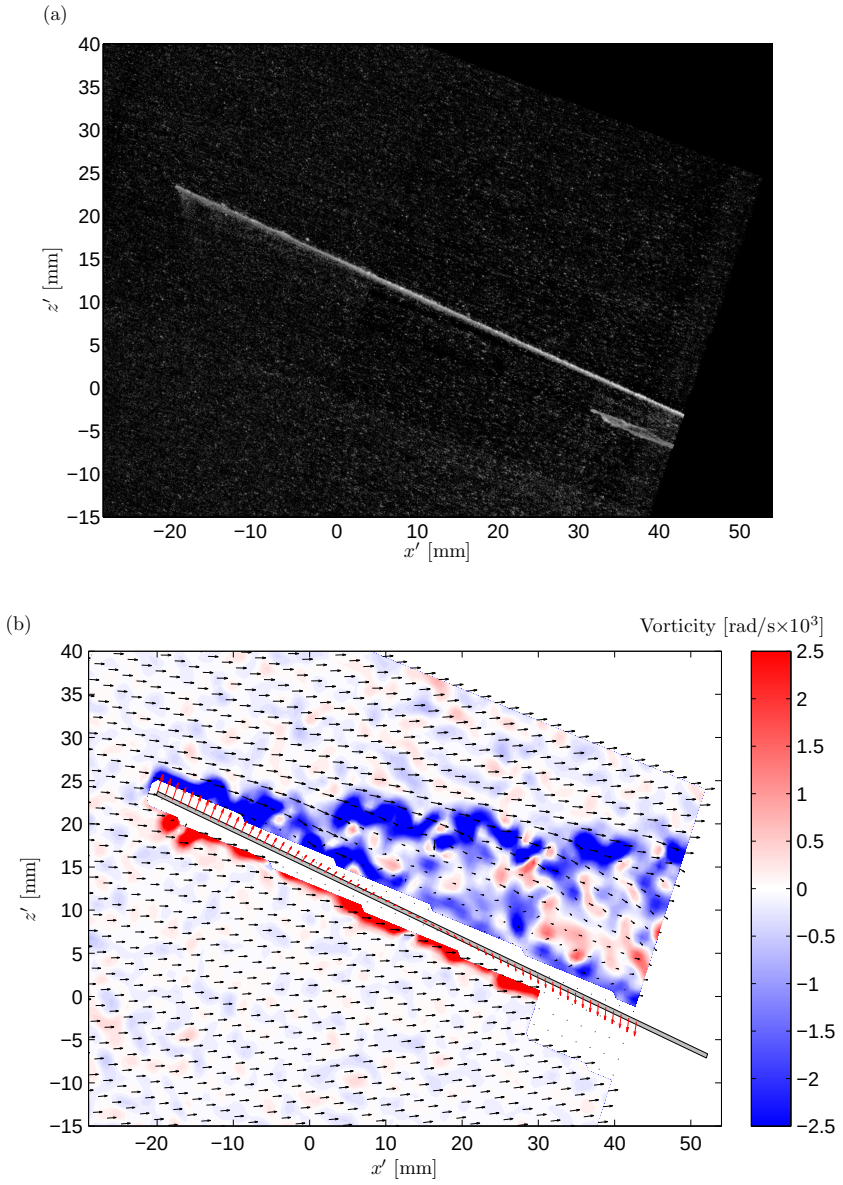

Figure 5: (a) Image of seeded fluid and structure for combined BIV/PIV measurements. (b) Computed velocity and vorticity field. → fluid velocity; → structure velocity ×50; contours indicate fluid vorticity.

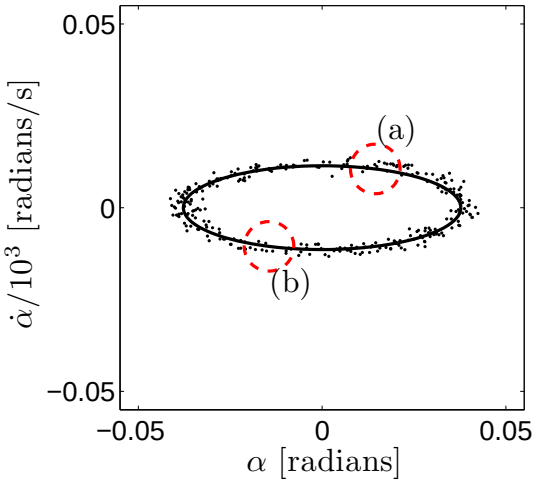

Figure 6: Phase space behavior of the flat plate subject to uniform flow. Points marked represent phase-state locations used in figure 7.

The last two passes utilized 32×32 pixel windows with an axisymmetric Gaussian weighting function and a Whittaker image reconstruction on the final pass. This resulted in a vector resolution of 1.5 vectors/mm. Note that in figure 5(b) every 4^{th} fluid velocity vector and every 3^{rd} structure velocity vector are displayed for clarity.

Vector validation allowed a maximum vector velocity that was set to 3 times greater than the maximum anticipated tip velocity and a minimum correlation peak ratio (for a given window, the ratio of the highest correlation peak had to be at least 1.3 times greater than the second highest correlation peak). Lastly, a median filter (velocity vectors which deviate by more than 2 standard deviations of their neighbors were rejected) and a single smoothing operation were applied. For a brief introduction to these processing operations, the reader is referred to chapters 5 and 6 in Raffel et al. (2007).

The BIV/PIV image pairs were acquired at 1 Hz. The low sampling rate with respect to the frequency of the structural vibration (53 Hz) implies that each velocity field obtained by combined BIV/PIV was an independent realization. However, dynamic information can be obtained by phase averaging the velocity measurements with respect to the blade motion. The phase-state of the vibration was determined by measuring the angle of the blade with respect to the approach flow as well as the angular velocity of the blade. The angle of the blade tip was determined from a single blade image. The angular velocity was derived from the velocity measurements. A phase-space type diagram of 300 realizations of the structural motion is shown in figure 6. The resulting limit cycle shown is approximately elliptical. The solid ellipse shown in the figure represents a phase averaged representation of the quasi-periodic blade motion. The major and minor axes represent the amplitude of the phase-averaged angular displacement and velocity, respectively. The ratio of the major axis to the minor axis of this ellipse yields an estimate for the frequency of vibration, and was found to be 48 Hz.

The phase-averaged velocity and vorticity fields at two points in the response are shown in figure 7. An isocontour representing velocity magnitude of 11 m/s is shown in order to illustrate the spatial extent of the wake. In figure 7(a), the plate is shown pitching upward and the general structure of the flow field is similar to the instantaneous measurement presented in figure 5(b). Note that the velocity field shown is a planar section of a highly three dimensional flow at the tip of the plate. The velocity shows a separation point at $\approx 30\%$ chord (as measured from the leading edge). The

isocontour shows that the separation region grows in the chord-normal direction as the flow progresses downstream. Aft of 50% chord, the isocontour becomes nearly parallel to the free-stream velocity.

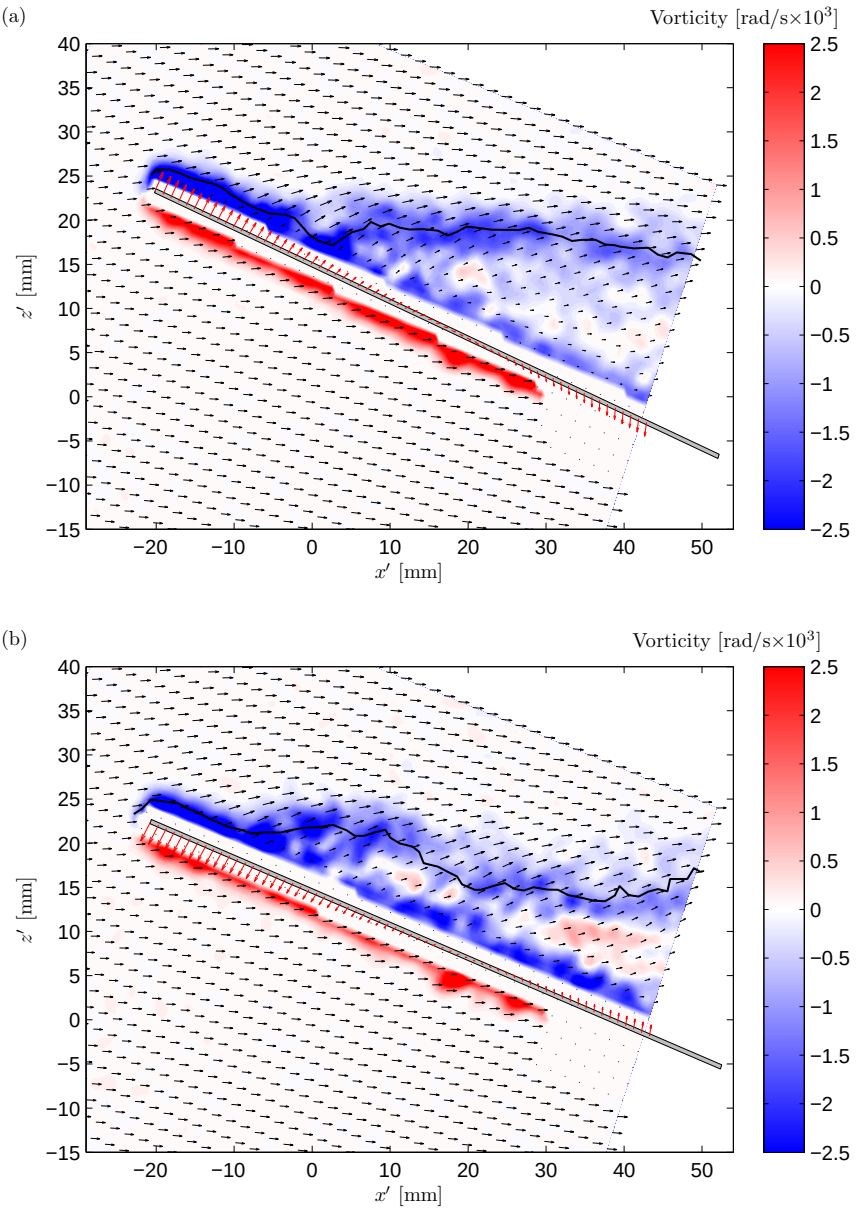

Figure 7: Phase averaged flow around a blade undergoing aeroelastic oscillations. See figure 6 for the corresponding locations in phase space. → fluid velocity; color contours represent vorticity; → structure velocity ×50; − isocontour of $\sqrt{U_{x'}^2 + U_{z'}^2} = 11$ m/s; (a) $\alpha \approx 0.0145$ rad, $\dot{\alpha} \approx 10.5$ rad/s; (b) $\alpha \approx -0.0144$ rad, $\dot{\alpha} \approx -10.5$ rad/s.

There are significant differences in the flow field as the plate pitched downward (figure 7(b)). The separation point moved forward to approximately 15 percent of the chord, and two regions within the wake were observed. Specifically, the isocontour is nearly parallel to the blade over the mid section of the chord, and nearly parallel to the free stream direction near the trailing edge. Analysis of the full cycle of the phase-averaged response revealed an interesting dynamic between the plate and the fluid. As the plate pitches upward (figure 7(a)), the separation point retreats toward the trailing edge and the chord-normal extent of the wake grows. A new separation region then forms upstream of the pre-existing wake

region as the plate begins to pitch downward. The new separation region grows until the lowest angle of attack is reached. A video illustrating the phase-averaged velocity field over the entire limit cycle is available from the authors[†]

Figures 5 - 7 demonstrate that significant insight into fluid-structure interactions can be obtained using the BIV/PIV technique in aeroelastic flows. The following section will focus on the accuracy of the structural velocity measurements using the PIV hardware. This will be followed by a description of the mathematics and uncertainty related to using the BIV measurements to estimate the discrete modal amplitudes.

2.2.2 Uncertainty in Structural Velocity

The accuracy of the structural velocity measurements was evaluated experimentally using harmonic forcing of the structure. A blade-like geometry was utilized in which the natural frequency of the first torsional mode was 782 Hz. Details of the geometry and mode shapes are provided in Section 3.3.2. A Laser Doppler Vibrometer (LDV) was used as a reference sensor that was assumed to provide the true velocity at one point on the blade. The uncertainty in the LDV velocity measurement was 20 μm/s. A schematic of the experimental setup is shown in figure 20.

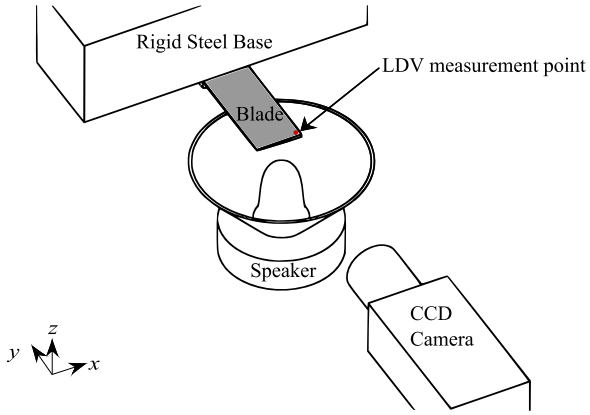

Figure 8: Schematic of the BIV calibration experiment.

Velocity measurements obtained from BIV were spatially averaged in the vicinity of the LDV measurement point. The LDV measurements were time averaged over the 200μs required to obtain two BIV images. The optical arrangement and vector processing were similar to that described in the previous section.

The velocity measured by the BIV system is shown as a function of the LDV measured velocity in Figure 9(a). The corresponding difference between the two measured velocities are shown in Figure 9(b) in "pixel equivalent" displacement. The LDV velocity was converted to "pixel equivalent" displacement by applying the PIV camera calibration to the LDV data. The peak locking effect (Westerweel (2000)), a common error in PIV measurements, is evident in the data. The standard deviation of the peak-locking effect is approximately 0.045 pixels. This corresponds to an accuracy of 1.2% of the full-scale measurement, or 9.1 mm/s over a range of 757 mm/s. These results will be used later in this paper for estimating the uncertainty of the blade modal amplitude.

[†]`http://www.archive.org/details/BIV_PIV_Phase_average_Mikrut_Morris_09`

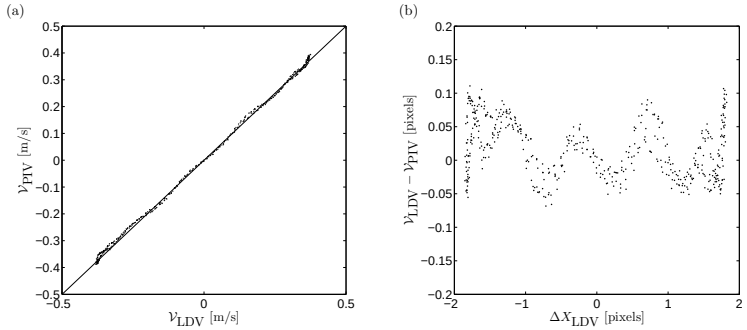

Figure 9: Accuracy of the correlation algorithms in measuring structural velocity: (a) BIV measured velocity as a function of LDV measured velocity. The solid line indicates a slope of 1 with zero offset; (b) Difference in measured velocity as a function of LDV measured velocity. Results are presented as "pixel equivalent" velocity.

2.3 Determination of Vibration Modal Amplitude

This section describes the mathematical operations necessary to obtain both instantaneous and mean-squared amplitudes of discrete vibration modes. Consider the cantilevered blade shown in figure 4. The velocity of the blade, $\mathbf{v}$ is assumed to be scalar valued representing the blade-normal component of the structural velocity at discrete spatial locations (x_i, y_j) and time (t_n), $[\mathbf{v}]_{i,j} = v(x_i, y_j)$. Here $i = 1$, $j = 1$ represents the leading edge of the blade tip. The trailing edge of the blade is represented by $i = M$, where M is determined by the number of velocity vectors along the chord that are provided by the PIV processing. The notation $[\ ]_{i,j}$ denotes the element of the argument corresponding to the i^{th} row and j^{th} column. The number of subscripts denotes the dimension of the argument; in this case a matrix with 2 dimensions. The velocities can be represented by a summation of eigenmodes as

$$[\mathbf{v}]_{i,j} = \sum_{p=1}^{P} [\mathbf{\Omega}]_{i,j,p} \, [\boldsymbol{\zeta}]_p. \tag{2}$$

where $\boldsymbol{\zeta}$ is a time-varying vector of modal amplitudes with dimensions $[P \times 1]$, where P is the number of modes used to represent the structural vibration. The eigenmode shapes of the structure are given by the three dimensional matrix $\mathbf{\Omega}$. Because the BIV technique provides velocity measurements at the tip of the structure, it will be useful to provide a more specific notation to represent these values. Specifically, the measurements along the chord of the blade tip are represented as

$$[\boldsymbol{\mathcal{V}}]_i \equiv v(x_i, y_{j=1}). \tag{3}$$

Similarly a matrix is defined to represent the mode shapes at the tip as

$$[\mathbf{\Phi}]_{i,p} \equiv [\mathbf{\Omega}]_{i,j=1,p} \, . \tag{4}$$

such that $\mathbf{\Phi}$ is a two dimensional $[M \times P]$ matrix with rows corresponding to the i^{th} measurement point along the chordwise direction and the columns corresponding to the p^{th} vibration mode evaluated at $y_{j=1}$. Unlike the full eigenmode shapes given by $\mathbf{\Omega}$, the columns of the matrix $\mathbf{\Phi}$ are not generally orthogonal.

The relationship between the observed velocities and the modal amplitudes is now given by

$$\boldsymbol{\mathcal{V}} = \boldsymbol{\Phi}\boldsymbol{\zeta}, \tag{5}$$

This relation can be inverted to obtain the modal amplitudes directly from the measured velocities:

$$\boldsymbol{\zeta} = \left[\boldsymbol{\Phi}^{\mathrm{T}}\,\boldsymbol{\Phi}\right]^{-1}\boldsymbol{\Phi}^{\mathrm{T}}\,\boldsymbol{\mathcal{V}} \tag{6}$$

where the superscript $_{\mathrm{T}}$ denotes the matrix transpose. The only constraint is that the columns $\boldsymbol{\Phi}$ must be linearly independent ($\boldsymbol{\Phi}$ must be full column rank). Equation 26 can be used with equation 21 to estimate the full blade velocity $\mathbf{v}$.

The mean squared amplitude of the various modes is most often of interest, and can be evaluated directly from an ensemble of velocity measurements ($\boldsymbol{\mathcal{V}}$) through equation 26. However, it will be useful to consider the mean squared amplitudes of the modes based on the statistics of the measured velocities in order to simplify the uncertainty analysis to follow. The ensemble of $\boldsymbol{\zeta}(t_n)$ can be represented as the matrix

$$\boldsymbol{\xi} \equiv \left[\begin{array}{cccccc} \boldsymbol{\zeta}(t_1) & \boldsymbol{\zeta}(t_2) & \boldsymbol{\zeta}(t_3) & \cdots & \boldsymbol{\zeta}(t_N) \end{array}\right]. \tag{7}$$

where the discrete time t_n is shown explicitly for clarity. Note that $\boldsymbol{\xi}$ is a $[P \times N]$ matrix, where N is the number of samples. The vector of mean-squared amplitudes of the P modes is estimated by

$$\boldsymbol{\sigma_\zeta}^2 \equiv \mathbb{D}\left(\frac{1}{N}\boldsymbol{\xi}\boldsymbol{\xi}^{\mathrm{T}}\right), \tag{8}$$

where the operator $\mathbb{D}\,()$ selects the diagonal elements of the argument. Note that $\boldsymbol{\sigma_\zeta}^2$ is a vector of length P.

The measured velocities can be used to define the ensemble of observations as

$$\boldsymbol{\Upsilon} = \left[\begin{array}{cccccc} \boldsymbol{\mathcal{V}}(t_1) & \boldsymbol{\mathcal{V}}(t_2) & \boldsymbol{\mathcal{V}}(t_3) & \cdots & \boldsymbol{\mathcal{V}}(t_N) \end{array}\right] = \boldsymbol{\Phi}\boldsymbol{\xi}, \tag{9}$$

The correlation matrix $\boldsymbol{C}$ is defined as

$$\boldsymbol{C} \equiv \frac{1}{N}\boldsymbol{\Upsilon}\boldsymbol{\Upsilon}^{\mathrm{T}} = \frac{1}{N}\boldsymbol{\Phi}\boldsymbol{\xi}\boldsymbol{\xi}^{\mathrm{T}}\,\boldsymbol{\Phi}^{\mathrm{T}}\,. \tag{10}$$

The vector of mean-squared amplitudes $\boldsymbol{\sigma_\zeta}^2$ can be found by taking the left pseudoinverse of $\boldsymbol{\Phi}$, $\mathbb{L} \equiv \left[\boldsymbol{\Phi}^{\mathrm{T}}\,\boldsymbol{\Phi}\right]^{-1}\boldsymbol{\Phi}^{\mathrm{T}}$ and the right pseudoinverse of $\boldsymbol{\Phi}^{\mathrm{T}}$, $\mathbb{R} \equiv \boldsymbol{\Phi}\left[\boldsymbol{\Phi}^{\mathrm{T}}\,\boldsymbol{\Phi}\right]^{-1}$:

$$\boldsymbol{\sigma_\zeta}^2 = \mathbb{D}\left(\mathbb{L}\boldsymbol{C}\mathbb{R}\right) \tag{11}$$

Equation 27 relates the mean-squared amplitudes of the structural modes given in $\boldsymbol{\sigma_\zeta}^2$ to the two-point correlation matrix of the observed velocities.

2.4 Uncertainty analysis

There are two types of errors which can arise in the estimation of $\boldsymbol{\sigma_\zeta}^2$. The first is noise corruption of $\boldsymbol{\mathcal{V}}$. The second type of error is associated with the discretization of the velocity by measuring displacement over a small time interval. This particular error is present because of the method by which PIV (and as a consequence, BIV) estimates velocity. These two errors will be discussed separately in the following subsections.

2.4.1 Noise corruption of the correlation matrix

Assume that $\boldsymbol{\mathcal{V}}$ is corrupted by additive noise. The observation matrix $\boldsymbol{\Upsilon}$ is modified as

$$\boldsymbol{\Upsilon} = \boldsymbol{\Phi\xi} + \boldsymbol{\eta}^{\mathrm{T}} ,$$

where $\boldsymbol{\eta}^{\mathrm{T}}$ is the ensemble of additive noise. The correlation matrix becomes

$$\boldsymbol{C} = \frac{1}{N} \left(\boldsymbol{\Phi\xi\xi}^{\mathrm{T}} \, \boldsymbol{\Phi}^{\mathrm{T}} \; + \boldsymbol{\eta}^{\mathrm{T}} \, \boldsymbol{\xi}^{\mathrm{T}} \, \boldsymbol{\Phi}^{\mathrm{T}} \; + \boldsymbol{\Phi\xi\eta} + \boldsymbol{\eta}^{\mathrm{T}} \, \boldsymbol{\eta} \right).$$

Applying the pseudoinverse operators $\mathbb{L}$ and $\mathbb{R}$ to the modified correlation matrix $\boldsymbol{C}$ yields

$$\mathbb{D}\left(\mathbb{L}\boldsymbol{C}\mathbb{R}\right) \quad = \quad \boldsymbol{\sigma_\zeta}^2 + \frac{1}{N}\mathbb{D}\left(\mathbb{L}\boldsymbol{\eta}^{\mathrm{T}} \, \boldsymbol{\xi}^{\mathrm{T}} \; + \boldsymbol{\xi\eta}\mathbb{R} + \mathbb{L}\boldsymbol{\eta}^{\mathrm{T}} \, \boldsymbol{\eta}\mathbb{R}\right). \tag{12}$$

The left hand side of equation 12 represents the measured quantity. The first term on the right hand side of equation 12 contains the true values of the modal amplitudes. The remainder of the terms are errors due to the additive noise. The second and third terms on the right hand side of equation 12 are noise-signal cross correlations, while the last is the autocorrelation of the noise. The signal-noise correlation terms can be finite in magnitude for a given experiment, but have an expected value of zero so long as the noise is not related to the mode shapes. However, the error due to noise autocorrelation is positive definite which leads to an expected bias. This error will be defined as

$$\left[\boldsymbol{\varepsilon}_{\mathrm{A}}\right]_p \equiv \frac{1}{N}\mathrm{E}\left[\left[\mathbb{D}\left(\mathbb{L}\boldsymbol{\eta}^{\mathrm{T}} \, \boldsymbol{\eta}\mathbb{R}\right)\right]_p\right] / \left[\boldsymbol{\sigma_\zeta}^2\right]_p , \tag{13}$$

where E[] is the expected value of the argument. The error is can be simplified to

$$\left[\boldsymbol{\varepsilon}_{\mathrm{A}}\right]_p = \left[\mathbb{D}\left(\left[\boldsymbol{\Phi}^{\mathrm{T}} \, \boldsymbol{\Phi}\right]^{-1}\right)\right]_p \left[\boldsymbol{\sigma_\eta}^2\right]_p / \left[\boldsymbol{\sigma_\zeta}^2\right]_p , \tag{14}$$

where the variance of the noise is given by

$$\left[\boldsymbol{\sigma_\eta}^2\right]_p \equiv \mathrm{E}\left[\left[\mathbb{D}\left(\frac{1}{N}\boldsymbol{\eta}^{\mathrm{T}} \, \boldsymbol{\eta}\right)\right]_p\right]. \tag{15}$$

2.4.2 Bias error due to velocity discretization

The bias error associated with the discretization of the velocity when using BIV will now be considered. The BIV measurement technique computes velocity based on displacement measurements with a specified time interval. This

can be considered as a discrete approximation to the velocity field using a central difference approach. Note that this discretization does not effect the mode shapes $\mathbf{\Phi}$. Therefore, according to equation 5, the bias error which manifests in the velocity estimation is proportional to $\boldsymbol{\zeta}$. Let the true value of $\boldsymbol{\zeta}$ at time t_n be of the form

$$[\boldsymbol{\zeta}]_p \equiv \left(\sqrt{2\,[\boldsymbol{\sigma}_{\boldsymbol{\zeta}}{}^2]_p}\right)\cos\left(2\pi\,[\boldsymbol{f}]_p\,t_n\right), \tag{16}$$

where $\boldsymbol{f}$ is a vector of frequencies associated with the mean-squared amplitudes $\boldsymbol{\sigma}_{\boldsymbol{\zeta}}{}^2$. Let the time between an image pair be Δt. The approximation of $\boldsymbol{\zeta}$ by BIV is

$$\left[\tilde{\boldsymbol{\zeta}}\right]_p \equiv \left(\frac{\sin\left(\pi\,[\boldsymbol{f}]_p\,\Delta t\right)}{\pi\,[\boldsymbol{f}]_p\,\Delta t}\right)\sqrt{2\,[\boldsymbol{\sigma}_{\boldsymbol{\zeta}}{}^2]_p}\cos\left(2\pi\,[\boldsymbol{f}]_p\,t_n\right). \tag{17}$$

The normalized error in the estimate of $\boldsymbol{\zeta}$ will be defined as

$$[\boldsymbol{\varepsilon}_{\mathrm{B}}]_p = \frac{[\boldsymbol{\zeta}]_p - \left[\tilde{\boldsymbol{\zeta}}\right]_p}{[\boldsymbol{\zeta}]_p}. \tag{18}$$

Using equations 16 and 17, this can be simplified as

$$[\boldsymbol{\varepsilon}_{\mathrm{B}}]_p = 1 - \frac{\sin(\pi\,[\boldsymbol{f}]_p\,\Delta t)}{\pi\,[\boldsymbol{f}]_p\,\Delta t}. \tag{19}$$

Thus, this error results in an underestimation of the amplitude of vibration. This error can be corrected for if the frequencies of oscillation $\boldsymbol{f}$ and the time between images Δt are known.

2.5 Experimental Validation of Uncertainty

The BIV measurement technique and the derived equations for the modal uncertainty were evaluated using a cantilevered beam with a cross section shown in figure 10. The cross section was constant over the 115.6 mm span. The beam was made from 6061−T6 aluminum bar stock. The second and third natural modes are shown in Figure 11. These were computed using FEA software (ProE Wildfire 2.0). The frequencies of the modes showin in figure 11 are 782.4 and 959.4 Hz respectively. The natural modes $\mathbf{\Omega}$ and frequencies of vibration $\boldsymbol{f}$ of the blade were experimentally verified using a scanning LDV in the setup described in figure 20.

Harmonic forcing in the form of acoustic pressure was applied to the blade using a 100W speaker. The separation between the cone of the speaker and the surface of the beam ($z-$direction) was 2.5 mm. The forcing was applied at the resonant frequencies.

The blade tip motion was recorded with one thousand image pairs ($N = 1000$). The mean squared amplitudes of vibration were computed using equation 27. The single point LDV was positioned near the blade tip and used as the reference transducer. Time series data were acquired for 60 seconds before and after BIV data acquisition. The autospectral density of the LDV data was computed and the mean-squared amplitude of the p^{th} mode, $\left[\overline{\zeta^2}\right]_p$, was determined by integrating around the frequency band of interest. The experimentally measured error in the estimation of modal amplitude is defined by

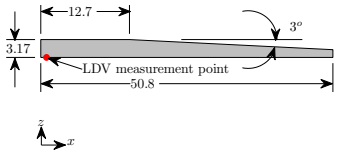

Figure 10: Sketch of blade cross section geometry (not to scale). All dimensions in mm. The cross section was constant across the 115.6 mm span.

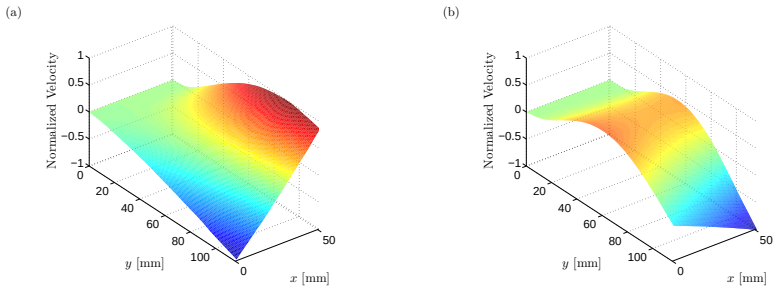

Figure 11: Shapes of the two structural modes of the test blade as computed by FEM. Shapes are exaggerated for clarity. (a) First torsion mode of the model, $[\boldsymbol{f}]_1 = 782.4$ Hz; (b) Second bending mode of the model, $[\boldsymbol{f}]_2 = 959.4$ Hz.

$$[\boldsymbol{\varepsilon}_{\mathrm{E}}]_p \equiv \frac{\sqrt{2\left[\overline{\zeta^2}\right]_p} - \sqrt{2\left[\boldsymbol{\sigma}_{\boldsymbol{\zeta}}{}^2\right]_p}}{\sqrt{2\left[\overline{\zeta^2}\right]_p}}, \tag{20}$$

where $\sqrt{2\left[\overline{\zeta^2}\right]_p}$ is the amplitude of the p^{th} mode as measured by the LDV and $\sqrt{2\left[\boldsymbol{\sigma}_{\boldsymbol{\zeta}}{}^2\right]_p}$ the amplitude of the p^{th} mode as measured by the BIV technique. The random error (equation 14) was approximated by assuming that the peak-locking error (cf. section 2.2.2) was the additive noise. The variance of the peak-locking error found in figure 9 (b) (corrected for the appropriate Δt) was substituted for $\left[\boldsymbol{\sigma}_{\boldsymbol{\eta}}{}^2\right]_p$.

The beam was harmonically forced only at first torsion at two different amplitudes to demonstrate the interaction of the two types of error. The Δt was varied among different tests to vary the influence of random and bias errors on the measured amplitude of vibration. Figure 12 presents both normalized errors as well as the experimentally measured error as a function of $(\Delta t)f$. The solid line in the figure represents the summation of the noise correlation error (ε_{A}) and the velocity discretization error (ε_{B}). The data show substantial agreement with the derived uncertainty values over the range of $(\Delta t)f$ tested. As expected, the lower values of $(\Delta t)f$ show a positive bias in the BIV measured modal amplitudes compared to the true value observed from the LDV. This is assumed to be a direct result of the noise correlation bias due to pixel locking in the digital image correlations. At higher $(\Delta t)f$, the BIV measured amplitudes were lower than the true values indicating that the velocity discretization error is dominant. For the specimen tested there was an optimal

range of $(\Delta t)f \approx 0.1$ where both types of error were found to be small.

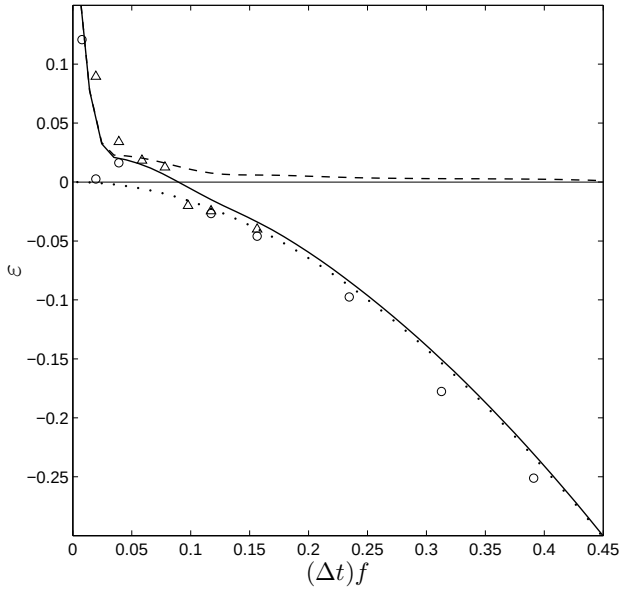

Figure 12: Error in amplitude estimate for a single mode as a function of $(\Delta t)f$. $\cdots$ ε_{B}; $--$ $\sqrt{2\varepsilon_{\mathrm{A}}}$; $-$ $\varepsilon_{\mathrm{B}} + \sqrt{2\varepsilon_{\mathrm{A}}}$; $\bigcirc$ ε_{E} from BIV with peak amplitude of ~ 2.3 m/s; $\triangle$ (ε_{E}) from BIV with peak amplitude of ~ 4.2 m/s.

The technique was also tested with two modes active. The Δt was 150 μs. The first torsion ($[\boldsymbol{f}]_1 \approx 782$ Hz) and second bending ($[\boldsymbol{f}]_2 \approx 959Hz$) were excited simultaneously with a corresponding $(\Delta t)f$ of 0.117 and 0.144, respectively. The amplitude estimates for first torsion and second bending are expected to be biased low by 2.25% and 3.37% low respectively. Table 1 shows the amplitudes of the modes obtained from the LDV measured autospectra compared to those obtained by BIV when one corrects for the velocity discretization error. The amplitude estimate obtained from the corrected BIV technique differ from those found by the LDV by 0.7% for first torsion and 1.75% for second bending. This agreement demonstrates the ability of the BIV measurements to obtain accurate estimates of the modal amplitudes when multiple modes are active.

	LDV [m/s]	BIV [m/s]
Mode 1	0.0015	N/A
Mode 2	1.4159	1.4097
Mode 3	0.7468	0.7338

Table 1: Comparison of modal amplitude estimates for a beam under two component harmonic forcing.

2.6 Conclusions

The BIV technique has been developed for acquiring simultaneous fluid and structure velocity measurements using a commerical PIV system. The method is non-intrusive and can measure structural velocity with accuracy similar to standard PIV.

There are a number of potential advantages compared to traditional structural measurements. First, the instantaneous amplitude of the blade mode shapes can be obtained because a spatial distribution of structural velocity is measured. When coupled with obtained PIV measurements of the fluid velocity, the causal relationships between the fluid and structural motion can be studied. An example was provided using a thin flat plat in a low-speed wind tunnel. A limit-cycle behavior was found in which the first torsional vibration mode was closely linked with a moving separation point. A second advantage of BIV is the ability to obtain aeroelastic measurements on rotating structures. This will allow measurements of both forced excitation and flutter in turbomachinery blades.

The theory relating the chordwise structural velocity profile at the free-end of a blade (the tip) to the modal amplitudes of the blade was presented. The measurements can provide independent realizations of the modal amplitude as long as the observable mode shapes are linearly independent. The equations were developed in order to describe the variance of the modal amplitudes in terms of the two-point correlation matrix of the measured velocity. This allowed for an analysis of the error due to noise corruption in the velocity measurements.

Two sources of error in the estimation of modal amplitudes were identified. The first is associated with the noise corruption of the velocity estimates and is due to the peak-locking effect, an error common to PIV. This results in an overestimation of the modal amplitudes. The second error is due to the central difference approximation of the velocity. Specifically, when the time between successive images is large the velocities are underestimated which leads to a systematic error in the modal amplitudes.

A specimen was created to represent a compressor blade geometry. The blade vibration modes were excited using harmonic acoustic forcing and compared with laser vibrometry measurements that were acquired simultaneously with the BIV. The results confirmed that the noise in the BIV measurements are dominated by peak-locking error. This led to an over estimation of the modal amplitudes when the displacement of the blade was small ($(\Delta t)f < 0.1$). The magnitude of the error agreed well with the predicted values based on the estimates of peak-locking noise. The error due to the central difference approximation of the velocity was found to dominate at large blade displacements ($(\Delta t)f > 0.1$). Good agreement was found between the experimentally measured magnitude and the theoretical prediction.

3 DEMONSTRATION OF BIV ON A HIGH-SPEED AXIAL COMPRESSOR

3.1 Introduction

This paper discusses the application of a novel blade vibration measurement technique to the rotor of a high speed axial compressor. The technique, termed Blade Image Velocimetry, estimates the blade vibration amplitude using standard PIV equipment. The development of this technique was motivated by the need for accurate, non-contact blade vibration amplitude estimates.

The complex aeromechanical environment which characterizes modern axial-flow turbomachinery provides unique challenges to blade vibration measurements. Specifically, measurements must characterize the dynamics of a system where the structure has both a low mass and low internal damping, rotating at high speed and is operating in a highly unsteady aerodynamic environment. Accurate knowledge of blade vibrations of the rotor of axial turbomachinery is both critical to aeromechanical design validation and difficult to obtain. The review article of Al-Bedoor (2002) provides a survey of the current technology applied to blade vibration measurement. There are two approaches which are commonly used. These are strain gages and Blade Tip Timing (BTT).

The use of strain gages to characterize the structural dynamics of turbomachinery blades dates back to the 1950s. Sensor size and accuracy have improved, but the fundamental operating principle has not changed. The sensors are typically recessed to preserve the aerodynamic shape of the blade (Kielb and Abhari (2003)). Few sensors are necessary to deduce the structural dynamics of the part. This technology remains attractive because it represents a well-established approach to obtaining accurate, time-resolved measurements of the blade motion. The application of strain-gages to rotating structures requires that both power and data be transmitted between a stationary data acquisition system and the rotating sensors. Traditionally, this is accomplished through slip-rings (Kielb et al. (2001)), which can introduce a significant amount of noise in the measurement system. In addition, the machining required to recess the sensor and wiring to be flush with the original aerodynamic surface of the blade may alter the structural dynamics. The successful implementation of this measurement technique requires substantial effort in the design of the measurement system and instrumentation of the rotor.

Blade Tip Timing (BTT) is a non-contact structural vibration measurement technology which has gained popularity over the last 40 years. Heath and Imregun (1998) and Lawson and Ivey (2005) provide a detailed description of this measurement technique. The concept will be summarized briefly. A set of proximity sensors are installed into the outer casing in a circumferential pattern. The proximity sensors can either be capacitive (Lawson and Ivey (2005)) or optical (Zellinski and Ziller (2000)). The sensors are installed such that they detect when a rotor blade tip passes by the sensor location. The average time required for a blade tip to move from one sensor location to another is known by the shaft speed of the rotor, the radius of the rotor at the tip and the circumferential distance between the two sensors. Any deviations from this average time indicates blade motion with respect to the hub. The advantage of this method over conventional strain gages is that the rotor does not need to be modified and installation only requires a few holes to be drilled in the outer casing. The output from this measurement system is a time-series of blade tip displacement. The sampling frequency of the method depends on the shaft speed of the compressor and the circumferential separation of the sensors, and is typically much lower than the frequency of blade vibration. Modes of vibration are distinguished by

observing their aliased frequencies (Zellinski and Ziller (2000)). One unique issue with this measurement system is the difficulty in obtaining amplitude and frequency estimates when the blade vibration frequency is an integer multiple of the shaft speed (a condition known as synchronous resonance). Data processing algorithms based on linear regression principles have been proposed to overcome this limitation (Heath (2000), Gallego-Garrido et al. (2007)). The accuracy of the vibration amplitude measurement can be comparable to strain-gage measurements under controlled circumstances (Lawson and Ivey (2005)). However, the presence of noise as well as the assumptions used in data processing can reduce the accuracy substantially (Carrington et al. (2001), Lawson and Ivey (2005)).

The BIV technique is a non-contact vibration measurement technology which can measure the fluid and structural velocity of a cantilevered beam simultaneously (Mikrut et al. (2010)). The concept of the measurement technique can be described as follows. A CCD camera is focused at the tip of a rotor blade through a window installed on the outer casing. Two pulses of light illuminate the blade tip as it passes through the camera's field of view. The displacement of the blade tip during the time between the two pulses of light yields information regarding the blade vibration. The frequency at which blade tip velocity data are acquired is typically much smaller than the frequency of blade vibration and so the data acquired by BIV are fundamentally different from time-resolved measurements (such as strain-gages).

The BIV technique was developed as an alternative to both BTT and strain gages. There are several important differences between BIV and Blade Tip Timing. First, estimates of the blade tip velocity are acquired with greater spatial resolution than currently offered by blade tip timing. The higher spatial resolution allows for the determination of modal amplitude based upon a set of known mode shapes. This avoids the need to rely upon the aliased frequencies to determine the mode of vibration. The high spatial resolution also provides more estimates of the blade tip velocity. These estimates are statistically independent from one another and can be used to minimize the influence of noise upon the velocity estimates.

Another important difference between the BIV technique and BTT is that adjustments to the measurement system can be made online with the BIV technique. Specifically, changes can be made to the time between light pulses, Δt. This flexibility allows the user to fine-tune the measurement system to optimize the measurement accuracy. Changes in Δt necessarily lead to changes in blade displacement between the two light pulses. However, the "noise" in the BIV measurement is, for large blade displacements, nearly constant with respect to displacement (Mikrut et al. (2010)). Therefore, changing Δt at a fixed speed (and fixed vibration amplitude) changes the signal to noise ratio. Alternatively, scaling Δt with shaft speed can yield a constant magnitude of additive noise over a wide range of turbomachine operating conditions. Furthermore, such a scaling simplifies data processing since the average blade displacement remains essentially constant.

Finally, the BIV technique allows for the simultaneous acquisition of the fluid velocity in the vicinity of the blade tip. The simultaneous acquisition of both fluid and structural velocity is important because the fluid and structural dynamics are coupled. This feature allows for the study of this coupling directly with a minimum number of instruments.

A brief review of the fundamentals of BIV will be presented. A method for the estimation of the measurement noise and the mean-squared modal amplitude using the statistics of the tip velocity will be presented. The demonstration of BIV on a high-speed axial compressor will then be presented.

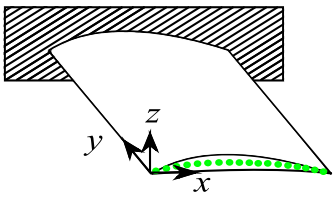

Figure 13: Sketch of a cantilevered rotor blade and measurement points.

3.2 Mathematical theory behind BIV

3.2.1 Review

A brief review of the BIV technique will be presented. A more detailed description of the technique can be found in Mikrut et al. (2010). A sketch of a generic rotor blade can be found in figure 13. The velocity of the blade, $\mathbf{v}$, is assumed to be the scalar valued z-component of the structural velocity at discrete spatial locations (x_i, y_j) and time (t_n): $[\mathbf{v}]_{i,j} = v(x_i, y_j)$. Here $i = 1$, $j = 1$ represents the leading edge of the blade tip. The trailing edge of the blade is represented by $i = M$, where M is determined by the number of velocity vectors along the chord that are provided by the processing algorithms. The notation $[\ ]_{i,j}$ denotes the element of the argument corresponding to the i^{th} row and j^{th} column. The number of subscripts denotes the dimension of the argument; in this case a matrix with 2 dimensions. The velocities can be represented by a summation of eigenmodes as

$$[\mathbf{v}]_{i,j} = \sum_{p=1}^{P} [\mathbf{\Omega}]_{i,j,p} \, [\boldsymbol{\zeta}]_p. \tag{21}$$

where $\boldsymbol{\zeta}$ is a time-varying vector of modal amplitudes with dimensions $[P \times 1]$, where P is the number of modes used to represent the structural vibration. The eigenmode shapes of the structure are given by the three dimensional matrix $\mathbf{\Omega}$. Note that the BIV technique provides blade velocity estimates at the tip. Mathematically, this can be expressed as

$$[\boldsymbol{\mathcal{V}}]_i \equiv v(x_i, y_{j=1}). \tag{22}$$

Similarly a matrix is defined to represent the mode shapes at the tip as

$$[\mathbf{\Phi}]_{i,p} \equiv [\mathbf{\Omega}]_{i,j=1,p} \, . \tag{23}$$

such that $\mathbf{\Phi}$ is a two dimensional $[M \times P]$ matrix with rows corresponding to the i^{th} measurement point along the chord-wise direction and the columns corresponding to the p^{th} vibration mode evaluated at $y_{j=1}$. Unlike the full eigenmode shapes given by $\mathbf{\Omega}$, the columns of the matrix $\mathbf{\Phi}$ are not generally orthogonal. The relationship between the tip velocity $\boldsymbol{\mathcal{V}}$ and the tip modes $\mathbf{\Phi}$ can be expressed as

$$[\boldsymbol{\mathcal{V}}]_{(i,1)} = \sum_{p=1}^{q} [\mathbf{\Phi}]_{(i,p)} \, [\boldsymbol{\zeta}]_{(p,1)} \, , \tag{24}$$

The relationship in equation 24 can also be expressed as

$$\boldsymbol{\mathcal{V}} = \mathbf{\Phi} \boldsymbol{\zeta}. \tag{25}$$

The modal amplitudes $\boldsymbol{\zeta}$ for a given velocity $\boldsymbol{\mathcal{V}}$ can be estimated by

$$\boldsymbol{\zeta} = \left[\boldsymbol{\Phi}^{\mathrm{T}}\,\boldsymbol{\Phi}\right]^{-1}\boldsymbol{\Phi}^{\mathrm{T}}\,\boldsymbol{\mathcal{V}}. \tag{26}$$

Alternatively, if an ensemble of observed blade tip velocities, Υ, are available, an estimate of the mean-squared modal amplitudes, can be obtained using the two point correlation matrix,

$$\boldsymbol{\sigma_{\zeta}}^2 = \mathbb{D}\left(\mathbb{L}\boldsymbol{C}\mathbb{R}\right), \tag{27}$$

where $\mathbb{D}$ selects the elements along the matrix diagonal, $\mathbb{L} \equiv \left[\boldsymbol{\Phi}^{\mathrm{T}}\,\boldsymbol{\Phi}\right]^{-1}\boldsymbol{\Phi}^{\mathrm{T}}$, $\mathbb{R} \equiv \boldsymbol{\Phi}\left[\boldsymbol{\Phi}^{\mathrm{T}}\,\boldsymbol{\Phi}\right]^{-1}$,

$$\boldsymbol{C} \equiv \boldsymbol{\Upsilon}\boldsymbol{\Upsilon}^{\mathrm{T}} = \frac{1}{N}\boldsymbol{\Phi}\boldsymbol{\xi}\boldsymbol{\xi}^{\mathrm{T}}\,\boldsymbol{\Phi}^{\mathrm{T}} \tag{28}$$

and

$$\boldsymbol{\Upsilon} = \left[\begin{array}{cccccc} \boldsymbol{\mathcal{V}}(t_1) & \boldsymbol{\mathcal{V}}(t_2) & \boldsymbol{\mathcal{V}}(t_3) & \cdots & \boldsymbol{\mathcal{V}}(t_N) \end{array}\right] = \boldsymbol{\Phi}\boldsymbol{\xi}, \tag{29}$$

$$\boldsymbol{\xi} \equiv \left[\begin{array}{cccccc} \boldsymbol{\zeta}(t_1) & \boldsymbol{\zeta}(t_2) & \boldsymbol{\zeta}(t_3) & \cdots & \boldsymbol{\zeta}(t_N) \end{array}\right]. \tag{30}$$

These relations yield exact estimates of the modal amplitudes in the absence of noise. Noise in the measurement system is assumed to be additive, uncorrelated with respect to the mode shapes $\boldsymbol{\Phi}$, zero-mean with a Gaussian probability density function with respect to time and independent and identically distributed (i.i.d.) over the blade chord. The ensemble of blade tip velocity are modified as

$$\boldsymbol{\Upsilon} = \boldsymbol{\Phi}\boldsymbol{\xi} + \boldsymbol{\eta}^{\mathrm{T}}, \tag{31}$$

where $\boldsymbol{\eta}$ the ensemble of additive noise. The mean-squared modal amplitude estimates (cf. equation 27) now yield

$$\left[\mathbb{D}\left(\mathbb{L}\boldsymbol{C}\mathbb{R}\right)\right]_p = \left[\boldsymbol{\sigma_{\zeta}^2}\right]_p\left(\left(1 + \left[\mathbb{D}\left(\left[\boldsymbol{\Phi}^{\mathrm{T}}\,\boldsymbol{\Phi}\right]^{-1}\right)\right]_p\left[\boldsymbol{\sigma_{\eta}^2}\right]_p / \left[\boldsymbol{\sigma_{\zeta}^2}\right]_p\right), \tag{32}$$

where

$$\left[\boldsymbol{\sigma_{\eta}^2}\right]_p \equiv \mathrm{E}\left[\left[\mathbb{D}\left(\frac{1}{N}\boldsymbol{\eta}^{\mathrm{T}}\,\boldsymbol{\eta}\right)\right]_p\right] \tag{33}$$

3.2.2 Determination of modal the amplitude(s) and additive noise

A non-trivial problem with the above relations occurs when the magnitude of additive noise is not known a priori. Equation 32 demonstrates that a non-zero bias error is introduced for finite noise. If not accounted for, this noise can bias the estimated modal amplitudes high. Consequently, it is desirable to be able to estimate the magnitude of noise corruption from the statistics of the blade tip velocity. Let the quantity $\left[\boldsymbol{f}\right]_p$ be defined as

$$\left[\boldsymbol{f}\right]_p \equiv \frac{1}{N}\left[\mathbb{D}\left(\mathbb{L}\tilde{\boldsymbol{\Upsilon}}\tilde{\boldsymbol{\Upsilon}}^{\mathrm{T}}\,\mathbb{R}\right)\right]_p \tag{34}$$

where $\tilde{\boldsymbol{\Upsilon}}$ is the experimentally measured ensemble of blade tip velocities using the BIV technique. Thus, $[\boldsymbol{f}]_p$ can calculated from the acquired data. Note that the elements of $[\boldsymbol{f}]_p$ contain the biased estimates of the mean-squared modal amplitudes (cf. equation 32). Consider the statistic

$$\tau \equiv \frac{1}{N}\sum_{n=1}^{s}\frac{1}{M-1}\sum_{i=1}^{M-1}\left(\tilde{\boldsymbol{\Upsilon}}-\frac{1}{M}\sum_{i=1}^{M}\tilde{\boldsymbol{\Upsilon}}\right)\left(\tilde{\boldsymbol{\Upsilon}}^{\mathrm{T}}-\frac{1}{M}\sum_{i=1}^{M}\tilde{\boldsymbol{\Upsilon}}^{\mathrm{T}}\right), \tag{35}$$

which is the ensemble-averaged chordwise variance of the measured tip velocity. Substituting equation 31 and performing the summations, this can be simplified as

$$\tau = \boldsymbol{\sigma}_{\boldsymbol{\Phi}}^{\mathbf{2}}\boldsymbol{\sigma}_{\boldsymbol{\zeta}}^{\mathbf{2}} + \sigma_\eta^2 \tag{36}$$

where

$$\boldsymbol{\sigma}_{\boldsymbol{\Phi}}^{\mathbf{2}} \equiv \frac{1}{M-1}\sum_{i=1}^{M-1}\left(\boldsymbol{\Phi}-\frac{1}{M}\sum_{i=1}^{M}\boldsymbol{\Phi}\right)\left(\boldsymbol{\Phi}^{\mathrm{T}}--\frac{1}{M}\sum_{i=1}^{M}\boldsymbol{\Phi}^{\mathrm{T}}\right) \tag{37}$$

is the variance of the p^{th} mode along the chord. Note that σ_η^2 is assumed constant for all modes (cf. equation 33) such that τ is a scalar quantity. This statistic has contributions from all modes and noise in the measurement system. Equations 38 and 52 represent a system of $Q+1$ equations with $Q+1$ unknowns which is easily solvable for the mean-squared modal amplitudes $\boldsymbol{\sigma}_{\boldsymbol{\zeta}}^{\mathbf{2}}$ and the noise σ_η^2.

3.2.3 Monte-carlo simulations of the algorithm performance

This section describes the effect of additive noise which has some chordwise distribution which has a non-zero correlation with any of modes $\boldsymbol{\Phi}$ on the estimation of the mean-squared modal amplitude $\boldsymbol{\sigma}_{\boldsymbol{\zeta}}^{\mathbf{2}}$ and the variance of the additive noise σ_η^2. Recall that these statistics can be estimated from the system of equations

$$\begin{aligned}
[\boldsymbol{f}]_p &\equiv \frac{1}{N}\left[\mathbb{D}\left(\mathbb{L}\tilde{\boldsymbol{\Upsilon}}\tilde{\boldsymbol{\Upsilon}}^{\mathrm{T}}\,\mathbb{R}\right)\right]_p \\
&= \left[\boldsymbol{\sigma}_{\boldsymbol{\zeta}}^{\mathbf{2}}\right]_p\left(\left(1+\left[\mathbb{D}\left(\left[\boldsymbol{\Phi}^{\mathrm{T}}\,\boldsymbol{\Phi}\right]^{-1}\right)\right]_p\left[\boldsymbol{\sigma}_{\boldsymbol{\eta}}^{\mathbf{2}}\right]_p/\left[\boldsymbol{\sigma}_{\boldsymbol{\zeta}}^{\mathbf{2}}\right]_p\right)\right. \qquad (38)\\
\tau &\equiv \frac{1}{N}\sum_{n=1}^{s}\frac{1}{M-1}\sum_{i=1}^{M-1}\left(\tilde{\boldsymbol{\Upsilon}}-\frac{1}{M}\sum_{i=1}^{M}\tilde{\boldsymbol{\Upsilon}}\right)\left(\tilde{\boldsymbol{\Upsilon}}^{\mathrm{T}}-\frac{1}{M}\sum_{i=1}^{M}\tilde{\boldsymbol{\Upsilon}}^{\mathrm{T}}\right) \\
&= \boldsymbol{\sigma}_{\boldsymbol{\Phi}}^{\mathbf{2}}\boldsymbol{\sigma}_{\boldsymbol{\zeta}}^{\mathbf{2}} + \sigma_\eta^2. \qquad (39)
\end{aligned}$$

Here, $\tilde{\boldsymbol{\Upsilon}}$ is the experimentally measured ensemble of blade tip velocities, $\mathbb{L}$ is the left pseudo-inverse of $\boldsymbol{\Phi}$, $\mathbb{R}$ is the right pseudo-inverse of $\boldsymbol{\Phi}$ and $\mathbb{D}$ is an operator which selects the diagonal elements of the argument. Equations 38 and 52 constitute a system of $Q+1$ equations in $Q+1$ unknowns and can be solved for $\boldsymbol{\sigma}_{\boldsymbol{\zeta}}^{\mathbf{2}}$ and σ_η^2. Note however that these relations were derived assuming that the noise η was statistically independent of both the mode shape $\boldsymbol{\Phi}$ and the time-varying modal amplitude $\boldsymbol{\zeta}$.

The effect of a correlated chordwise distribution of η was investigated using a Monte-Carlo approach. The mode shapes used in these simulations were identical to those used in the 98% speed investigation (cf. figure 26).

The additive noise was simulated in the following manner. The noise was split into two distinct components. These were a spatial contribution, η_s and a temporal contribution, η_t such that

$$[\boldsymbol{\eta}]_{(n,i)} \equiv [\eta_t]_{(n,1)} [\eta_s]_{(1,i)} . \tag{40}$$

The spatial contribution η_s was generated at each time n using the probability density function

$$\rho\left([\eta_s]_{(1,i)}\right) \equiv \frac{1}{\sqrt{Q'}} \sum_{p=p'}^{Q'} \frac{1}{\sqrt{2\pi\,[\tilde{\sigma}]^2_{(p,i)}}} \exp\left(-\frac{[\eta_s]_{(1,i)}}{2\,[\tilde{\sigma}]^2_{(p,i)}}\right), \tag{41}$$

where

$$[\tilde{\sigma}]_{(p,i)} = \frac{[\Phi^{\mathrm{T}}]_{(p,i)}}{\frac{1}{M}\sum_{i=1}^{M} [\Phi^{\mathrm{T}}]^2_{(p,i)}} \tag{42}$$

Here, p' represents the mode shapes for which the additive noise has some correlation and Q' is the total number of modes to which the noise is correlated. The factor $1/\sqrt{Q'}$ is included to ensure that the chord-wise variance for each realization is equal to 1. It is worth emphasizing that this probability density function has a standard deviation which varies along the chord. The variation is determined by the modes to which the noise is correlated. The temporal contribution of the noise has the probability density function

$$[\rho_{\eta_t}(\eta_t)]_{(n,1)} \equiv \frac{1}{\sqrt{2\pi\sigma_\eta^2}} \exp\left(-\frac{[\eta_t]_{(n,1)}}{2\sigma_\eta^2}\right), \tag{43}$$

where σ_η^2 is the specified variance of the additive noise.

Four-hundred realizations were acquired ($N = 400$) with 15 points along the chord ($M = 15$). The error in the mean-squared modal amplitude as a function of signal to noise ratio when a single mode is active can be seen in figure 14. It can be observed that, for the mode shapes used, the mean-squared modal amplitude estimates had a positive bias at low signal to noise ratios. This is a result of the shapes not being orthogonal. Specifically, the sixth and ninth modes are not orthogonal, but linearly independent. The correction proposed in section 3.2.2 helps to reduce the bias error, but cannot completely eliminate it. Note that the bias predicted in equation 33 provides an acceptable upper limit for the expected bias error. When the noise was correlated to all three modes, the bias error increased in both the un-corrected ($[\varepsilon_f]$) and corrected $[\varepsilon_\zeta]$ estimates. The bias error was significant for signal to noise ratios smaller than approximately 10.

Figure 15 shows the error in estimating the ensemble-variance of the additive noise (σ_η^2) when only one mode is active. Note that, due to the non-orthogonal mode shapes, the noise estimate is biased low. This bias error was constant with respect to signal to noise ratio and equal to approximately 5% when the noise was uncorrelated. The effect of correlated noise did not change the bias error, but rather increased magnitude of the random fluctuations about this bias.

Figure 16 shows the normalized error in the mean-squared modal amplitude estimate when all three modes are active. The amplitudes of each mode were equal. When the noise was uncorrelated, the bias error for each mode was similar to that observed when only one mode was active. However, when the noise was correlated to all three modes

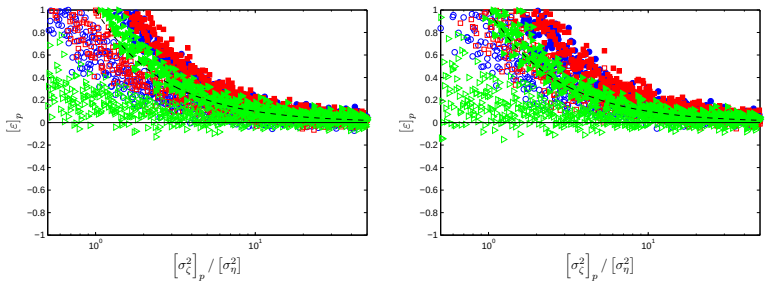

(a) Uncorrelated noise. (b) Noise correlated to all modes

Figure 14: Normalized error in the mean-squared modal amplitude estimate for a single mode. ○ $[\varepsilon_\zeta]_1$; ● $[\varepsilon_f]_1$; □ $[\varepsilon_\zeta]_2$; ■ $[\varepsilon_f]_2$; ▷ $[\varepsilon_\zeta]_3$; ▶ $[\varepsilon_f]_3$; − − Theoretical bias error due to additive noise (cf. equation 32).

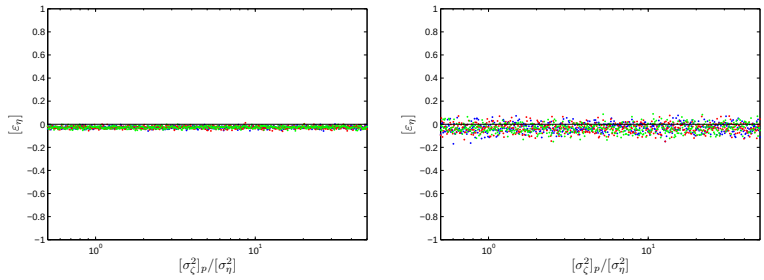

(a) Uncorrelated noise. (b) Noise correlated to all modes.

Figure 15: Normalized error in the noise estimate for a single mode. ● Mode 1, ● Mode 2, ● Mode 3

there was an increase in the bias error for the ninth mode. This suggests that the ninth mode is the most sensitive to noise, and will tend to yield modal amplitude estimates which bias high. Note that this bias error is significant when the signal to noise ratio is smaller than 10, which is similar to the trend observed when a single mode was active.

Figure 17 presents the normalized error in estimating σ_η^2 when all three modes are active. The trends observed are comparable to those observed when a single mode is active.

Figure 18 presents the estimated signal to noise ratio for a mode which was falsely identified as being active, as a function of the actual signal to noise ratio of the active mode. For example, included in this figure is the estimated signal to noise ratio of the sixth and ninth modes when only the twelfth mode was active. Note that for uncorrelated noise, the estimated signal to noise ratio for inactive modes does not exceed 1. In contrast, when the noise was correlated to all three modes, the maximum estimated signal to noise ratio did not exceed 2. It can therefore be concluded that the minimum estimated signal to noise ratio must exceed 2 for a mode to be correctly identified as active. Note that at this signal to noise ratio, the mean-squared modal amplitude estimates biased 50% high for uncorrelated noise and nearly 80% high for noise which was correlated to all three modes. Therefore, for the mode-shapes used in this study, an estimated signal to noise ratio greater than 2 is necessary to reliably detect an active mode. Note that the estimated modal amplitudes will have a significant positive bias. A signal to noise ratio greater than 10 is necessary to reliably predict the modal amplitudes with minimal bias error.

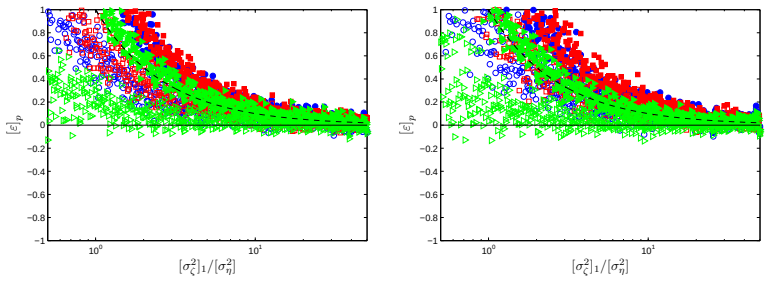

(a) Uncorrelated noise. (b) Noise correlated to all modes

Figure 16: Normalized error in the mean-squared modal amplitude estimate when all three modes are active. ∘ $[\varepsilon_\zeta]_1$; • $[\varepsilon_f]_1$; □ $[\varepsilon_\zeta]_2$; ■ $[\varepsilon_f]_2$; ▷ $[\varepsilon_\zeta]_3$; ▶ $[\varepsilon_f]_3$; − − Theoretical bias error due to additive noise (cf. equation 32).

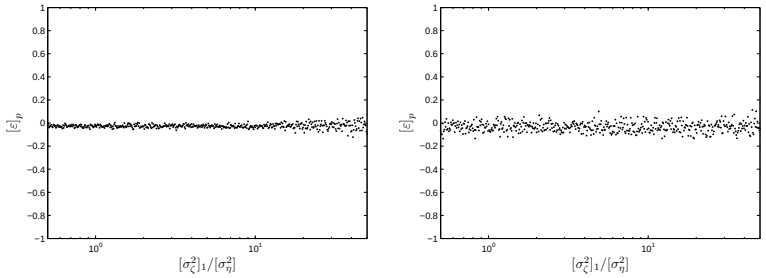

(a) Uncorrelated noise. (b) Noise correlated to all modes.

Figure 17: Normalized error in the noise estimate when all three modes are active.

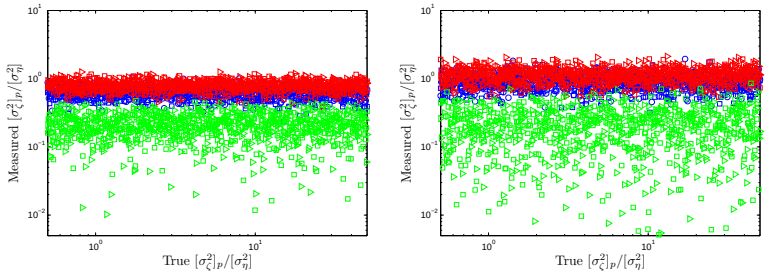

(a) Uncorrelated noise. (b) Noise correlated to all modes

Figure 18: Estimated signal to noise ratio of modes which are not active. ∘ $\left[\boldsymbol{\sigma}_{\boldsymbol{\zeta}}^{\mathbf{2}}\right]_1$; □ $\left[\boldsymbol{\sigma}_{\boldsymbol{\zeta}}^{\mathbf{2}}\right]_2$; ▷ $\left[\boldsymbol{\sigma}_{\boldsymbol{\zeta}}^{\mathbf{2}}\right]_3$.

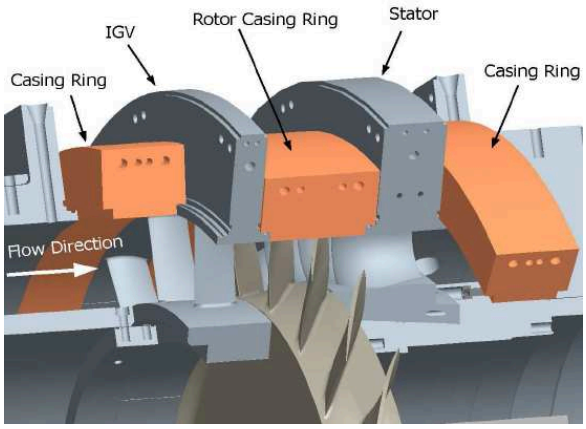

Figure 19: Schematic of the flow path of the compressor, from Cameron et al. (2006).

3.3 Demonstration of BIV on a high-speed compressor

3.3.1 Experimental Setup

The BIV technique was applied to the rotor of a high-speed, low pressure axial compressor. A description of the compressor can be found in Cameron *et al* Cameron et al. (2006). Figure 19 shows a schematic of the flow path through the compressor. A plexiglas casing window was installed on the rotor casing ring. Data were acquired at two shaft speeds. The first, 50% of design corresponded to a shaft speed of 7,345 RPM with an average blade tip speed of 175 m/s. The second was 98% of design and corresponded to a shaft speed of 14,690 RPM with an average blade tip speed of 350 m/s.

The BIV technique was implemented using equipment common to a conventional single-camera PIV system. A pattern of matte white dots whose diameter ranged from 60μm to 120μm were applied to the tip of one of the rotor blades. A 2048×2048 pixel Imager Pro X 4M CCD camera was focused at the rotor tip plane. The field of view was 128×128 mm resulting in a spatial resolution of 16 pixels/mm. The camera was calibrated using a curved calibration plate located on the inside of the casing window with marks placed uniformly in the axial and circumferential directions. A 3$^{\text{rd}}$ order polynomial fit was used to correct for image distortion due to both imperfections in the casing window and the mapping of the planar image onto a cylindrical surface. The polynomial fit had an rms of 1.5 pixels.

A double pulse Nd:YAG laser was used to illuminate the blade tip. Both beams were expanded using a spherical lens and an optical diffuser. The general orientation of the laser and camera relative to the casing is shown in figure 20. The optical axes of both the camera and laser were aligned axially with the rotor at the mid-chord of the blade tip. The laser was positioned approximately 3 feet from the rotor tip, which resulted in uniform illumination over the camera's field of view. The camera and laser were synchronized to an optical once-per-revolution sensor affixed to the rotor shaft. The synchronization, controlled by a programmable timing unit (PTU), was accurate to within $\pm 1.9^{\text{o}}$. The camera was operated in "double-frame, double exposure" mode, where two separate images (one for each laser pulse) were acquire. The time between pulses, Δt, was varied from 2μs to 100μs.

The following operations were used to enhance the features applied to the blade tip. These operations were performed prior to the estimation of blade tip velocity. First, a pair of complimentary sobel edge detection filters were applied to the image. These filters emphasized edges oriented at 45° and -45° relative to the $x-$axis of the CCD chip.

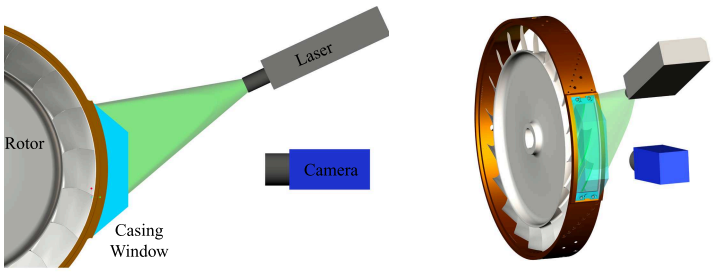

Figure 20: Schematic of the experimental setup.

A bias of -200 counts was then applied followed by a threshold which set to zero any pixels whose intensity was less than zero. These operations effectively increased the intensity of the features which were applied to the blade tip.

The algorithms used in the estimation of the blade tip velocity were similar to those found in conventional PIV. Specifically, the image pairs were segmented into interrogation windows over which the two-dimensional cross-correlation between the two frames was computed. The peak in the cross-correlation yielded an estimate of the blade tip displacement. The velocity was obtained by dividing this displacement by the appropriate Δt. Two approaches were used in estimating the blade tip velocity. The difference between each approach was the final window size. The initial window size was 128×128 pixels. The final window size ranged from 64×64 pixels to 32×32 pixels. In both cases, the window overlap was 50% of the window size and used an axisymmetric Gaussian weighting function. Finally, it should be noted that an initial estimate of the blade tip velocity was provided for the first pass. This was necessary for large Δt, where the blade tip displacement between the two successive images was greater than the interrogation window size. Acceptable velocity estimates were obtained using this approach for blade displacements which approached 300 pixels (18.75mm).

Vector validation was performed after each pass. This consisted of rejecting any velocity estimates where the peak in the correlation algorithm was less than 2.5 times larger than the next largest peak. Any vectors which deviated by more than 3 standard deviations relative to their neighbors were rejected. Finally, any vectors whose velocity deviated from the theoretical blade tip velocity (based upon the shaft speed and the tip radius) by more than 18% were rejected. This assumption implied that the fluctuating blade tip velocity (associated with blade vibration) was much smaller than the mean blade velocity (associated with the shaft speed of the compressor).

The velocity vectors, which were centered to a grid fixed to the CCD frame of reference, were mapped onto a coordinate system which was affixed to the blade tip. This required the estimation of the blade tip position. The following operations were used to estimate the blade tip position in the first image. The image enhancement techniques used for the velocity calculation (the complimentary sobel filters and thresholding operations) were also employed for the blade position estimate. After these processing algorithms were applied, a threshold which set to zero any pixels whose intensity was less than 400 counts was applied. A "mask" was created which was a binary image of the blade tip cross-section. The intensity of the pixels were non-zero only if the pixels lay inside the cross-section. The two-dimensional cross-correlation between this mask and the camera image was calculated. The approximate location of the peak in the cross-correlation was taken as an initial estimate of the location of the centroid of the blade tip. The blade tip camber-line was approximated using a 3rd order polynomial based upon the tip cross-section. Pixels which deviated by more than 6 mm from the camber line were set to zero. The two-dimensional cross-correlation between the resulting image and

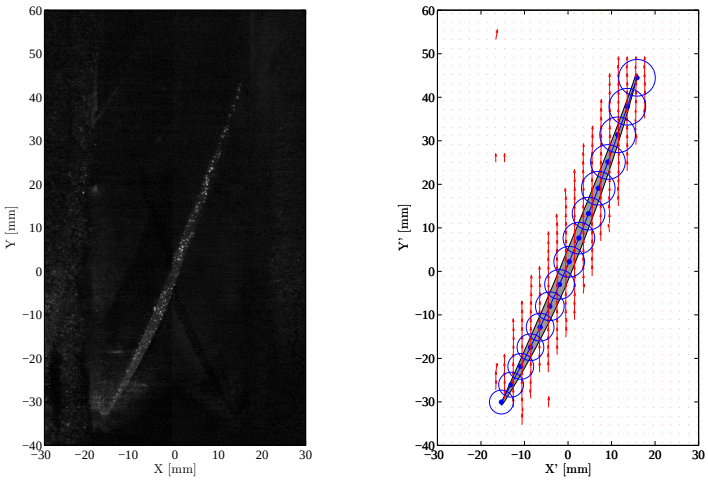

Figure 21: CCD image of the rotor blade tip and BIV estimate of blade tip velocity. → BIV estimated tip velocity, •– discrete locations along the camber-line used for averaging, ◯ Region W_i used for spatial averaging for a given camber-line location.

the original mask was then computed and the peak was taken as the blade tip centroid. These operations proved to be effective in determining the location of the blade tip to within 63μm (1 pixel).

The blade tip camber-line was discretized and the tip velocity was spatially averaged about these points. Vectors which were within a set radius (defined as 60% of the distance between two adjacent points along the camber line) were averaged to obtain an estimate of the blade tip velocity at that location. Figure 21 shows schematically the spatial averaging approach used. Mathematically, this operation can be described as

$$[\boldsymbol{\mathcal{V}}]_{(i,n)} \equiv \frac{1}{T} \sum_{(k,j)\in W_i}^{T} [\boldsymbol{V}]_{(k,j,n)} \,, \tag{44}$$

where W_i is the i^{th} region along the mean camber line about which to spatially average, T is the total number of vectors within region W_i and $\boldsymbol{V}$ are the velocity vectors obtained by BIV centered to the camera's coordinate system. Note that k and j are indicies corresponding to the $x'-$ and $y'-$axes of the CCD chip respectively. The number of points along the chord, M, varied for each processing approach. The variation was done such that the number of vectors used in the spatial averaging, T was consistent between the two approaches. The spatial discretization used for the 32×32 pixel interrogation windows was $M = 30$, which resulted in 8 vectors per chord-wise location. The discretization used for the 64×64 pixel window study was $M = 15$, which resulted in 10 vectors per chord-wise location.

3.3.2 Results

The ensemble and chordwise-averaged velocity yields an estimate of the steady blade tip velocity. A comparison between the steady tip velocity obtained by the BIV technique and the theoretical tip velocity (as determined using the blade tip radius and the shaft speed) provides a general indication of the accuracy of the technique. Figure 22 shows the normalized ensemble and chord-averaged blade tip velocity, defined as

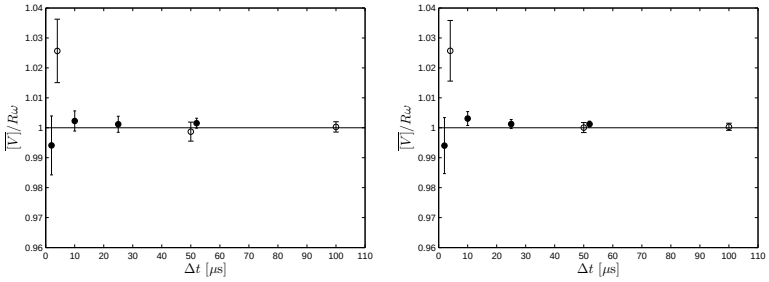

(a) 32×32 pixel windows, $T = 30$. (b) 64×64 pixel windows, $T = 15$.

Figure 22: Normalized steady blade tip velocity as a function of Δt and BIV interrogation window size for two shaft speeds. ○ 7,345 RPM; • 14,690 RPM.

$$\overline{[V]} \equiv \frac{1}{N}\sum_{n=1}^{N}\frac{1}{M}\sum_{i=1}^{M}[\boldsymbol{V}]_{(i,n)}/\mathcal{R}\omega \tag{45}$$

where $\mathcal{R}$ is the tip radius, ω is the shaft speed in radians per second. The error bars represent the 99% confidence interval normalized by $\mathcal{R}\omega$. There are several features which should be noted. First, the accuracy of the technique increases with increasing Δt (and consequently blade tip displacement) regardless of the size of the interrogation windows. This manifests as reductions in both the bias of the normalized velocity and in the confidence interval. When the Δt was greater than 10μs, the error in the average blade velocity was less than 1%. Second, note that the trends in normalized velocity are nearly identical between the two approaches using different interrogation windows. This suggests that interrogation window size has a relatively small effect on the accuracy of the steady velocity estimate. In general, it can be concluded that the method accurately captures the steady tip velocity due to shaft rotation.

An analysis of the fluctuating velocity was performed. The rotor used in these experiments had a conservative structural design and as such had been assumed to be rigid over the operating range of the compressor. A way to evaluate this assumption is to observe the probability distribution function (pdf) of the fluctuating velocity. Figure 23 shows the pdf of the fluctuating chord-normal velocity as a function of Δt at 50% design speed. Note that the pdf was normalized to have a maximum of 1 at each chord-wise location to better elucidate the spatial variation of the pdf. The chord-normal velocity was defined as

$$[\boldsymbol{V_N}]_{(i,j,n)} \equiv \left([\mathcal{V}_x]_{(i,j,n)} - \overline{\mathcal{V}_x}\right)\sin(\gamma) + \left([\mathcal{V}_y]_{(i,j,n)} - \overline{\mathcal{V}_y}\right)\cos(\gamma), \tag{46}$$

where γ is the stagger angle of the rotor at the tip and $\overline{\mathcal{V}_x}$ and $\overline{\mathcal{V}_y}$ are the ensemble-averaged velocity in the $x-$ and $y-$ directions in the camera's reference frame. Also shown in figure 23 is the fluctuating velocity expressed as "pixel-equivalent" displacement. It can be observed that the fluctuating tip velocity decreased when the Δt increased. It can also be observed that for $\Delta t < 50\mu$s, the blade fluctuating displacement remained nearly constant with a standard deviation of nearly 0.15 pixels. This suggests that a significant component of the fluctuating velocity was due to uncertainty in estimating the sub-pixel displacement of the blade tip. This uncertainty is a well-established source of error in BIV Mikrut et al. (2010). Note that there is a noticeable increase in the fluctuating displacement when the Δt was increased from 50μs to 100μs. This change, which increased the standard deviation by approximately 0.1 pixel, may indicate the presence of tip motion which was previously un-detectable due to the high level of noise.

Another feature to note is the spatial distribution of the pdf with respect to the chord. It can be observed that the fluctuations were large at the leading and trailing edges and relatively small at mid-chord. This behavior can be explained as follows. Referring back to figure 21, it can be observed that there were fewer features at the leading and trailing edges when compared with the mid-chord of the blade tip. Few particles can reduce the correlation peak intensity (see chapter 3 of Raffel et al. (2007)), which can result in increased uncertainty in the velocity estimate, especially at the sub-pixel level. This uncertainty is expected to be independent of Δt for particle displacements greater than 10 pixels when cast in pixel-equivalent displacement. Note that for the data presented in figure 23 there was only a slight increase in the magnitude of the pixel-equivalent fluctuations. This suggests that the a significant portion of the observed fluctuations at 50% of design speed are due to uncertainty in the estimate of the true blade displacement.

The chord-normal fluctuating velocity pdf as a function of Δt for the 98% speed investigation are shown in figure 24. It can be observed that the magnitude of the velocity fluctuations decreased with a corresponding increase in Δt. This suggests that a significant portion of the observed velocity fluctuations were due to inaccuracies in the estimate of the true blade displacement. The fluctuating tip displacement also supports this conclusion. However, it should be noted that at a $\Delta t > 10\mu$s, there was a noticeable increase in the magnitude of the fluctuations at the leading edge of the blade tip. These fluctuations increased when the Δt was increased. This may indicate the presence of a vibratory mode which had a large response at the leading edge.

The analysis presented in section 3.2.2 was applied to the fluctuating velocity. A small subset of the rotor's eigenmodes were used in the analysis. These modes were selected based upon the rotor's Campbell diagram as the most likely to be excited at the shaft speeds investigated. This resulted in different modes being used for each speed. Each mode-shape was normalized such that the L_2 norm was equal to one. Figure 25 and 26 show the mode shapes used for the 50% and 98% speed investigations respectively. Note that these shapes are two-dimensional. The analysis outlined in sections 3.2.1 and 3.2.2 were applied to each component of velocity and the results were combined using vector algebra to yield estimates of the modal amplitudes.

The mean-squared modal amplitudes for the 50% speed investigation can be seen in figure 27. Here, the estimates are presented as functions of Δt for the two interrogation window sizes used. Note that the estimates were corrected for the velocity discretization bias (cf. Mikrut et al. (2010)). The following features should be noted. First, an increase in Δt resulted in a decrease in the estimates for both mean-squared modal amplitudes and noise. This was consistent with the pdfs of the chord-normal velocity. The decrease was greater than 2 orders of magnitude over a similar increase in Δt and effected all modes. An explanation is that the chord-wise distribution of additive noise was correlated with one or multiple mode shapes. Monte-Carlo simulations demonstrated that a significant bias error can be introduced when the noise is correlated with a mode shape, even when the approach outlined in section 3.2.2 was used. The magnitude of this bias error depended upon the degree of correlation between the noise and the mode shape(s), with an upper limit similar to the expected bias in equation 33. A description of these simulations can be found in appendix 3.2.3. Observing the pdf for $\Delta t = 4\mu$s presented in figure 23, it is clear that the noise varied over the chord. It can therefore be concluded that the overall trend with respect to Δt was due to correlated noise, which resulted in biased estimates of the modal amplitudes. An increase in Δt decreased the magnitude of the noise and consequently the bias error.

Another observation is that an increase in window size (and corresponding decrease in spatial resolution) resulted in a decrease in the noise as well. This reduction varied with Δt and ranged from a factor of 2 to 5. Note that the

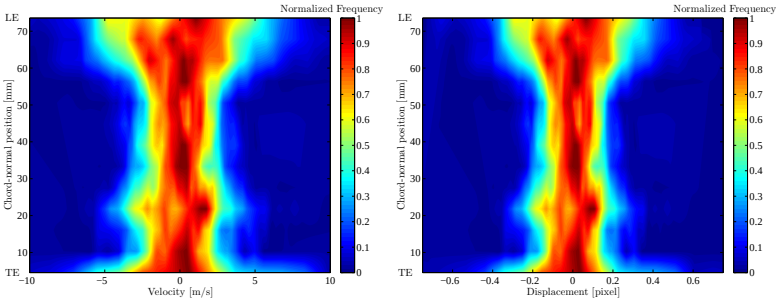

(a) Velocity, $\Delta t = 4\mu$s (b) Displacement, $\Delta t = 4\mu$s

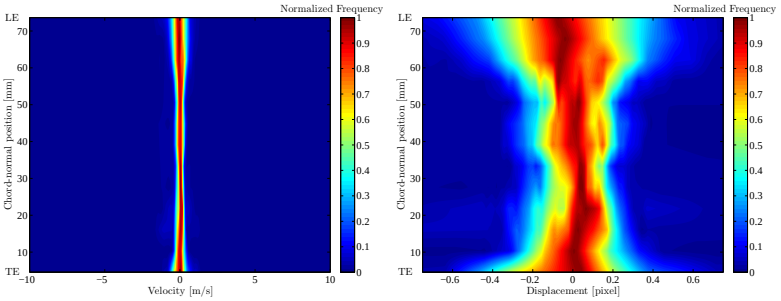

(c) Velocity, $\Delta t = 50\mu$s (d) Displacement, $\Delta t = 50\mu$s

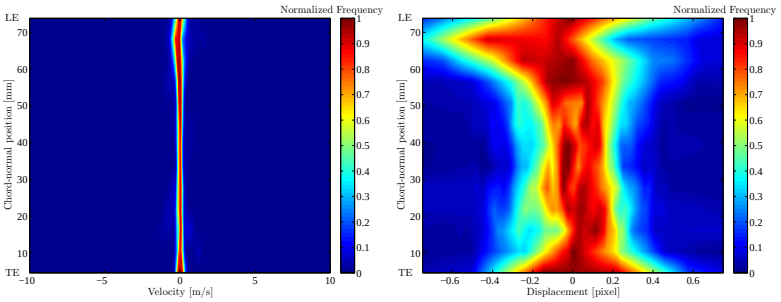

(e) Velocity, $\Delta t = 100\mu$s (f) Displacement, $\Delta t = 100\mu$s

Figure 23: Normalized probability density functions of the fluctuating chord-normal velocity and pixel-equivalent displacement as a function of chord-wise position at 50% design speed (7,345 RPM). Interrogation window size was 64×64 pixels.

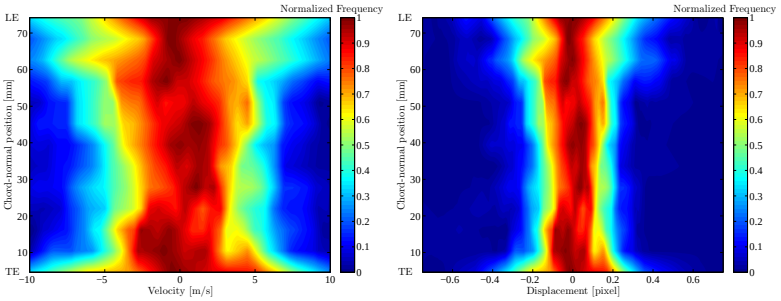

(a) Velocity, $\Delta t = 2\mu$s (b) Displacement, $\Delta t = 2\mu$s

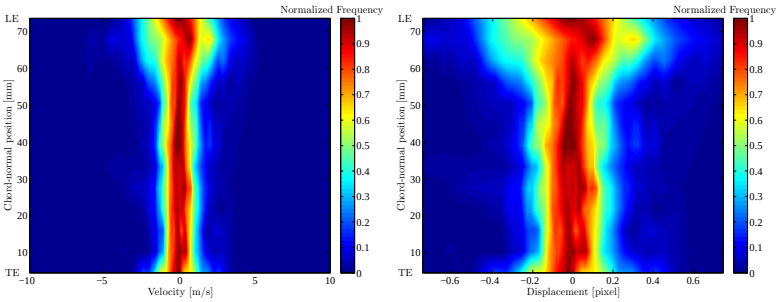

(c) Velocity, $\Delta t = 10\mu$s (d) Displacement, $\Delta t = 10\mu$s

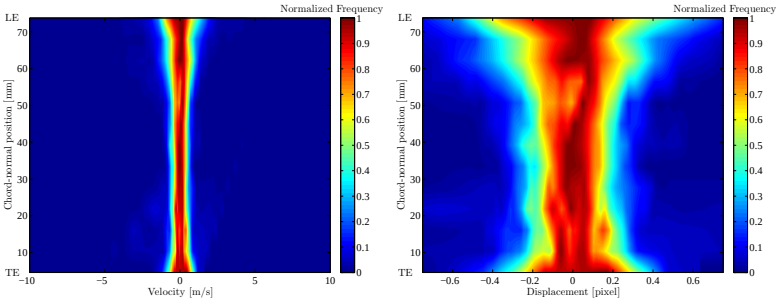

(e) Velocity, $\Delta t = 25\mu$s (f) Displacement, $\Delta t = 25\mu$s

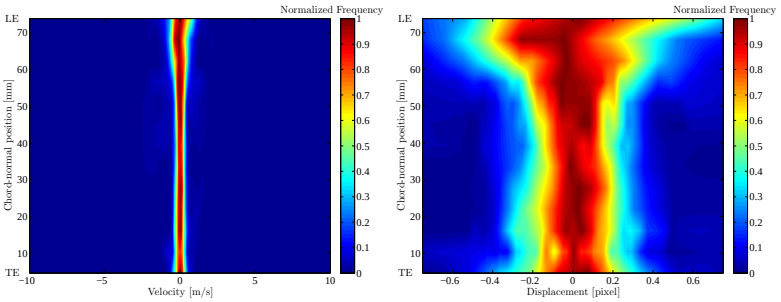

(g) Velocity, $\Delta t = 50\mu$s (h) Displacement, $\Delta t = 50\mu$s

Figure 24: Normalized probability density functions of the fluctuating chord-normal velocity and pixel-equivalent displacement as a function of chord-wise position at 98% design speed (14,690 RPM). Interrogation window size was 64×64 pixels.

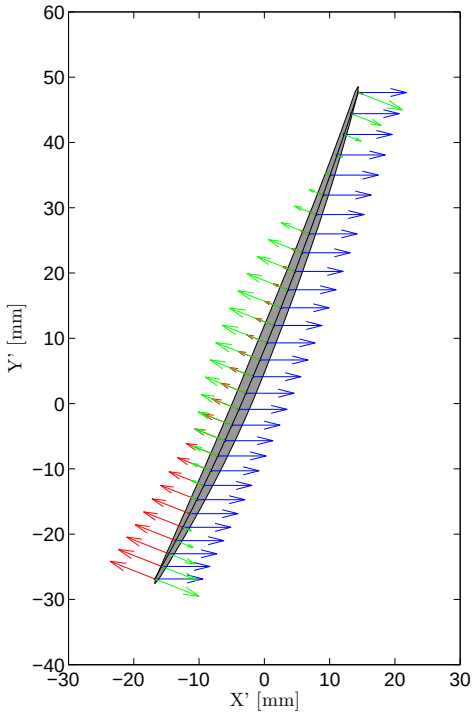

Figure 25: Mode shapes which may be excited at 50% speed. → Mode 1, $F \approx 435$ Hz; → Mode 3, $F \approx 2,736$ Hz; → Mode 7, $F = 5,750$ Hz.

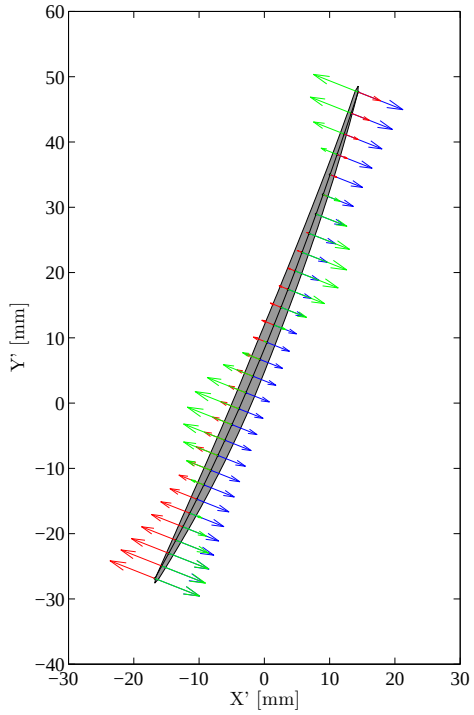

Figure 26: Mode shapes which may be excited at 100% speed. → Mode 6, $F \approx 4,640$ Hz; → Mode 9, $F \approx 7,799$ Hz; → Mode 12, $F = 10,768$ Hz.

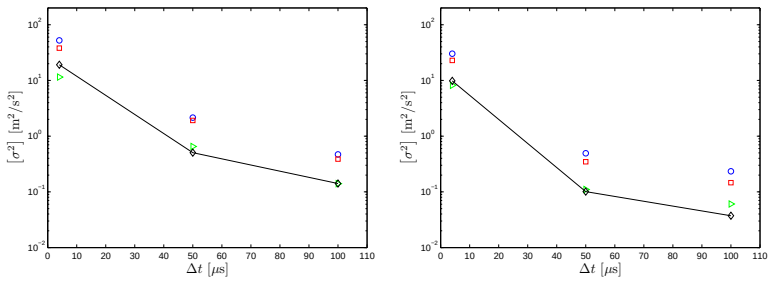

(a) 32×32 pixel windows. (b) 64×64 pixel windows.

Figure 27: Mean-squared modal amplitude at 50% design speed as a function of Δt for two interrogation window sizes. $\circ$ $[\boldsymbol{\sigma}^2_{\boldsymbol{\zeta}}]_1$; $\square$ $[\boldsymbol{\sigma}^2_{\boldsymbol{\zeta}}]_3$; $\triangleright$ $[\boldsymbol{\sigma}^2_{\boldsymbol{\zeta}}]_7$; $\diamondsuit$ σ^2_η.

number of vectors used in the spatial averaging (cf. equation 45) was consistent between the two approaches. Therefore, the decrease in noise was due to an increase in the accuracy of the correlation algorithms in estimating the true blade displacement.

A final observation must be made regarding the magnitudes of the mean-squared amplitudes relative to the noise (the signal to noise ratio). Modes 1 and 3 show a signal to noise ratio (SNR) greater than 1 for both windows and all Δt investigated, whereas mode 7 has a signal to noise ratio of nearly 1. Increasing the window size and the Δt increased this ratio for modes 1 and 3, but had little effect on mode 7. The largest recorded SNR for the first mode was about 6.3, which occurred at a $\Delta t = 100\mu$s and a window size of 64×64 pixels. The third mode had a maximum of approximately 4, which occurred at the same Δt and window size. Monte-carlo simulations using correlated noise show that when the fluctuating velocity is due only to noise, the estimated SNR is does not exceed 2 when the analysis presented in section 3.2.2 is used (cf. appendix 3.2.3). Thus, it can be concluded that the observed fluctuations in blade tip velocity are due in part to blade vibration in the first mode. The true amplitude is probably lower than the estimated amplitude, owing to the positive bias induced by the correlated noise. In addition, it can also be concluded that vibration in the seventh mode cannot be resolved by the BIV technique for this investigation, due to the large amount of measurement noise. It is possible that some portion of the fluctuating velocity is due to vibration in the third mode. However, because the SNR is not much larger than 2, the results for this investigation were not conclusive.

The mean-squared modal amplitude for the 98% speed investigation as a function of Δt and final interrogation window size is shown in figure 28. Note that, similar to the results presented for the 50% speed investigation, the mean-squared modal amplitudes and the noise estimates decreased when the Δt was increased, regardless of the interrogation window size. In addition, the estimated noise was similar in magnitude between the two speeds for a given Δt. This observation reinforces the conclusion that the estimated noise was due to inaccuracies in the estimation of the true blade tip displacement. An increase in the final interrogation window size also reduced the magnitude of the noise. The similarities observed in the noise estimates between both speeds investigated suggest that the additive noise is dependent upon the Δt and window size used, and not necessarily on the actual blade tip velocity. The implication is that, so long as the Δt is sufficiently small such that the blade tip remains in the camera's field of view, the accuracy of the technique can be independent of shaft speed. Based upon the observed maximum SNR, it can be concluded that the sixth mode (with a SNR of nearly 10) and the ninth mode (with a SNR of about 7) had significant contributions to the observed

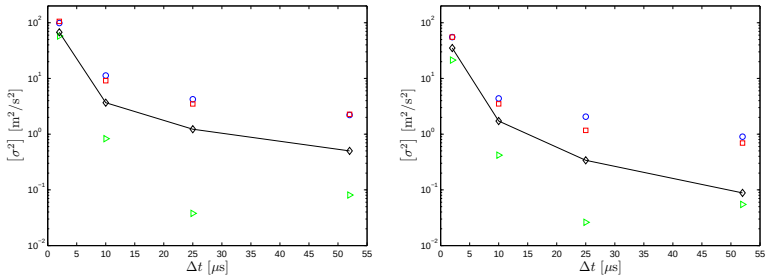

(a) 32×32 pixel windows. (b) 64×64 pixel windows.

Figure 28: Mean-squared modal amplitude at 98% design speed as a function of Δt for two interrogation window sizes. ○ $[\boldsymbol{\sigma}_{\boldsymbol{\zeta}}^{\mathbf{2}}]_6$; □ $[\boldsymbol{\sigma}_{\boldsymbol{\zeta}}^{\mathbf{2}}]_9$; ▷ $[\boldsymbol{\sigma}_{\boldsymbol{\zeta}}^{\mathbf{2}}]_{12}$; ♢ σ_η^2.

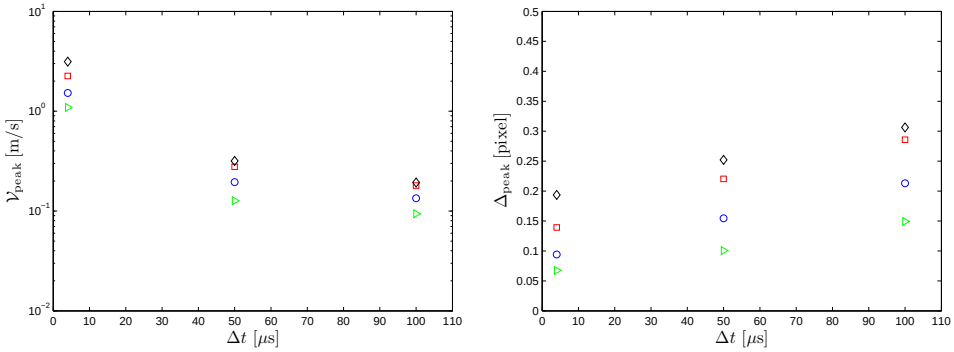

(a) Velocity. (b) Pixel-equivalent displacement.

Figure 29: Peak response of the blade at 50% design speed as a function of Δt using 64×64 pixel interrogation windows. ○ mode 1; □ mode 3; ▷ mode 7; ♢ 1 standard deviation of estimated noise.

fluctuating velocity, whereas the contributions from mode 12 cannot be distinguished from the noise.

Although the modal amplitudes of vibration are of interest, it is also useful to consider the maximum response of the blade at the tip. This quantity will be referred to as the peak response of the blade. This is considered to be the highest velocity over the chord at a given modal amplitude and can be expressed mathematically as

$$[\boldsymbol{\mathcal{V}}_{\text{peak}}]_p = \text{MAX}\left(\left|[\boldsymbol{\Phi}]_{(i,p)}\sqrt{\left[\boldsymbol{\sigma}_{\boldsymbol{\zeta}}^{\mathbf{2}}\right]_{(p,1)}}\right|\right) \tag{47}$$

where MAX() selects the maximum value of the argument. Figure 29 shows the peak response of the blade at 50% design speed in both velocity and pixel-equivalent displacement. Note that regardless of the Δt, the peak response for each mode is always smaller than the standard deviation of the estimated noise. This is a consequence of the normalization applied to the mode-shapes. The requirement that the L_2 norm be equal to one implies that $[\boldsymbol{\Phi}]_{(i,p)} \leq 1$ for all i and p. Thus, the peak response will have an upper limit equal to the modal amplitude. It can be observed that neither the noise nor the peak response exceeds 0.5 pixels for this speed. This is consistent with the ensemble-pdfs of the fluctuating chord-normal velocity, presented in figure 23.

Figure 30 presents the estimated peak response for the blade at 98% of design speed. In contrast to the 50% speed results, the peak response for sixth and ninth modes exceeds the noise at long Δt. The peak pixel-equivalent displacement

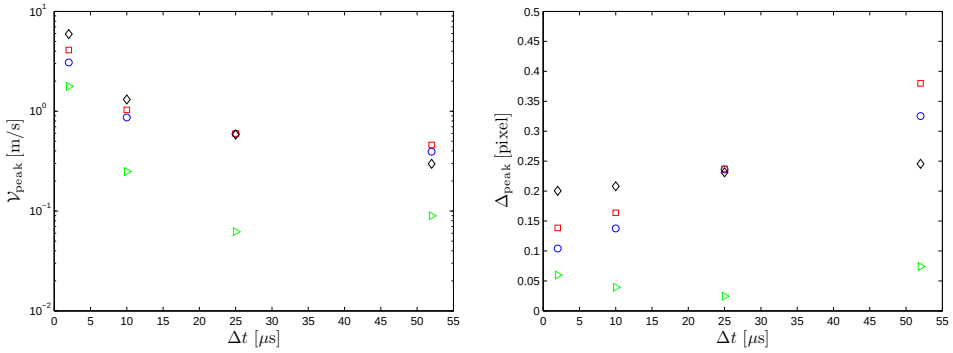

(a) Velocity.

(b) Pixel-equivalent displacement.

Figure 30: Peak response of the blade at 98% design speed as a function of Δt using 64×64 pixel interrogation windows. ○ mode 6; □ mode 9; ▷ mode 12; ♢ 1 standard deviation of estimated noise.

	7,345 RPM		14,690 RPM	
Mode	$[\boldsymbol{\sigma_\zeta}]_p$ [m/s]	$[\boldsymbol{\Delta_\zeta}]_p$ [pixel]	$[\boldsymbol{\sigma_\zeta}]_p$ [m/s]	$[\boldsymbol{\Delta_\zeta}]_p$ [pixel]
1	0.48	0.77	N/A	N/A
3	0.38	0.61	N/A	N/A
7	< 0.25	< 0.39	N/A	N/A
6	N/A	N/A	0.95	0.78
9	N/A	N/A	0.83	0.69
12	N/A	N/A	< 0.23	< 0.19
Noise	0.19	0.31	0.30	0.25

Table 2: Estimated maximum vibratory tip displacement and noise level for 50% and 98% of design speed using a final interrogation window size of 64×64 pixels.

increased linearly with increasing Δt, which would be expected if the blade were vibrating. The peak displacement for the twelfth mode, however, remained essentially constant at less than 0.1 pixels. This suggests that any vibrations due to the twelfth mode were un-detectable.

The findings of these two speed studies when using the 64×64 pixel interrogation windows are summarized in table 2. Presented in this table is the root-mean-squared (RMS) modal amplitude $[\boldsymbol{\sigma_\zeta}]_p$ and the equivalent RMS displacement in pixels, $[\boldsymbol{\Delta_\zeta}]_p$. The following conclusions can be made. First, the RMS of the modal amplitudes are less than 0.3% of the theoretical tip speed, which verifies the assumption that the blade vibration amplitudes are much smaller than the average tip speed. In addition, it can be observed that the RMS modal amplitudes and noise are all less than 1 pixel. Thus, a significant portion of the measured fluctuations are due to noise. The noise has a similar magnitude for both speeds when expressed in terms of pixel-equivalent displacement. This suggests that the source of the noise is uncertainty in estimating the true blade displacement. Finally, it may be concluded that at 50% speed, the first and third modes are excited whereas at 98% speed the sixth and ninth modes are active. The trends shown in figures 27 and 28 suggest that these amplitude estimates may be biased high, and as such represent the upper-bounds of the modal amplitudes.

3.4 Conclusions

The BIV technique has been demonstrated on a high speed compressor. The theory behind the technique has been expanded to allow for the estimation of the noise and the un-biased modal amplitudes when the noise is not know a-priori. This approach requires that a simple statistic of the ensemble of blade tip velocity be estimated and as such can be applied quite easily. This approach can significantly reduce the bias error due to additive noise.

The BIV technique has been applied to a high-speed axial compressor at realistic tip velocities. Data were acquired at 50% of design speed (with a tip velocity of 175 m/s) and 98% of design speed (with a tip velocity of 350 m/s). The technique accurately estimated the average tip velocity to within 0.5% of the theoretical tip speed.

An analysis of the fluctuating tip velocity revealed the following. First, a significant portion of the velocity fluctuations were due to noise in the measurement system. The origin of the noise was the uncertainty in the estimation of the true blade tip displacement. This displacement uncertainty had a similar magnitude for both speeds investigated and as such did not depend on shaft speed. Increasing the time between images (Δt) and increasing the final interrogation window size both reduced the magnitude of the noise.

It was determined that at 50% of design speed, the first and third natural modes of the rotor were excited, whereas at 98% of design speed the sixth and ninth modes were excited. The amplitude of these vibrations was determined to be much smaller than the average tip speed.

4 INVESTIGATION OF THE AEROELASTIC RESPONSE OF AN ISOLATED COMPRESSOR BLADE

4.1 Introduction

The aeroelastic behavior of a single cantilevered blade in a uniform subsonic and transonic flow was investigated. Note that there exist significant differences between the aeroelastic system in this configuration and those found in an axial compressor. However, there may exist similarities in the fundamental mechanisms for which energy is exchanged between the fluid and the structure. In addition, the methods used in identifying the non-linear aeroelastic mechanisms of this "simple" system will be directly applicable to more complex turbomachinery environments. A brief review of the current state of knowledge regarding subsonic-compressible and transonic aeroelasticity will be presented. A description of the experimental setup will be presented followed by the results of four investigations. The first characterized the instantaneous flow field to which the blade was subjected. The second investigation described the structural response of the blade to a steady, uniform flow as a function of Mach number, angle of attack, blade stiffness and the presence of an end-wall. The third investigation characterized the aerodynamic damping which was associated with the steady flow. The final investigation described the response of the blade to a mechanical impulse.

4.2 Review of limit cycle oscillations of wings in compressible flow

There are many phenomena which lead to limit-cycle oscillations of wings in compressible flows. This review will concentrate on the aeroelastic mechanisms which are most likely to be encountered in the axial compressor environment. These are the interaction between shocks and flow separations for transonic flows and unsteady flow separation for compressible, subsonic flows.

The physics of unsteady shock motion and shock induced separation was reviewed by Lee (2001). There are a number of complex interactions between shocks and flow separations for airfoils operating in transonic flow conditions. In general, a shock wave can trigger a localized boundary layer separation. The separation induced by the shock results in a strong fluctuating pressure on the surface of the airfoil. The peak in this fluctuating pressure occurs just downstream of the shock, at the beginning of the region of flow separation. The presence of a shock induced flow separation upstream of the trailing edge may, under certain circumstances, trigger a separation bubble upstream of the trailing edge. Sufficiently strong shocks can perturb the flow such that the two regions of separated flow merge. The conditions for the oscillation of the shock in both position and magnitude occur within a narrow range of flow velocities associated with the merging of these two separation regions. The feedback mechanism which induces unsteady shock motion can be described as follows. At the trailing edge, the flow separation results in fluctuations of static pressure within the wake. These pressure disturbances propagate upstream and interact with the shock wave, inducing shock movement (Lee (2001)). A change in shock position alters the momentum of the flow at the trailing edge, causing the wake region to deflect. However, there is a phase lag between the perturbation in wake pressure at the trailing edge and the corresponding shock motion. The phase lag, coupled with the unsteady flow at the trailing edge are the proposed mechanisms which explain the shock oscillation phenomena. This phenomena is only observed within a small range of Mach numbers for rigidly supported airfoils. This oscillation can occur when the Mach number upstream of the shock is within $1.22 \leq M \leq 1.3$ (Lee (2001)).

Low Mach numbers result in weak shocks which do not induce trailing edge separation. High Mach numbers result in strong shocks which tend to stabilize the wake static pressure. Finally, it is noted that the pressure perturbations which interact with the shock travel outside of the separated flow region.

Yamasaki et al. (2004) investigated the shock-stall flutter of a supercritical airfoil commonly found on high-speed aircraft. The airfoil was allowed to oscillate in pitching only. This motion resulted in a complex interaction between a shock located on the suction surface and the trailing edge separation. The behavior of the airfoil under this type of flutter was found to have a nonlinear dependence on the dynamic pressure at constant Mach number. Specifically, there exist a critical dynamic pressure for which the amplitude of the oscillations dramatically increased. The use of schlieren photography and numerical simulations revealed a complex dependency between the unsteady aerodynamic forces, the unsteady shock motion and the structure of the wake. At high instantaneous angles of attack, the shock-induced flow separation resulted in a von-Karmán vortex shedding in the wake. This resulted in a large energy transfer from the flow to the airfoil. At low instantaneous angles of attack, this vortex-shedding was not present. In both cases, the shock was found to be stabilizing (transferring energy from the airfoil to the flow).

Bouhadji and Braza (2003) numerically investigated the unsteady separation of supercritical airfoils at a variety of Mach numbers. Similar to the results presented by Yamasaki et al., von-Karmán vortex shedding was observed in the wake of the airfoil. However, their numerical simulations predicted vortex shedding at low angles of attack and low Mach numbers (as low as M=0.35). The unsteady pressure on the surface of the airfoil triggered a shock oscillation at Mach numbers greater than 0.7. The frequency of shock oscillation was much lower than the vortex shedding frequency. The deflection of the wake associated with the unsteady shock oscillation appeared to be consistent with observations by Lee and Yamasaki et al.

Schewe et al. (2003) and Dietz et al. (2006) investigated the shock-stall flutter behavior of a supercritical airfoil with two degrees of freedom using experimental measurements and numerical simulations. The airfoils were allowed to oscillate in both plunging motion and pitching motion. In addition to Mach number, these studies also investigated the effect of vibration amplitude on the stability of the aeroelastic system. It was found that multiple stable oscillatory states exist for the shock-stall flutter investigated. These states could be reached by perturbing the system with a sufficiently large structural disturbance. There exist a substantial change in the flow between the two stable limit cycle oscillations. The smaller amplitude limit cycle oscillation resulted from a weak interaction of the shock with the trailing edge separation. The flow over the airfoil was primarily attached. The large amplitude limit cycle resulted from a strong coupling between the unsteady trailing edge separation and the shock.

These studies show that there are two mechanisms which can interact to generate self-limiting aeroelastic oscillations of airfoils in compressible flow. The von-Karmán vortex shedding observed by Yamasaki et al. and Bouhadji and Braza can result in self-sustained, self-limited airfoil oscillations at low flow velocities. An increase in flow velocity results in the formation of shocks, the interaction of which with the pressure at the trailing edge can also induce stable oscillations. Shocks appear to be stabilizing while separated flow appears to be destabilizing. It should be noted that all these studies considered airfoils which approximate the response of wings associated with high speed commercial transport aircraft. To the author's knowledge, the interaction of these effects on structures where three-dimensional effects are strong (such as low aspect ratio cantilevered blades typically found in axial compressors) has not been investigated. It is clear from Chapter 1 that there exist some commonality between the mechanisms present in axial compressor flutter

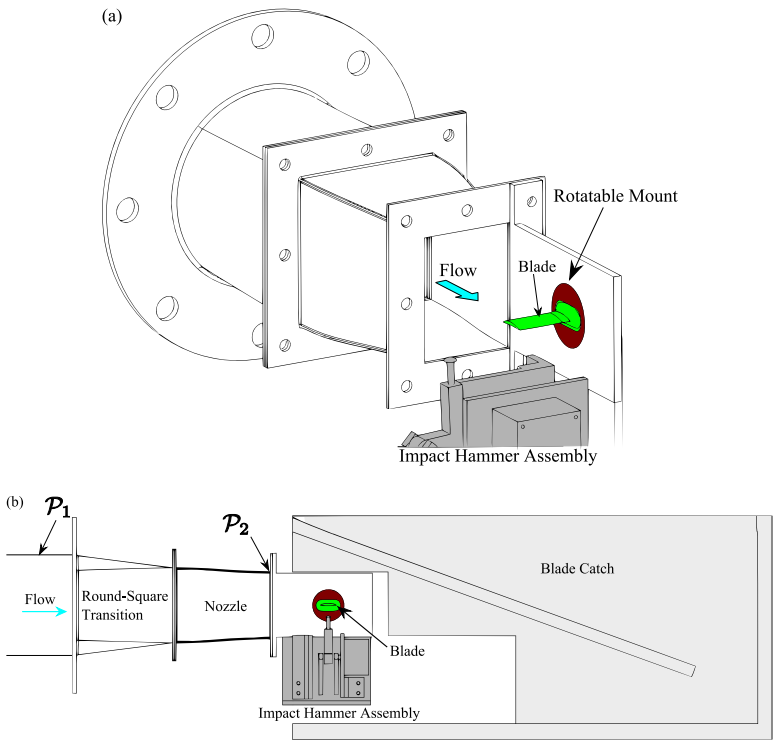

Figure 31: Schematic of experimental setup. (a) Isometric view of test section including blade mount. Note that the blade can be pitched to any angle of attack using the flush-mounted circular mounting plate. Blade-catch is omitted for clarity. (b) Cross-sectional view of complete blowdown assembly.

and transonic airfoil flutter (such as unsteady shock motion and flow separation). The study of these mechanisms in the context of a single cantilevered wing which approximates a typical axial compressor blade will be the subject of this chapter. A description of the experimental setup will be the topic of the next section. This will be followed by exploratory measurements of structural response of the cantilevered wing to compressible, subsonic flow.

4.3 Experimental Approach

The aeroelastic behavior of a cantilevered blade was investigated using a high-speed open jet. The high speed jet facility is an open jet blow-down tunnel. A description of the facility can be found in Walker (1997). The test section consisted of a single plate with a flush-mounted blade mount capable of pitching the blade about its chord. A schematic of the nozzle and test section can be seen in figure 31. The blade was exposed to a uniform rectangular jet. A "Blade Catch" was mounted downstream of the test section to contain any debris in the event of blade structural failure. Two exit nozzles were used for this study. The first nozzle had a rectangular exit of dimension 76×102 mm. This nozzle could sustain $\mathcal{M} \approx 0.6$ flows for ≈ 45 seconds and was used to investigate the aeroelastic response of a canonical compressor blade without an endwall. The second nozzle had a rectangular exit of dimension 51×102 mm and could sustain $\mathcal{M} = 1$ flow for ≈ 30 seconds. A 25 mm thick plexiglas plate was affixed in the vicinity of the blade tip to simulate the end-wall effects and tip flow common to rotor blades. The gap between the blade tip and the plexiglas wall was 0.48mm, approximately 2% of the chord.

The Mach number and flow velocity were estimated from static pressure and temperature measurements taken at

duct locations $\mathcal{P}_1$ and $\mathcal{P}_2$. The exit Mach number was estimated using the relationships between the throat properties ($\mathcal{P}_2$) and the properties at the reference location ($\mathcal{P}_1$) for the isentropic flow of a compressible perfect gas in a duct. The relationship between two areas and the local Mach numbers are given by

$$\frac{A_1}{A_2} = \frac{\mathcal{M}_1}{\mathcal{M}_2}\left[\frac{1+\frac{\gamma-1}{2}\mathcal{M}_2^2}{1+\frac{\gamma-1}{2}\mathcal{M}_1^2}\right]^{\frac{\gamma+1}{2(\gamma-1)}}. \tag{48}$$

The static pressures have a similar relationship,

$$\frac{\mathcal{P}_1}{\mathcal{P}_2} = \left[\frac{1+\frac{\gamma-1}{2}\mathcal{M}_2^2}{1+\frac{\gamma-1}{2}\mathcal{M}_1^2}\right]^{\frac{\gamma}{\gamma-1}}. \tag{49}$$

Note that these relations yield a closed form solution for the ratio of Mach numbers. The problem is completely specified when the static pressure at the nozzle exit is known and by considering only $0.1 \leq \mathcal{M}_1, \mathcal{M}_2 \leq 1$. The ambient lab pressure was assumed to approximate the static pressure at the nozzle exit. The pressure difference was estimated by measuring the difference between a single static pressure port upstream of the round-square transition (point $\mathcal{P}_1$ in figure 31) and the manifold pressure of 5 interconnected static pressure ports located at the nozzle exit (point $\mathcal{P}_2$). Static temperature which was measured by a thermistor was also acquired at point $\mathcal{P}_1$. The static temperature measurement enabled the estimation of the density (and thus the velocity) in the duct.

An advantage of performing aeroelastic measurements in an open jet facility is that the damage to equipment associated with wing/airfoil failure can be reduced substantially with relatively little effort. An approach to damage mitigation in the event of blade failure is to construct a "blade-catch". The objective is to collect and sequester high velocity debris in a predictable manner. The blade catch which was used for the experiments conducted in this facility is shown in figure 31(b). The blade-catch was designed such that blade failure will not pose a significant risk to the operator or the facility.

The test section was equipped with a impulsive loading mechanism. This device was a four-bar mechanism designed to impart a spatially concentrated, short time duration mechanical load on the structure. The device is shown schematically in figure 32. The general principle of operation can be described as follows. The impactor initially deflects the blade by a pre-determined amount. The magnitude of the deflection can be controlled by changing the height of the impactor, h. The change in load when the impactor slips off the tip of the blade approximates a step function. At moderate impactor speeds this loading approximated an impulse.

The mechanism was driven by a servomotor. The use of a servomotor with a pre-programmed motion profile improves experiment consistency when compared to conventional impulse response tests. Furthermore, the ability to conduct impulse response tests remotely allows for the measurement of the response of structures in environments which are otherwise inaccessible (such as in a vacuum chamber or in high speed flows where blade failure may pose a significant risk to the operator).

All structural vibration data presented here was acquired using a single point Laser Doppler Vibrometer (LDV). The LDV utilizes the Doppler effect to estimate the velocity of a surface perpendicular to the beam. Reflective tape was affixed to the surface of the blade to improve measurement accuracy. The area of the tape was much smaller than the

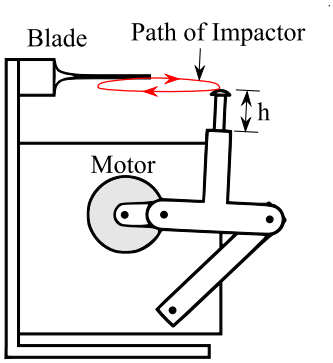

Figure 32: Schematic of impulsive loading mechanism and general orientation with respect to the test blade.

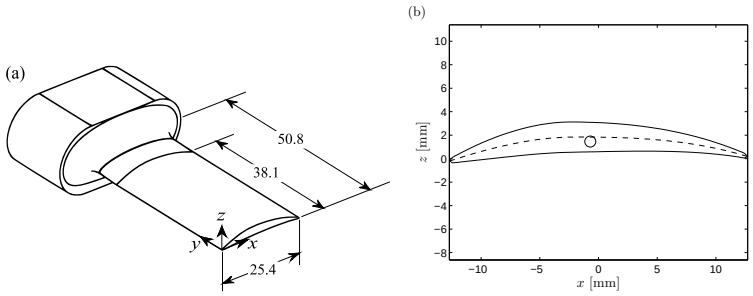

Figure 33: Geomtery of airfoil used in exploratory measurements. All dimensions in mm. (a) Isometric view of blade geometry. (b) Blade cross section at $\alpha_0 = 0^o$. $--$ indicates camber line, $\circ$ is the approximate location of the elastic axis for the cross-section.

planform area of the blade (the area ratio is $\approx 1:22$ tape:blade). Consequently, the effect of the reflective tape can be considered negligible. The minimum accuracy for all structural velocity measurements presented here was 170μm/s.

The flow was characterized using PIV. A 2048×2048 pixel Imager Pro X 4M CCD camera and double pulse Nd:YAG laser were mounted to a metal frame. The frame affixed to a linear slide which enabled the camera and laser to be traversed along the span of the blade. This allowed for measurement at multiple span-wise locations without requiring re-calibration of the camera and re-alignment of the laser.

The camera's field of view was 80×80 mm resulting in a spatial resolution of 23.7 pixels/mm. The camera was calibrated using a curved calibration plate located on the inside of the casing window with marks placed uniformly in the axial and circumferential directions. A 3^{rd} order polynomial fit was used to correct for image distortion from the camera's lens. The polynomial fit had an rms of 0.1 pixels. The Δt between images was set to 6μs.

Two approaches were used in the processing of PIV data. The first approach was used to characterize the flow from the 76×102 mm nozzle without a blade. A multipass approach was used. The initial and final window sizes were 64×64 and 32×32 pixels and were overlapped by 50% of the window size. The windows were weighted with an axisymmetric Gaussian function. Vector validation was performed. The validation consisted of removal of vectors which deviated by more than three times the RMS of the neighboring vectors and the rejection of any vectors which indicated reversed flow. Note that the jet spanned the camera's field of view and as such no flow reversal was expected for the jet. These operations resulted in a spatial resolution of 1.5 vectors/mm.

The second approach was used to investigate flow about the blade. The images were first processed by applying a sliding-background-subtraction algorithm. A Gaussian blurring filter was then applied. A multipass approach was used. The initial and final window sizes were 32×32 and 16×16 pixels respectively and were overlapped by 50% of the window size. An axisymmetric Gaussian weighting function was also applied to the windows. The vector validation used in this investigation was identical to the one used in the characterization of the nozzle flow. The resultant vector field was post-processed in the following manner. An interpolation algorithm was used to estimate the fluid velocity for most of the rejected vectors. Note that vectors which were located inside the cross-section of the blade were not used for interpolation. The number of rejected vectors was less than 3% of the total number of vectors. A spatial smoothing filter was then applied. These operations resulted in accurate velocity estimates with a spatial resolution of 3 vectors/mm. Note that the post-processing operations were performed to allow for the estimation of the flow vorticity.

The geometry of the canonical compressor blade used in this study is shown in figure 33. Figure 34 shows the shape of the first four eigenmodes of vibration for this geometry. The cross-section of the blade was constant over the outer 75% of the span. Two blades were made of different materials. Table 3 describes some of the mechanical properties of the materials used. The natural frequencies of the first four modes ($[\boldsymbol{f}]_1$ and $[\boldsymbol{f}]_2$) were similar because the ratio E/ρ_s was nearly identical between both materials. Furthermore, the ratio between fluid density ρ_a and structural density ρ_s, was similar in magnitude between the two materials. As a result, the "added mass" effect due to the presence of fluid can be considered negligible for both blades. Consequently, the only substantial difference between the aeroelastic systems when using these blades was the structural stiffness.

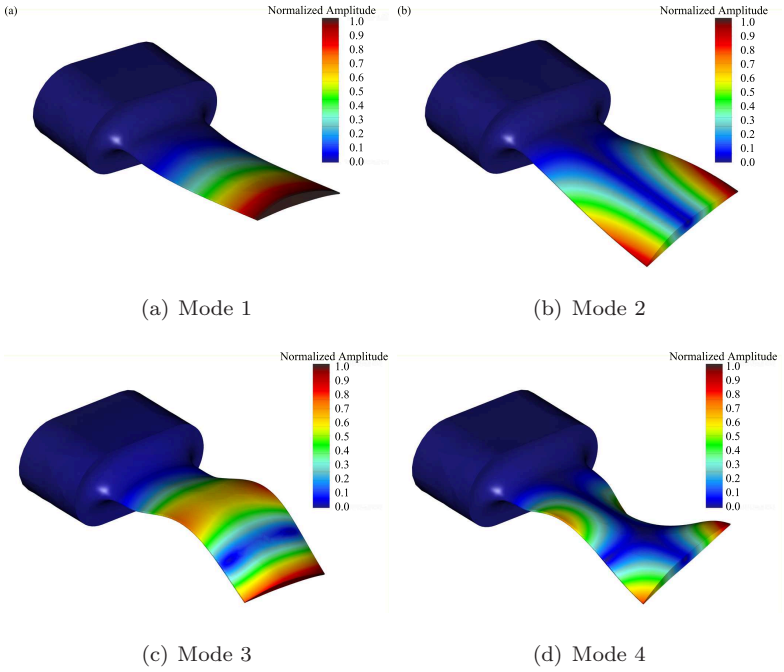

(a) Mode 1 (b) Mode 2

(c) Mode 3 (d) Mode 4

Figure 34: First four mode shapes of the blade.

Table 3: Material and properties of the two blades used.

	6061-T6 AL	A2 Tool Steel
E [GPa]	68.9	203
ρ_s [kg/m^3]	2700	7860
$\frac{E}{\rho_s}$	2.55×10^7	2.58×10^7
$[\boldsymbol{f}]_1$ [Hz]	1150	1160
$[\boldsymbol{f}]_2$ [Hz]	3820	4070
$[\boldsymbol{f}]_3$ [Hz]	6,370	6,500
$[\boldsymbol{f}]_4$ [Hz]	12,220	12,700

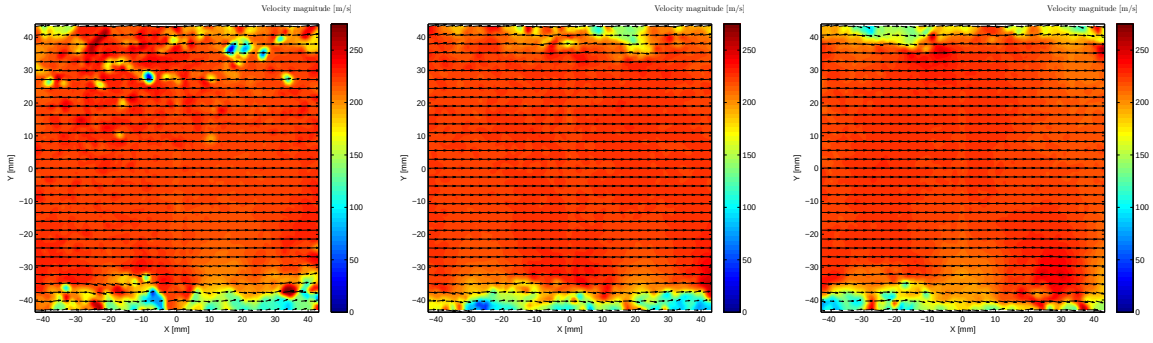

(a) Blade root. (b) Mid-span. (c) Blade tip.

Figure 35: Flow field produced by the 76×102mm nozzle at three spanwise locations and $\mathcal{M} \approx 0.6$. Isocontours represent velocity magnitude. The blade (which was not present for these measurements) mounted at $x = y = 0$ mm.

4.4 Results

The data presented in this section can be divided into four distinct investigations. The first is the characterization of the flow field in which the blade was immersed. This was performed to ensure that the flow which the blade was exposed to was spatially uniform. The second study described the the modal amplitude of blade vibration due to steady flow. The characteristics of the modal amplitudes can provide insight into the aerodynamic mechanisms which were responsible for the structural excitation at a given set of flow conditions. The third investigation characterized the damping of the blade due to the material, the mount on which the blade was attached and the aerodynamic damping. The damping provides a general measure which quantifies the stability of the aeroelastic system to a small disturbance. The fourth investigation studied the response of the system to a large disturbance. The disturbance was provided by the impulsive loading mechanism. The characteristics of this response provides a measure of the global stability of the aeroelastic system. Note that it has been observed that the flow mechanism which drives the aeroelastic response can change dramatically if subjected to a large disturbance.

4.4.1 Characterization of the mean flow

The flow field at the nozzle exit was characterized using PIV. This study was performed to determine if there were any coherent flow structures being generated upstream of the blade. A coherent flow structure which is advected over the blade can induce unsteady forces. The variation of these unsteady forces with respect to Mach number and angle of attack can be coupled to the object which is generating these flow structures. The variation in blade aerodynamic response with respect to Mach number may reflect not only the aeroelastic response of the blade at a given flow condition, but also the forcing. Thus, it is desirable to minimize the amount of forcing which is not associated with the blade.

The a snapshot of the fluid velocity at three spanwise locations for the 76×102mm nozzle is shown in figure 35. The root corresponds to 25% of the blade span as measured from the fillet at the base. It can be observed that the only large scale flow structure present at all three spanwise locations were the shear layers associated with the edges of the jet. The shear layers were more than 1.5 chord-lengths away from the blade surface in the $y-$direction. This separation was sufficiently large such that the presence of the shear layers did not have a significant influence the aeroelastic response of the blade. In addition, the flow-field at the tip and root were quantitatively similar to the flow field observed at mid-span.

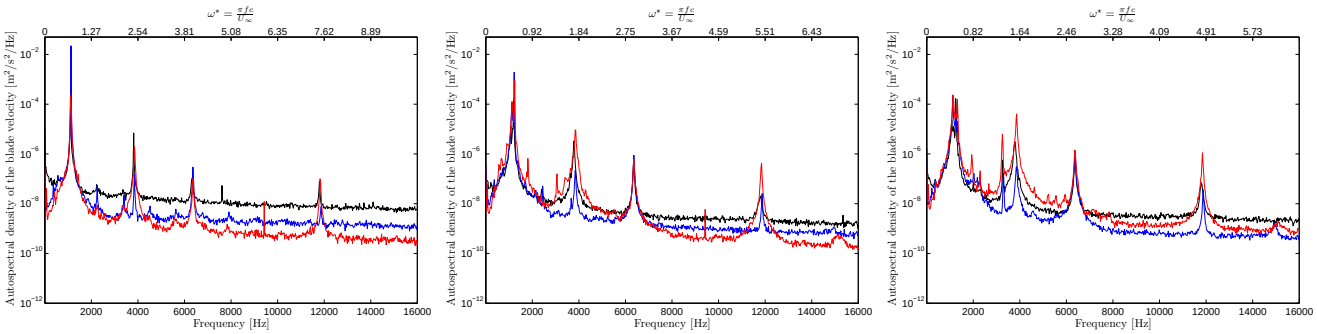

(a) $\mathcal{M} \approx 0.4$ (b) $\mathcal{M} \approx 0.51$ (c) $\mathcal{M} \approx 0.6$

Figure 36: Power spectral density of the blade surface velocity as a function of Mach number for the Aluminum blade in a uniform jet without an end-wall. – $\alpha_0 = 0.8^o$, – $\alpha_0 = 5.2^o$, –$\alpha_0 = 10.1^o$.

Thus, it can be concluded that the jet in which the blade was immersed was spatially uniform.

4.4.2 Steady response

The structural response of the blade in a steady, compressible, uniform flow was investigated. The autospectral density of the blade surface velocity as measured by the LDV is presented in figure 36 for the aluminum blade and figure 37 for the steel blade for several Mach numbers and angles of attack. Note that these spectra were obtained without an end-wall. The parameter α_0 was defined as the angle between the chord-line and the flow at zero fluid velocity. It should be noted that the presence of a steady aerodynamic load resulted in a deflection of the blade, which changed the mean angle of attack at non-zero fluid velocities. This angle is not reflected in the results presented here.

The following observations can be made regarding the behavior of the Aluminum blade. Nearly all of the vibration energy is concentrated at frequencies corresponding to the first four blade eigen-modes of vibration. An increase in α_0 from 0.8^o to 5.2^o for a flow velocity of $\mathcal{M} \approx 0.4$ (figure 36 (a)) resulted in a significant increase in the magnitude of the response of the first mode and a decrease in the response of the second and fourth modes. A further increase in α_0 to 10.1^o at this flow speed resulted in responses similar in magnitude as those observed for $\alpha_0 = 0.8^o$.

The spectra at $\mathcal{M} \approx 0.5$ (figure 36 (b)) show substantial differences from those observed at $\mathcal{M} \approx 0.4$. Specifically, the response for the fourth mode showed a significant increase at $\alpha_0 = 10.1^o$ compared to the observations at $\mathcal{M} \approx 0.4$. In contrast, the magnitude of the response of this mode at lower angles of attack decreased when the Mach number was increased. Finally, it should be noted that the relative width of all four peaks increased with an increase in Mach number.

The spectra of blade surface velocity at $\mathcal{M} \approx 0.6$ can be seen in figure 36 (c). There were several fundamental changes in the observed spectra at this Mach number. First, a peak appeared at 3.5 kHz (with a reduced frequency of $\omega^\star \approx 1.35$). This peak was present at all angles of attack investigated. Note that the magnitude of this peak varied with the magnitude of the second mode. The maximum response for this peak and the second mode was observed at $\alpha_0 = 10.1^o$, whereas the minimum response occurred at $\alpha_0 = 5.2^o$. Significant changes in the width of these peaks was observed as the angle of attack was varied. In addition, the peak associated with the first mode bifurcated into two distinct peaks. This was accompanied by a reduction in the magnitude of the response of this mode. Note that the magnitude of the response for this mode showed minor variation over the range of α_0 tested.

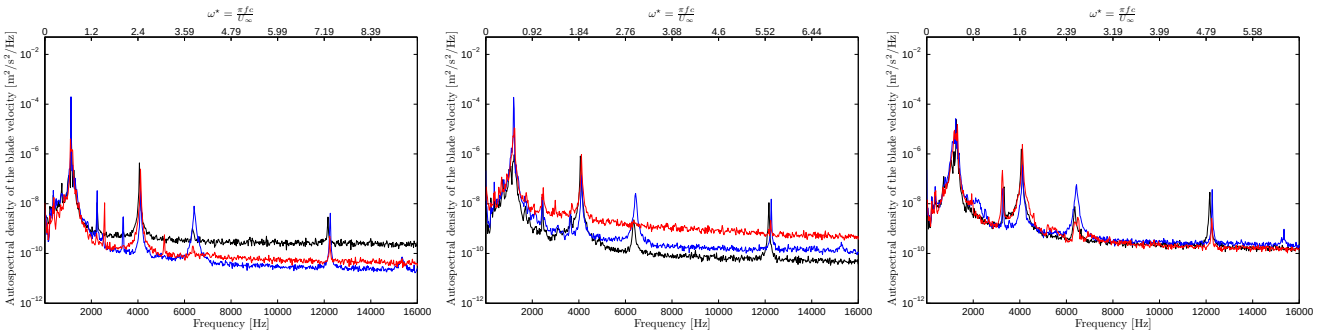

(a) $\mathcal{M} \approx 0.41$ (b) $\mathcal{M} \approx 0.48$ (c) $\mathcal{M} \approx 0.6$

Figure 37: Autospectral density of the blade surface velocity as a function of Mach number for the Steel blade in a uniform jet without an end-wall. – $\alpha_0 = 0.8^o$, – $\alpha_0 = 5.2^o$, –$\alpha_0 = 10.1^o$.

The following observations can be made regarding the behavior of the Steel blade. At Mach 0.4 (figure 37 (a)), the magnitudes of the response at the first two modes had a similar trend to that observed for the Aluminum blade as the angle of attack was varied. Specifically, the magnitude of the response for the first mode was large at $\alpha_0 = 5.2^o$ and relatively small at $\alpha_0 = 0.8^o$ and 10.1^o. A similar decrease in the magnitude of the response for the second mode was observed at $\alpha_0 = 5.2^o$. Note that except at $\alpha_0 = 5.2^o$ the response of the blade in the third and fourth modes was much smaller than the response observed for the first two modes. Finally, it should be noted that the overall response for the Steel blade was much smaller than the Aluminum blade.

An increase of the Mach number to 0.5 did not result in many significant changes in the observed response of the steel blade. Note that peak associated with the first mode of the blade bifurcated into two distinct peaks when $\alpha_0 = 0.8^o$. This bifurcation was not observed when α_0 was increased. The magnitude of the response at the eigen-frequencies of the blade, as well as the width of the peaks were comparable to those observed for the steel blade at $\mathcal{M} \approx 0.4$. Recall that for the Aluminum blade, an increase in Mach number from 0.4 to 0.5 resulted in a large decrease in the magnitude of the response for the first mode as well as a widening of the peaks associated with all four modes. This suggests that the aeroelastic interactions observed in this range of Mach numbers were dependent upon the amplitude of structural vibration.

The response of the steel blade at a Mach number of 0.6 was significantly different from the observed response at $\mathcal{M} \approx 0.5$. Note that a peak at 3.5 kHz appeared, which was consistent with the response of the Aluminum blade at the same Mach number. In addition, the spectra of the surface velocity was not significantly influenced by the angle of attack of the blade. Note that an exception to this observation occurred for the third mode at $\alpha_0 = 5.2^o$. The response of this mode at this flow condition was significantly larger than at $\alpha_0 = 0.8^o$ and 10.1^o. A comparison of the response with the Aluminum blade at the same Mach number revealed that the variation in magnitude of the response with angle of attack for the second and fourth modes were significantly reduced when the blade stiffness was increased.

The mean-squared modal amplitude of the blade response in first bending as a function of zero-flow angle of attack (α_0), Mach number ($\mathcal{M}$) and reduced frequency ($\omega^\star$) is presented in figure 38(a) for Aluminum and figure 38(b) for Steel. A brief segment of the corresponding time-dependent blade vibration velocity, normalized by the root-mean-squared amplitude $[\sigma_\zeta]_1$ is presented in figure 39 for Aluminum and 40 for Steel. Note that these data were acquired without an end-wall.

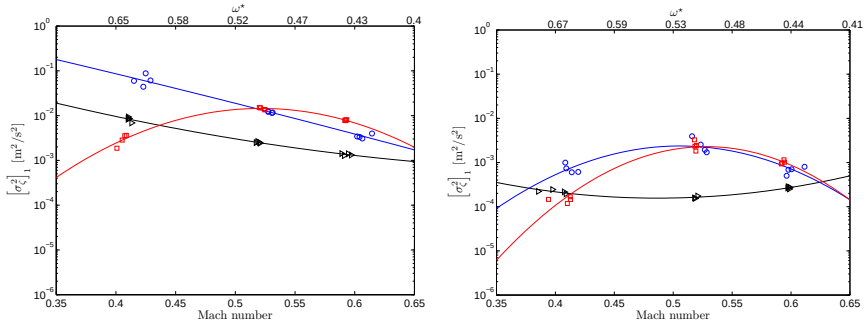

Figure 38: Mean-squared amplitude of the first mode vibration for the blade in a uniform jet without an end-wall as a function of Mach number, $\omega^\star$ and zero flow angle of attack. $\triangleright$ – $\alpha_0 = 0.8^o$, $\circ$ – $\alpha_0 = 5.2^o$, $\square$ – $\alpha_0 = 10.1^0$. Lines are included to show general trend of data. (a) Aluminum blade. (b) Steel blade.

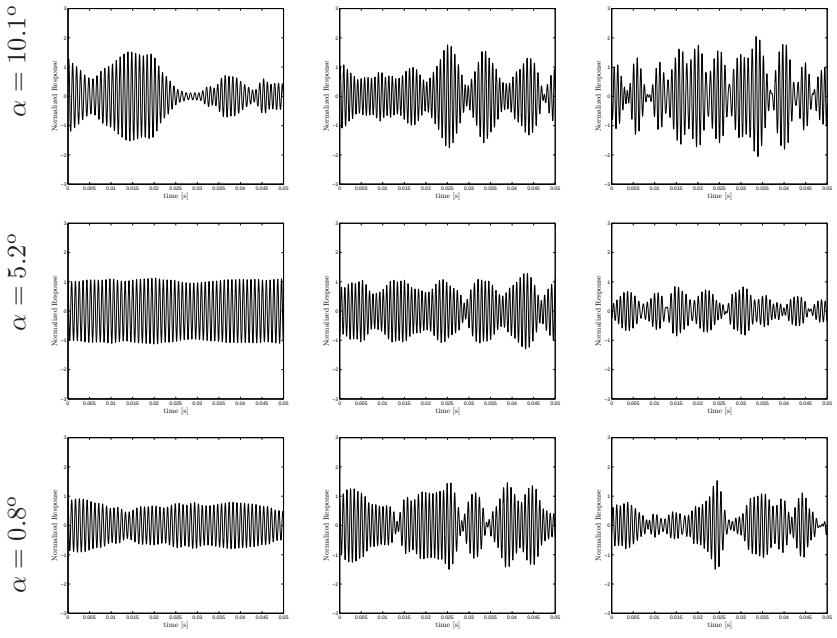

$\mathcal{M} \approx 0.44$ $\omega^\star \approx 0.59$ | $\mathcal{M} \approx 0.54$ $\omega^\star \approx 0.48$ | $\mathcal{M} \approx 0.6$ $\omega^\star \approx 0.43$

Figure 39: Steady response of the Aluminum blade without end-wall in the first mode to a uniform jet without an end-wall as a function of Mach number and zero-flow angle of attack.

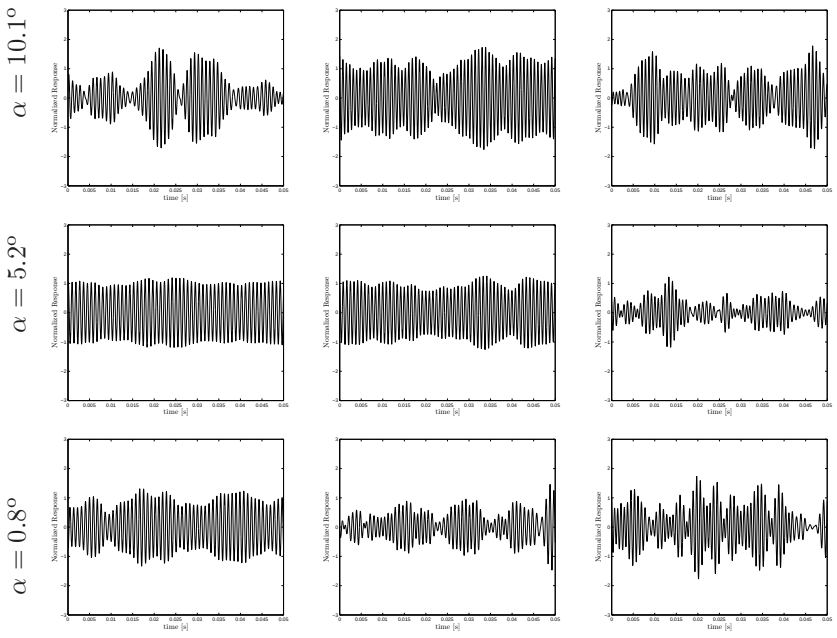

$\mathcal{M} \approx 0.44$ $\mathcal{M} \approx 0.54$ $\mathcal{M} \approx 0.6$

$\omega^\star \approx 0.60$ $\omega^\star \approx 0.49$ $\omega^\star \approx 0.44$

Figure 40: Steady response of the Steel blade in the first mode to a uniform jet without an end-wall as a function of Mach number and zero-flow angle of attack.

The trends in $\left[\boldsymbol{\sigma}_{\boldsymbol{\zeta}}^{\mathbf{2}}\right]_1$ for the Aluminum blade at several angles of attack and Mach numbers/reduced frequencies can be summarized as follows. The lowest angle of attack investigated showed a reduction of the mean-squared amplitude of vibration as the Mach number was increased. The time-series showed an increase in vibration amplitude intermittency associated with this trend. The largest amplitude response of the blade at this angle of attack occured at a reduced frequency of $\omega^\star \approx 0.63$, corresponding to a Mach number of $\mathcal{M} \approx 0.44$.

An increase in α_0 to 5.2° resulted in a nearly uniform shift of the trend observed for $\alpha_0 = 0.8^o$ up by a factor of nearly 6. The time-series of the blade response also showed an increase intermittency with increased Mach number. In contrast to the $\alpha_0 = 0.8^o$ time-series data, the response at $\alpha_0 = 5.2^o$ appeared to be amplitude modulated. The reduced frequency of this amplitude modulation was $\omega^\star_{\text{AM}} \approx 0.043$ when $\mathcal{M} \approx 0.54$ and $\omega^\star \approx 0.49$. This increased to $\omega^\star_{\text{AM}} \approx 0.046$ when $\mathcal{M} \approx 0.6$ and $\omega^\star \approx 0.44$. The similar dependence of $\left[\boldsymbol{\sigma}_{\boldsymbol{\zeta}}^{\mathbf{2}}\right]_1$ on Mach number/reduced frequency suggest that the mechanism responsible for the excitation was similar between the two angles of attack.

A further increase in α_0 resulted in a significant change in the trend of $\left[\boldsymbol{\sigma}_{\boldsymbol{\zeta}}^{\mathbf{2}}\right]_1$. The response at $\mathcal{M} \approx 0.44$ ($\omega^\star \approx 0.59$) was much smaller than those observed for lower angles of attack. The time-series response of the blade at this set of flow conditions was characterized by long periods of small amplitude vibration with brief periods of high-amplitude vibration randomly interspersed. Furthermore, the response amplitude was self-limiting at high Mach numbers and low reduced frequencies with respect to α_0. The time-series response of the structure was qualitatively similar to the $\alpha_0 = 5.2^o$ response for $\mathcal{M} \geq 0.50$. Specifically, the amplitude modulation of the structural response in the first mode was quasi-periodic with a reduced frequency of $\omega^\star_{\text{AM}} \approx 0.048$ when $\mathcal{M} \approx 0.54$ and $\omega^\star \approx 0.48$. This increased to $\omega^\star_{\text{AM}} \approx 0.078$ for $\alpha_0 = 10.1^o$. The similarities between the trends observed in the time-series data and the mean-squared amplitude again

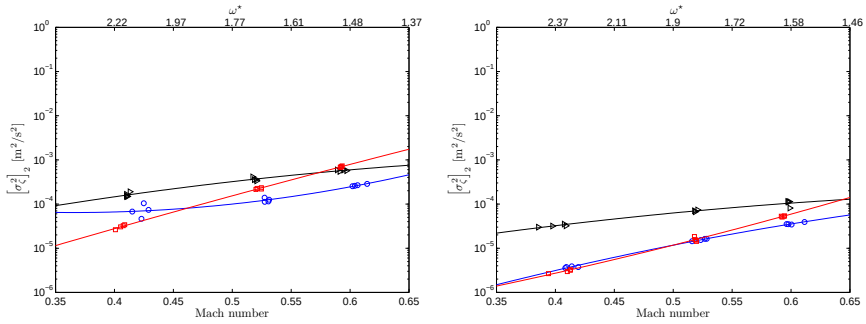

Figure 41: Mean-squared amplitude of the second mode vibration for the blade in a uniform jet as a function of Mach number, $\omega^\star$ and zero flow angle of attack. $\triangleright$ – $\alpha_0 = 0.8^o$, $\circ$ – $\alpha_0 = 5.2^o$, $\square$ – $\alpha_0 = 10.1^0$. Lines are included to show general trend of data. (a) Aluminum blade. (b) Steel blade.

suggest that there is some commonality between the aeroelastic interactions associated with the high α_0, high $\mathcal{M}$ for the Aluminum blade.

The effect of increased blade stiffness resulted in a significant change in the trends observed in $\left[\boldsymbol{\sigma}^{\mathbf{2}}_{\boldsymbol{\zeta}}\right]_1$. The dependence of $\left[\boldsymbol{\sigma}^{\mathbf{2}}_{\boldsymbol{\zeta}}\right]_1$ on Mach number and reduced frequency was weak at $\alpha_0 = 0.8^{\text{o}}$. Note that for the Aluminum blade, the mean-squared amplitude decreased by nearly an order of magnitude over the Mach number range observed. There was an increase in vibration intermittency as the Mach number was increased (cf. figure 40). These two observations imply that, although the time-series data are similar, the increase in blade stiffness had a much stronger influence than Mach number and reduced frequency effects at this angle of attack.

Increasing the angle of attack to 5.2^{o} yielded a dependence of mean-squared amplitude on the Mach number and reduced frequency. In contrast to the Aluminum blade response, the peak amplitude of vibration occurred for a Mach number of 0.54 ($\omega^\star \approx 0.49$). In addition, significant vibration intermittency was only observed at the highest Mach number tested. The intermittency was qualitatively different from the Aluminum blade response in that it appeared to be stochastic, rather than quasi-periodic.

The blade stiffness had a small effect on the structural response at $\alpha_0 = 10.1^{\text{o}}$. The dependence of mean-squared amplitude of vibration on Mach number and reduced frequency appeared to be similar between both materials. The time-series response showed qualitatively similar behavior. The most striking similarity was that $\left[\boldsymbol{\sigma}^{\mathbf{2}}_{\boldsymbol{\zeta}}\right]_1$ was a weak function of α_0 at $\mathcal{M} \geq 0.5$ and $\alpha_0 \geq 5.2^{\text{o}}$. This implies that the physical process which produces this effect was not strongly dependent on blade stiffness. Note that for the Steel blade, the intermittency was lower than for the Aluminum blade. Finally, it should be noted that the trend of mean-squared amplitude with respect to Mach number and reduced frequency for the steel blade at $\alpha_0 = 5.2^{\text{o}}$ was qualitatively similar to the trend found at $\alpha_0 = 10.1^{\text{o}}$. There is a peak in both responses at $\mathcal{M} \approx 0.55$.

An analysis of the time-varying modal amplitude of the steady response was performed. The modal amplitude was assumed to be of the form

$$[\zeta(t)]_p \equiv [Z(t)]_p e^{\mathrm{j}\omega_p t} \tag{50}$$

where $[Z(t)]_p$ is the time-varying magnitude of $[\zeta(t)]_p$ and ω_p is the circular frequency of vibration of the mode. Note

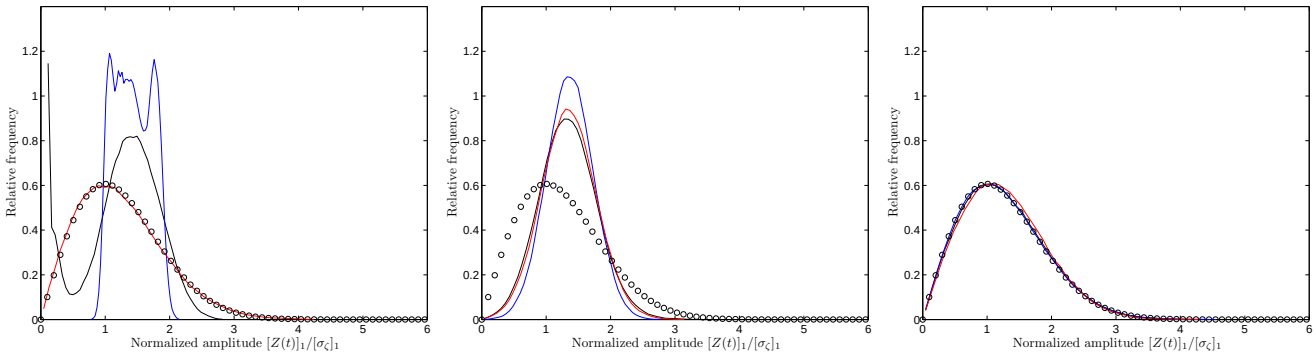

(a) $\mathcal{M} \approx 0.40$ (b) $\mathcal{M} \approx 0.51$ (c) $\mathcal{M} \approx 0.60$

Figure 42: Probability distribution function of the magnitude of $[\zeta(t)]_1$ as a function of Mach number for the Aluminum blade. – $\alpha_0 = 0.8^o$, – $\alpha_0 = 5.2^o$, –$\alpha_0 = 10.1^o$.

that $\jmath \equiv \sqrt{-1}$. The magnitude of the modal amplitude was estimated in the following manner. First, a Hilbert transform was applied to $[\zeta(t)]_p$. The magnitude of this result yielded $[Z(t)]_p$. Figure 42 showa the probability distribution function of $[Z(t)]_p$ for the first mode of the Aluminum blade at several α_0 and $\mathcal{M}$, whereas figure 43 shows the pdfs for the Steel blade. Note that the abcissa has been normalized by the standard deviation of $[\zeta(t)]_p$. Also included is a Rayleigh distribution, which is the expected distribution if $[Z(t)]_p$ varies randomly (Bendat and Piersol (2000)).

There are several important features which can be observed for the histograms of $[Z(t)]_1$ for the aluminum blade. There was a dramatic change in the pdf at $\mathcal{M} \approx 0.4$ when the angle of attack was changed. The pdf at $\alpha_0 = 10.1^o$ can be approximated using the standard Rayleigh distribution. A reduction in α_0 to 5.2^o resulted in a uniform distribution, centered at $[Z(t)]_1/\sigma_Z \approx 1.4$. The implication is that $[Z(t)]_1$ fluctuated with equal probability about the mean, which was consistent with the observed time-varying modal amplitudes shown in figure 39. The magnitude of these fluctuations was about 50% of $\left[\boldsymbol{\sigma}_{\boldsymbol{\zeta}}^{\mathbf{2}}\right]_1^{1/2}$. The pdf at $\alpha_0 = 0.8^o$ was substantially different from those observed at the other angles of attack. Two peaks can be observed at $[Z(t)]_1/[\sigma_\zeta]_1 \approx 0$ and 1.5. This suggests that the amplitude of vibration at this flow condition varied between a constant amplitude oscillation and periods of no vibration.

An increase in flow velocity to $\mathcal{M} \approx 0.5$ resulted in substantial changes in the pdfs. It can be seen that the pdfs were nearly identical in shape, regardless of the angle of attack. In addition, the pdfs were similar to a Gaussian distribution, centered about $[Z(t)]_1/[\sigma_\zeta]_1 \approx 1.4$. This implies that the vibration amplitude had small, random fluctuations about a mean value. An increase of the flow velocity to $\mathcal{M} \approx 0.6$ also resulted in a substantial change in the shape of the pdfs. Here, the pdf of $[Z(t)]_1$ was similar to a Rayleigh distribution, regardless of the angle of attack. This implies that the amplitude of vibration varied randomly with respect to time.

An increase in blade stiffness also resulted in a change in the shape of the pdfs. The following can be observed at $\mathcal{M} \approx 0.4$. The pdf at $\alpha_0 = 0.8^o$ had two peaks. Note that the centers of each peak are at $[Z(t)]_1/\sigma_Z = 0.75$ and 2.5. This implies that there were two preferred values of $[Z(t)]_1$, and that the amplitude of vibration varied between these two values. An increase in α_0 to 5.2^o resulted in a Gaussian pdf centered at a normalized amplitude of 1.4. The implication is that at this flow condition the vibration amplitude had small fluctuations about a non-zero mean value. A further increase in the angle of attack resulted in a pdf which was qualitatively similar to a Rayleigh distribution. Note that the distribution differs from the Rayleigh distribution because it had a larger tail at large normalized amplitude.

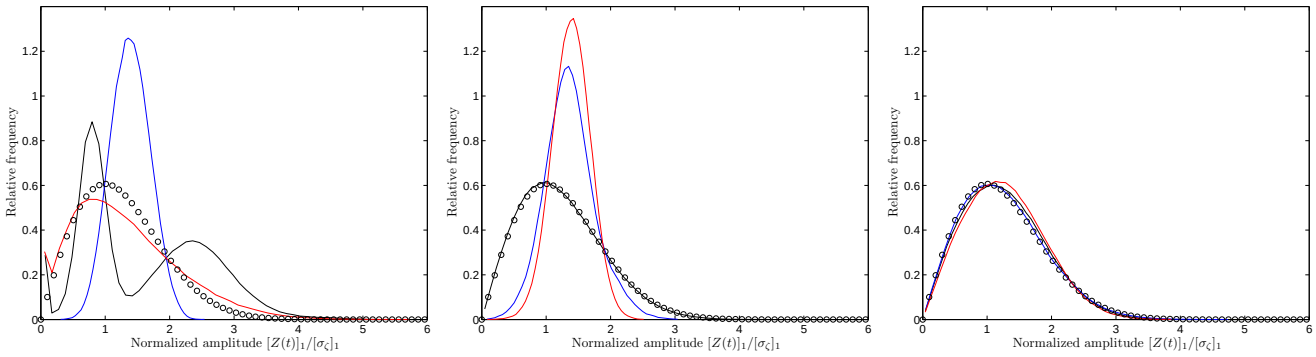

(a) $\mathcal{M} \approx 0.40$ (b) $\mathcal{M} \approx 0.51$ (c) $\mathcal{M} \approx 0.60$

Figure 43: Probability distribution function of the magnitude of $[\zeta(t)]_1$ as a function of Mach number for the steel blade. – $\alpha_0 = 0.8^o$, – $\alpha_0 = 5.2^o$, –$\alpha_0 = 10.1^o$.

An increase in the Mach number to 0.5 changed the observed pdfs. Note that at high angles of attack, the pdfs were similar to those observed for the Aluminum blade at the same flow conditions. Thus, it can be concluded that the time-varying blade vibration at these flow conditions were similar between blades of varying stiffness. In contrast, at $\alpha_0 = 0.8^o$, the pdf is very similar to a Rayleigh distribution. An increase in the Mach number to 0.6 resulted in pdfs which were similar to those observed for the Aluminum blade. This suggests that the aerodynamic mechanism responsible for the observed structural vibration at this flow condition had a similar effect regardless of blade stiffness.

The response of the blade in the second mode of vibration was also investigated. Figure 41 presents the dependence of the mean-squared amplitude of the blade as a function of Mach number and reduced frequency, while figures 44 and 45 present a brief segment of the time-series response of the Aluminum and Steel blades respectively. The time-series response was normalized by $[\sigma_\zeta]_2$.

The response of the Aluminum blade at $\alpha_0 = 0.8^o$ showed little change in mean-squared amplitude as the Mach number was increased. The time-series indicated that the vibration in this mode was very intermittent. The intermittency increased with Mach number, consistent with the observations of the blade response in the first mode. The response of the blade at the highest Mach number investigated was characterized by many short bursts of structural vibration.

Increasing the zero-flow angle of attack to $\alpha_0 = 5.2^o$ resulted in a decrease in vibration amplitude by an order of magnitude. This decrease was observed over all the Mach numbers investigated and was nearly uniform. Recall that for the first mode, the change in α_0 resulted in a uniform increase in the amplitude of vibration, by a factor of 6. The time-series response indicated that the vibration was very intermittent. It should be noted that the lowest vibration amplitudes at a given Mach number were observed at this angle. This is in contrast to the first mode, where the response was the highest at $\alpha_0 = 5.2^o$.

A further increase in the zero-flow angle of attack to 10.1^o resulted in a significant change in $\left[\boldsymbol{\sigma}_{\boldsymbol{\zeta}}^{\mathbf{2}}\right]_2$ as a function of Mach number and reduced frequency. The increase in $\left[\boldsymbol{\sigma}_{\boldsymbol{\zeta}}^{\mathbf{2}}\right]_2$ with Mach number and reduced frequency appeared to follow a power law with respect to Mach number. The time-series response of the blade shows that at a Mach number of 0.44, there was a quasi-periodic low-frequency ($\omega^\star_{\mathrm{AM}} \approx 0.023$) amplitude modulation of the second mode response. An increase in Mach number resulted in an increase in the frequency of the amplitude modulation. At a Mach number of 0.6, the time-series response appears to have two distinct amplitude modulations. The first is a high-frequency, low

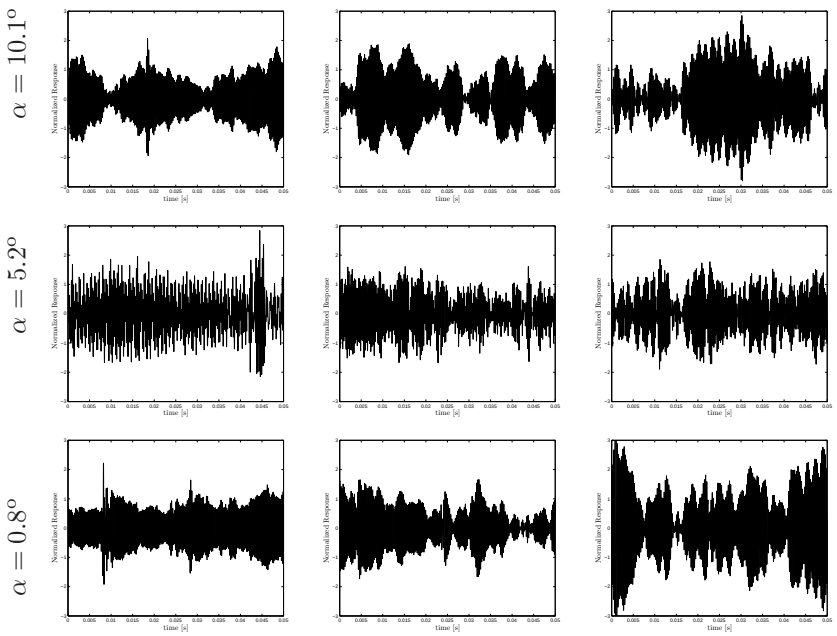

$\mathcal{M} \approx 0.44$ $\mathcal{M} \approx 0.54$ $\mathcal{M} \approx 0.6$

$\omega^\star \approx 2.02$ $\omega^\star \approx 1.64$ $\omega^\star \approx 1.48$

Figure 44: Steady response of the Aluminum blade in the second mode to a uniform jet as a function of Mach number and angle of attack.

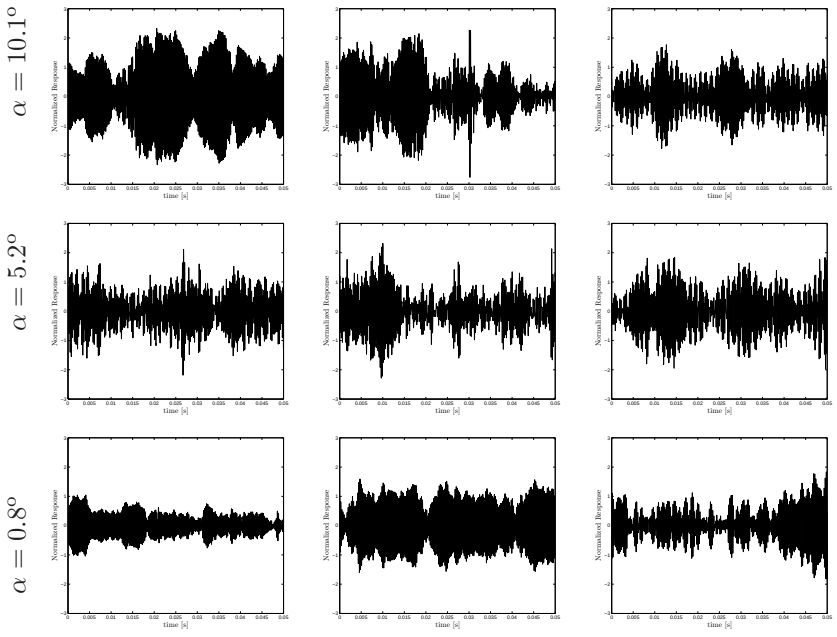

$\mathcal{M} \approx 0.44$ $\mathcal{M} \approx 0.54$ $\mathcal{M} \approx 0.6$

$\omega^\star \approx 2.16$ $\omega^\star \approx 1.76$ $\omega^\star \approx 1.58$

Figure 45: Steady response of the Steel blade in the second mode to a uniform jet as a function of Mach number and angle of attack.

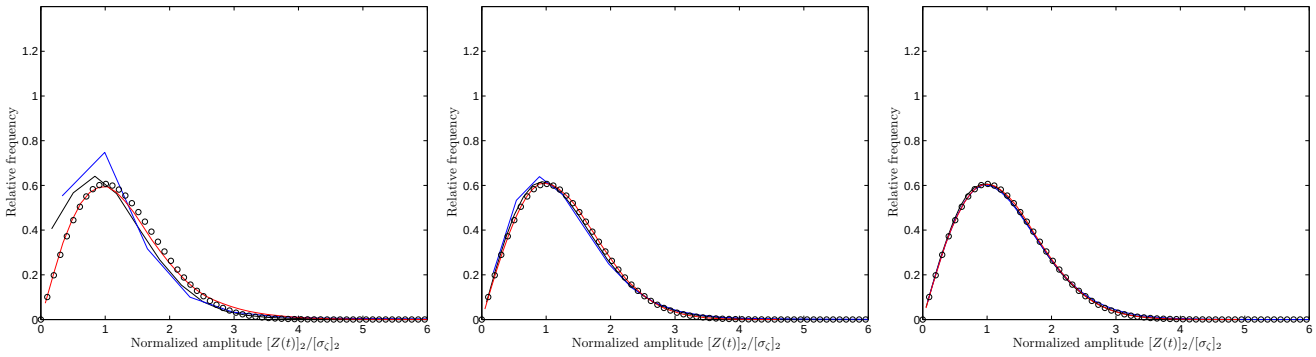

(a) $\mathcal{M} \approx 0.40$ (b) $\mathcal{M} \approx 0.51$ (c) $\mathcal{M} \approx 0.60$

Figure 46: Probability distribution function of the magnitude of $[\zeta(t)]_2$ as a function of Mach number for the Aluminum blade. – $\alpha_0 = 0.8^o$, – $\alpha_0 = 5.2^o$, –$\alpha_0 = 10.1^o$.

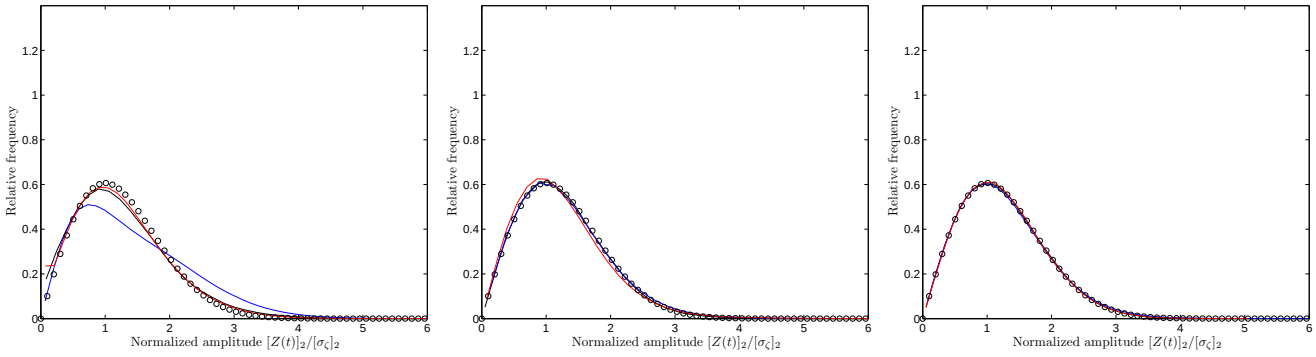

(a) $\mathcal{M} \approx 0.40$ (b) $\mathcal{M} \approx 0.51$ (c) $\mathcal{M} \approx 0.60$

Figure 47: Probability distribution function of the magnitude of $[\zeta(t)]_2$ as a function of Mach number for the steel blade. – $\alpha_0 = 0.8^o$, – $\alpha_0 = 5.2^o$, –$\alpha_0 = 10.1^o$.

amplitude type while the second is a low-frequency, high amplitude type. Both appeared to be quasi-periodic. It should be noted that the vibration amplitude self-limiting behavior due to zero-flow angle of attack was not observed for the second mode. This may be due, in part, to the small amplitude of the vibrations compared to those observed in the first mode response.

The effect of blade stiffness on $\left[\boldsymbol{\sigma}_{\boldsymbol{\zeta}}^{\mathbf{2}}\right]_2$ (figure 41 (b)) can be summarized as follows. There was a reduction in $\left[\boldsymbol{\sigma}_{\boldsymbol{\zeta}}^{\mathbf{2}}\right]_2$ at all α_0 and $\mathcal{M}$ tested. In addition, the dependence of $\left[\boldsymbol{\sigma}_{\boldsymbol{\zeta}}^{\mathbf{2}}\right]_2$ with respect to α_0 and Mach number were effected. Specifically, an increase in stiffness resulted in an increased dependency on Mach number and reduced frequency for $\alpha_0 = 0.8^o$ and 5.2^o. All three angles tested showed an increase in $\left[\boldsymbol{\sigma}_{\boldsymbol{\zeta}}^{\mathbf{2}}\right]_2$ when the Mach number was increased and the reduced frequency decreased. Finally, it should be noted that at the two highest α_0 investigated, the response was characterized by an amplitude modulation at $\mathcal{M} \approx 0.6$. The frequency was $\omega^\star_{\text{AM}} \approx 0.038$ for both $\alpha = 5.2^o$ and 10.1^o.

The pdfs of $[Z(t)]_2$ for the aluminum and steel blades can be found in figures 46 and 47 respectively. It is remarkable to note that the pdfs for both aluminum and steel are similar to a Rayleigh distribution , regardless of the Mach number or angle of attack. This suggests that the response for the second mode was essentially random.

The effect of an end-wall was investigated using the Aluminum blade at $\alpha_0 \approx 5^o$. The nominal tip gap was

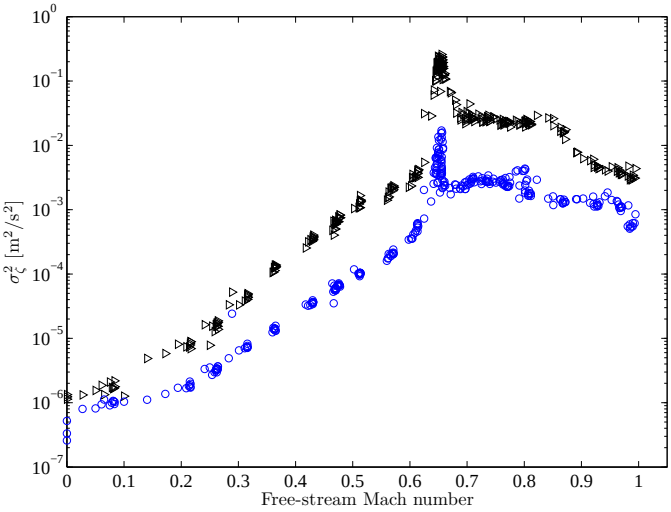

Figure 48: Mean-squared modal amplitude of the first three modes as a function of Mach number. ▷ mode 1; ○ mode 2.

approximately 0.4mm, which was about 2% of the blade chord. Figure 48 shows the variation in mean-squared modal amplitude as a function of Mach number for the first two modes. The following features should be noted. First, there was a peak in the response for both modes which occurred at $\mathcal{M} \approx 0.65$. This peak was very wide for the first mode and narrow for the second mode. The response of the blade in both modes appeared to increase linearly with Mach number until $\mathcal{M} \approx 0.6$. The response for both modes was very nearly constant in the range $0.7 \leq \mathcal{M} \leq 0.8$. At speeds greater than $\mathcal{M} = 0.85$, the response for the first mode decreased. The response for the second mode in this speed range showed a small decrease in magnitude.

A comparison between the response with and without an end-wall (cf. figures **??** and **??**) revealed the following. The trend observed with respect to the first mode had been significantly altered. Recall that the modal amplitude without an end-wall had a mean-squared modal amplitude which decreased from approximately 0.3 m^2/s^2 at $\mathcal{M} \approx 0.4$ to approximately 0.03 m^2/s^2 at $\mathcal{M} \approx 0.6$. The presence of an end-wall decreased the magnitude of the response for this range of Mach numbers by more than an order of magnitude. Furthermore, the mean-squared modal amplitudes showed an increase when the Mach number was increased, which was opposite of the trend observed without an end-wall.

The response for the second mode when an end-wall was present also showed significant differences from the response without an end-wall. It can be observed that the mean-squared modal amplitude increased with Mach number, and the overall magnitude was increased. This increase ranged from about 10 (at $\mathcal{M} \approx 0.4$) to nearly 100 (at $\mathcal{M} \approx 0.6$), suggesting that the Mach number had a stronger effect on the vibration amplitude when an end-wall was present.

An analysis of the flow about the blade was performed. PIV data were acquired at 84% span using the Aluminum blade without an end-wall. Three Mach numbers were investigated at $\alpha_0 = 0.5^o$. Figure 49 presents a snapshot the flow field for the three Mach numbers investigated. Isocontours represent the magnitude of fluid velocity normalized by the free-stream velocity. The free-stream velocity was subtracted from the vectors. Finally, the blade velocity distribution along the camber-line is included. These data were derived from the LDV measurements which were acquired simultaneously with the PIV data.

The location of the blade surface within the camera's field of view was determined in the following manner. A threshold was applied to the first frame of the image pair which set to zero any pixels whose intensity was less that 100

counts. The result was then eroded and then dilated using a disc structuring element with a diameter of 3 pixels. The effect of the erosion and dilation operations was to remove all features which were smaller than the size of the structuring element. These operations effectively isolated the features which were due to the intersection of the laser light sheet with the blade surface. A "mask" was created which was a binary image of the blade cross-section. The intensity of the pixels used in the mask can be described as the Gaussian blur of the blade cross-section shown in figure 33(b). The two-dimensional cross-correlation between this mask and the camera image was calculated. The approximate location of the peak in the cross-correlation was taken as the estimate of the location of the centroid of the blade.

Upstream of the blade, the flow was essentially uniform. In addition, there was a smooth acceleration of the flow over the suction side of the blade. At the highest Mach number investigated, the flow over the suction side of the blade remained sub-sonic. Finally, it can be observed that there were significant velocity fluctuations in the upper right corner of the field of view. This was a region of poor illumination and as such the estimates of the fluid velocity were less accurate than in the vicinity of the blade.

Figure 50 presents the computed vorticity for each of the snapshots shown in figure 49. Note that the velocity vectors represent the true velocity. It should be noted that the vorticity upstream of the blade was small but spatially uniform. The regions of high vorticity correspond to the blade surface and the wake region. It can be observed that there were discrete distributions of high vorticity which can be found along the wake. These discrete distributions are thought to reflect the unsteady aerodynamic forces on the blade. Finally, it should be noted that a region of high turbulence was found on the pressure side of the blade. This region may be responsible in part for the observed vibration at low angles of attack.

The time-averaged velocity field at several Mach numbers is presented in figure 51. Note that the general velocity distribution over the field of view varied only slightly as the Mach number was increased. The following features should be noted. First, the flow decelerated at the leading edge and was re-accelerated over the suction side. The maximum velocity over the suction side was approximately 1.4 times greater than the free-stream velocity. It can be observed that for the Mach numbers investigated, the flow was shock-free at this span-wise location. A region of low-momentum fluid can be observed downstream of 50% chord along the pressure side of the blade. This region of low momentum flow extended to the wake of the blade. Note that the chord-wise extent of the region did not vary significantly when the Mach number was increased.

The time-averaged vorticity field at several Mach numbers is presented in figure 52. Positive vorticity (blue contours) was found only in the vicinity of the leading and trailing edges on the pressure side of the blade. The suction side of the blade and the mid-chord region on the pressure side were bounded by flow with negative vorticity (red contours). The spatial distribution of vorticity in the vicinity of the blade surface was similar for all Mach numbers investigated. These two observations suggest that the region of low momentum flow on the pressure side of the blade may have been due to flow separation. The time-averaged location of the separation point was at approximately 25% chord and did not move significantly when the Mach number was increased.

4.4.3 Aero-mechanical damping ratio

The exchange of energy between the fluid and the structure is ultimately what governs the dynamics of the aeroelastic system. An approach to characterize this energy exchange is to estimate the "equivalent linear damping ratio", which is

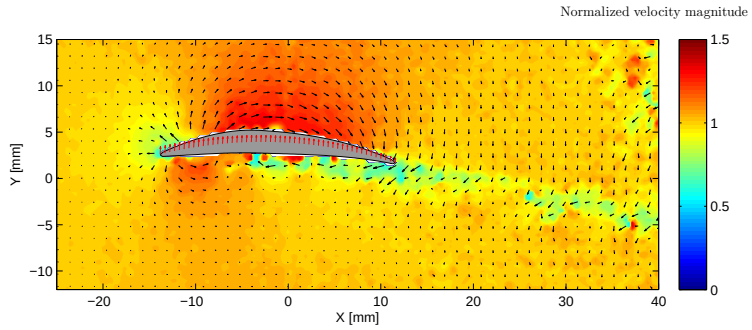

(a) $\mathcal{M} \approx 0.41$

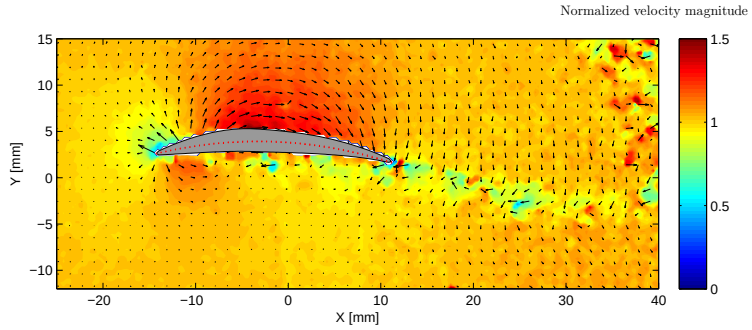

(b) $\mathcal{M} \approx 0.49$

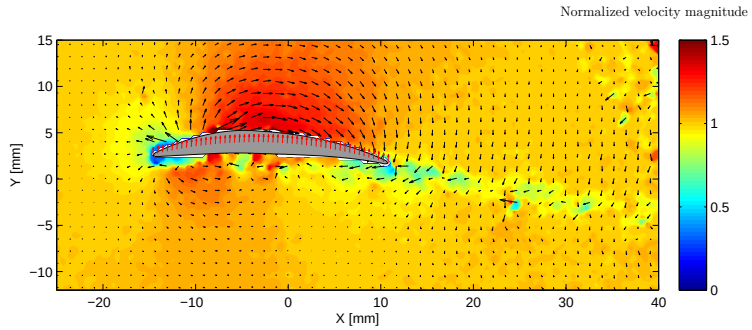

(c) $\mathcal{M} \approx 0.57$

Figure 49: Instantaneous flow field at 84% span for the Aluminum blade at $\alpha_0 = 0.5^{\circ}$ without an end-wall. $\rightarrow$ fluid velocity, $\rightarrow$ Blade velocity $\times 50$. Every 4^{th} vector is shown for clarity.

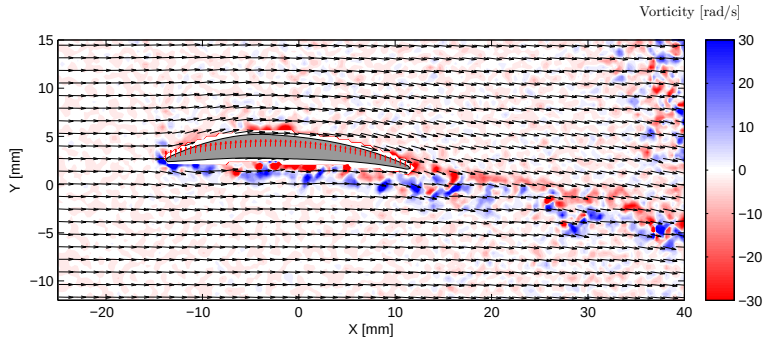

(a) $\mathcal{M} \approx 0.41$

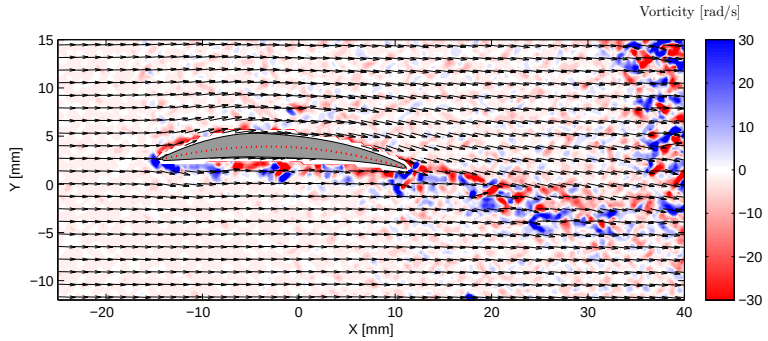

(b) $\mathcal{M} \approx 0.49$

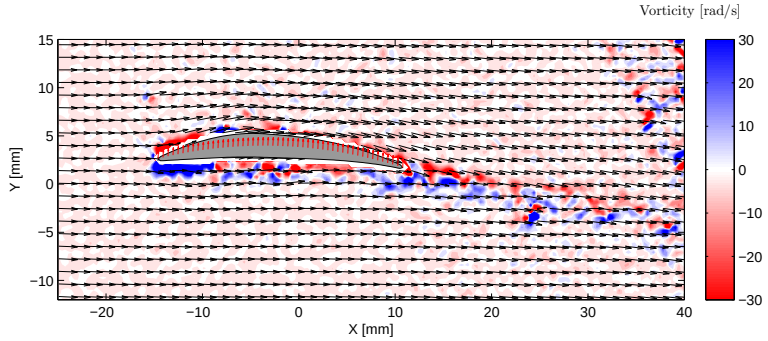

(c) $\mathcal{M} \approx 0.57$

Figure 50: Instantaneous flow field vorticity at 84% span for the Aluminum blade at $\alpha_0 = 0.5^{\circ}$ without an end-wall. $\rightarrow$ fluid velocity, $\rightarrow$ Blade velocity $\times 50$. Every 4^{th} vector is shown for clarity.

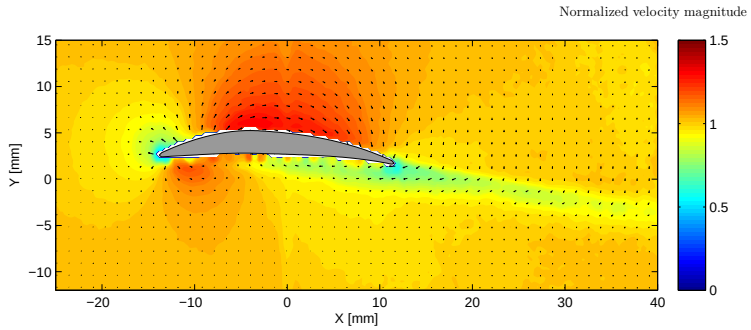

(a) $\mathcal{M} \approx 0.41$

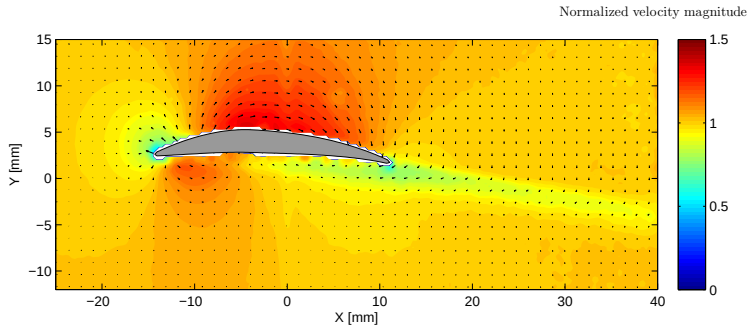

(b) $\mathcal{M} \approx 0.51$

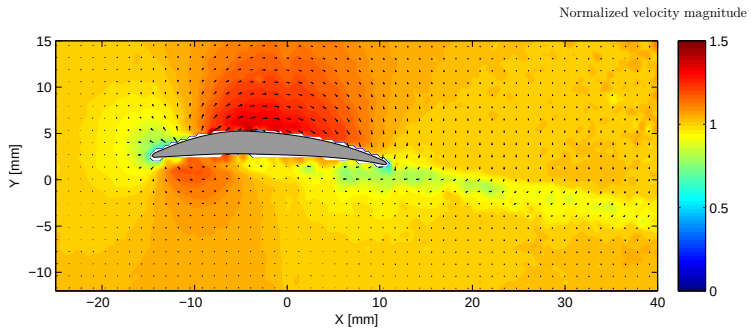

(c) $\mathcal{M} \approx 0.57$

Figure 51: Average flow field at 84% span for the Aluminum blade at $\alpha_0 = 0.5^{\circ}$ without an end-wall. Every 4^{th} vector is shown for clarity.

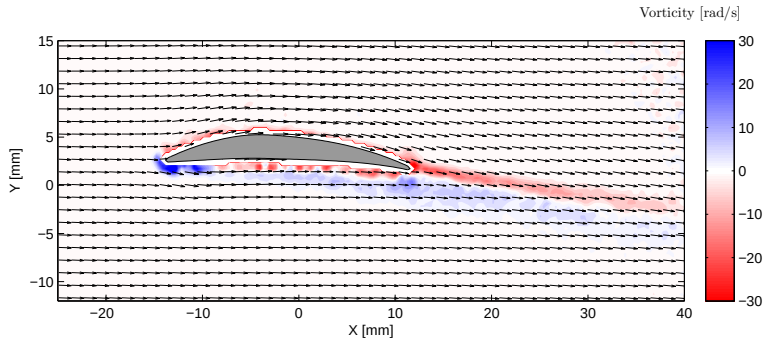

(a) $\mathcal{M} \approx 0.41$

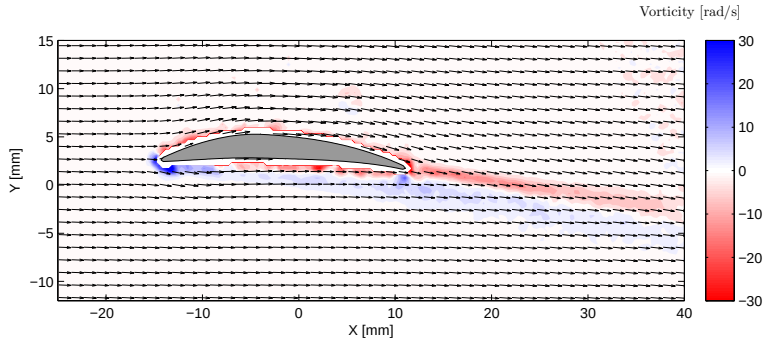

(b) $\mathcal{M} \approx 0.51$

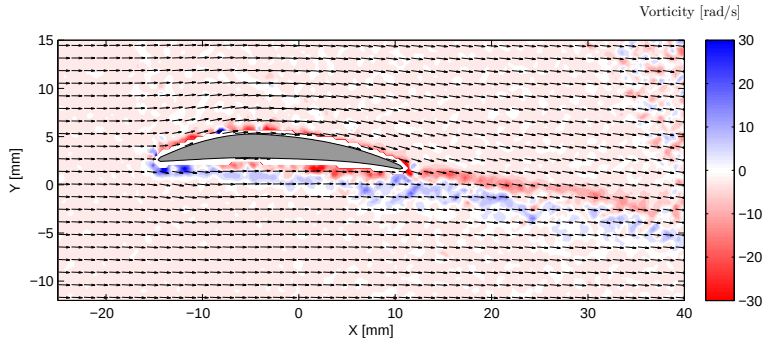

(c) $\mathcal{M} \approx 0.57$

Figure 52: Average flow field vorticity at 84% span for the Aluminum blade at $\alpha_0 = 0.5^{\circ}$ without an end-wall. Every 4^{th} vector is shown for clarity.

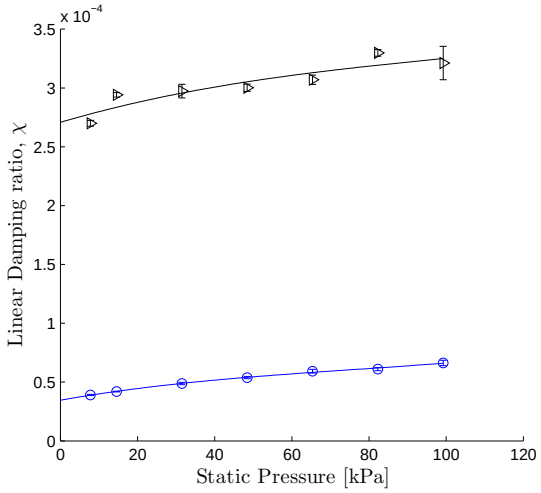

Figure 53: Equivalent linear damping ratio of the aluminum blade as a function of static pressure. ▷ - Mode 1, ○ - Mode 2.

described for a single degree of freedom mass-spring-damper system as

$$\chi = \frac{\varsigma}{2\sqrt{\kappa\mu}}. \tag{51}$$

ς represents the viscous damping, κ is the system stiffness and μ the system mass. χ expresses the rate at which a disturbance grows ($\chi < 0$) or decays ($\chi > 0$). Note that this approach implicitly assumes that the response of the system is linear. There are three primary contributions to χ. They are damping due to energy dissipation within the blade material (internal damping), damping associated with the parts to which the blade is mechanically attached (structural) and aerodynamic damping. The characterization of these three sources of damping will be addressed in this section.

The internal and structural damping ratio was estimated in the following manner. The response of the blade to an impulse load was filtered to isolate the mode of interest. A Hilbert transform (Bendat and Piersol (2000)) was performed. A linear curve fit was then applied to the logarithm of the magnitude of the transform. The slope of the curve fit yields the product $2\pi f\chi$. Thus, the damping ratio χ is obtained if the frequency of oscillation (f) is known.

The damping ratio of the aluminum blade in quiescent air was investigated. The blade was attached to a steel block whose mass was $O(10^2)$ greater than the blade itself. The steel block and impulsive loading mechanism were placed within a vacuum chamber. The structural response was measured using the single point LDV. Figure 53 displays the damping ratio for the first two modes as a function of static pressure. The effect of increasing static pressure yields a minor increase in the damping ratio. The increase is slightly larger in mode 1 than in mode 2. However, the damping ratio for both modes is extremely small. This result is consistent with the results of Kielb and Abhari (2003). A cubic polynomial was fit to the data to determine the internal damping of the structure. The internal damping was assumed to be the damping of the blade in a complete vacuum.

The contribution of the blade mount depicted in figure 31(b) to the equivalent damping ratio was also investigated. The damping ratio was estimated using both steel and aluminum blades at all three angles of attack investigated in the previous section. The results, averaged over all three angles, are presented in table 4. The internal damping of the

	χ	
Material/Source	Mode 1	Mode 2
6061-T6 AL, internal	$2.7 \times 10^{-4} \pm 2.5 \times 10^{-6}$	$3.9 \times 10^{-5} \pm 5 \times 10^{-7}$
6061-T6 AL, mount	$6.8 \times 10^{-3} \pm 2.9 \times 10^{-3}$	$6.8 \times 10^{-4} \pm 1.4 \times 10^{-4}$
A2 Tool Steel, mount	$8.8 \times 10^{-3} \pm 3.1 \times 10^{-3}$	$8.4 \times 10^{-4} \pm 3.4 \times 10^{-4}$

Table 4: Comparison of internal damping to structural damping for both blades investigated.

aluminum blade is presented for comparison. The mount increased the estimated damping by an order of magnitude for both modes. The damping was independent of blade material, which suggests that it was due to the assembly on which the blade is attached. The increase in the number of contact surfaces is thought to be responsible for the observed increase in χ. There were three major interfaces between the blade and the "ground"[‡] These were (cf. figure 31(b)) blade to rotatable mount, rotatable mount to test section wall and test section wall to ground. In contrast, the assembly used to produce the results shown in figure 53 consisted of one interface: blade to ground. The increase in the number of interfaces between the vibrating blade and "ground" and the corresponding increase in damping ratio implies that Coulomb damping (from friction between two sliding surfaces) increased substantially. It should be noted that the increase in damping due to the mount results in a mechanical system which was lightly damped.

The aerodynamic damping of the blade was estimated using the random-decrement technique. This technique can estimate the impulse response function of a single degree of freedom system subject to random excitation. The mathematical theory of the technique was described by Vandiver et al. (1982). The approach used in this study can be described as follows. The steady response of the blade was band-pass filtered to isolate each mode. The data were then split into segments 4 cycles of vibration long. The beginning of each segment had to have an amplitude greater than $2 \times [\sigma_\zeta]_p$ and a nearly zero slope. This ensured that the beginning of each segment corresponded to a peak in the vibratory amplitude. These segments were averaged together to obtain the "Random decrement signature". Using the assumptions of stationarity, this signature provides an estimate of the impulse response function. The damping ratio was estimated from this impulse response function using the Hilbert analysis described previously. The structural damping was subtracted to yield the damping due to unsteady aerodynamic forces. This can be considered to represent the damping which would be observed for small perturbations (such as a gust advecting over the blade) to the steady aeroelastic system.

An example of a "Random decrement signature" is presented in figure 54 for the aluminum blade without an end-wall at two different Mach numbers. It can be seen that the signature for each mode is time-resolved and can be approximated by a decaying sinusoid. Visual inspection of the signatures revealed that the damping ratio is small but non-zero. An increase from $\mathcal{M} \approx 0.4$ to 0.6 increased the damping ratio for the first mode, but decreased the damping ratio for the second.

The damping ratio of the blade without an end-wall as a function of angle of attack and Mach number can be seen in figure 55 for the first mode. There are several features which should be noted. First, at $\mathcal{M} < 0.45$, the aerodynamic damping was negative for all α_0 investigated. The stability of the system was maintained by the structural damping.

[‡]Here, ground is used to indicate an object whose mass was sufficiently large such that any vibration transmitted to it from the blade induces negligible motion.

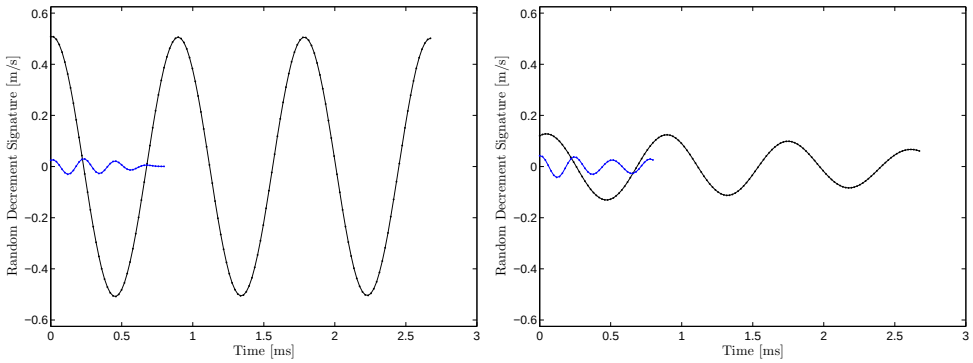

(a) $\mathcal{M} \approx 0.42$ (b) $\mathcal{M} \approx 0.60$

Figure 54: "Random decrement signature" for the Aluminum blade at $\alpha_0 = 5.2^o$ for two Mach numbers and without an end-wall. $-\bullet-$ Mode 1; $-\bullet-$ Mode 2.

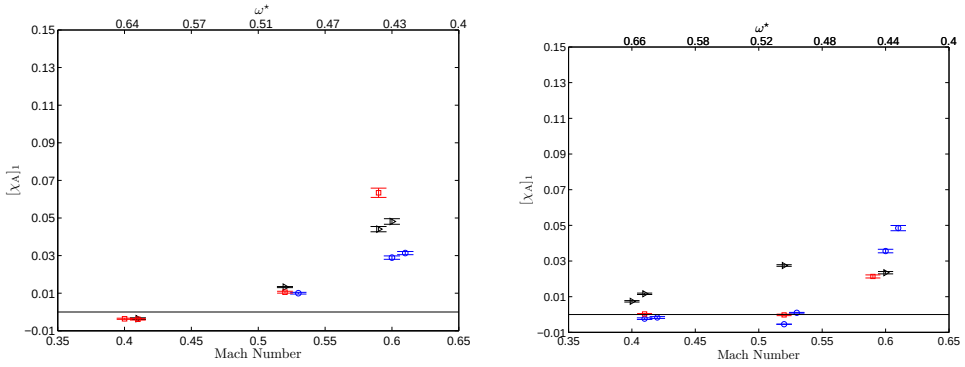

(a) Aluminum blade (b) Steel blade

Figure 55: Estimated total damping ratio for the first mode of vibration of the blade in a uniform jet without an end-wall. $\triangleright$ – $\alpha_0 = 0.8^o$, $\circ$ – $\alpha_0 = 5.2^o$, $\square$ – $\alpha_0 = 10.1^0$

It should be noted, however, that the aerodynamic damping was of a similar magnitude as the internal damping of the Aluminum blade. It can be concluded that for this blade at these flow conditions, the fluid was a source of excitation. The observed damping below $\mathcal{M} \approx 0.55$ did not vary much when the angle of attack was varied, but was sensitive to the Mach number. The angle of attack produced significant changes in the observed damping when the flow speed was greater than $\mathcal{M} \approx 0.55$. A decrease in damping ratio was observed at $\mathcal{M} \approx 0.6$ when the angle of attack was increased from $\alpha_0 = 0.8^o$ to 5.2^o. However, a further increase to $\alpha_0 = 10.1^o$ increased the damping ratio by a factor of 2. Recall that the mean-squared modal amplitude increased as the angle of attack was increased at this flow condition. A decrease in the damping can result in an increase in the magnitude of the response. However, the increase in damping along with the increase in modal amplitude which was observed as α_0 was increased to 10.1^o suggest that a significant change in the aeroelastic interactions occurred.

The effect of increasing the blade stiffness produced noticeable changes in the damping ratio. The damping ratio for the steel blade increased when the Mach number was increased, but the overall trend was different from that observed for the Aluminum blade. Note that for $\alpha_0 \geq 5.2^o$ and $\mathcal{M} \leq 0.55$, the aerodynamic damping was negative. However, structural damping was sufficient to ensure that the system was stable. The increase in damping with Mach number

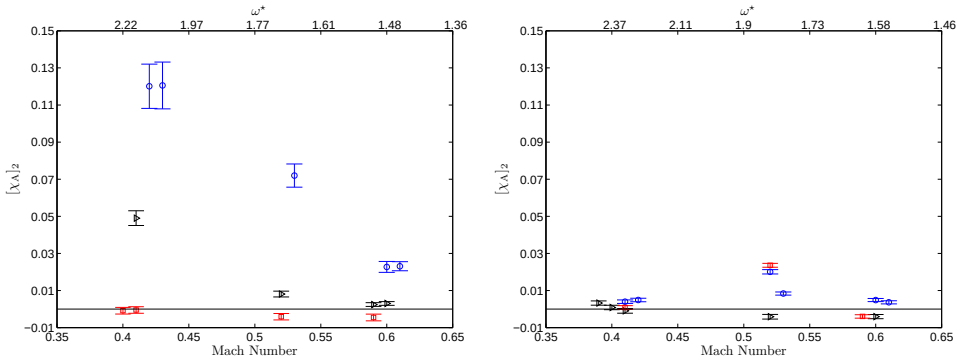

(a) Aluminum blade

(b) Steel blade

Figure 56: Estimated total damping ratio for the second mode of vibration of the blade in a uniform jet without an end-wall. ▷ – $\alpha_0 = 0.8^o$, ○ – $\alpha_0 = 5.2^o$, □ – $\alpha_0 = 10.1^0$

when the blade was at $\alpha_0 = 10.1^o$ was qualitatively similar to that observed for the Aluminum blade, but smaller in magnitude. A similar trend was observed for $\alpha_0 = 5.2^o$, but the effects of increased stiffness were not as pronounced. The largest change in damping ratio occurred for $\alpha_0 = 0.8^o$. An increase in blade stiffness resulted in positive estimates of $[\chi_A]_1$ over all Mach numbers investigated. The variation of $[\chi_A]_1$ with Mach number at this angle of attack was altered with an increase in blade stiffness. It can be observed that the aerodynamic damping decreased slightly when the Mach number was increased from $\mathcal{M} \approx 0.53$ to 0.6. The overall effect of an increase in blade stiffness was to reduce the dependence of $[\chi_A]_1$ on the Mach number.

The aerodynamic damping for the second mode can be seen in figure 56. The Mach number and angle of attack had a large influence on the damping for the aluminum blade. A decrease in damping was observed for $\alpha_0 = 0.8^o$ when the Mach number was increased. Note that at $\mathcal{M} \approx 0.6$, the aerodynamic damping is nearly zero. An increase in α_0 to 5.2^o increased the aerodynamic damping at all Mach numbers investigated. However, there was a larger reduction in the aerodynamic damping as the Mach number was increased. A further increase in α_0 resulted in negative aerodynamic damping for all Mach numbers observed. The damping decreased with Mach number, however the magnitude of this decrease was small.

An increase in the blade stiffness resulted in significant changes in the aerodynamic damping. Specifically, the effects of α_0 and $\mathcal{M}$ were greatly reduced. In addition, $[\chi_A]_2$ was much smaller for $\alpha_0 \leq 5.2^o$. It can be observed that at $\alpha_0 = 0.8^o$, the damping was nearly zero at $\mathcal{M} \approx 0.4$ and became negative as the Mach number was increased. An increase in α_0 to 5.2^o resulted in an increase in $[\chi_A]_2$ over all Mach numbers investigated. A peak was observed at $\mathcal{M} \approx 0.53$. The size of this peak increased when the angle of attack was increased to 10.1^o. However, $[\chi_A]_2$ was reduced at this angle of attack when $\mathcal{M} \approx 0.4$ and 0.6.

The effect of an end-wall on the estimated aerodynamic damping was investigated using the Aluminum blade at $\alpha_0 = 5^o$. The variation of $[\chi_A]_p$ as a function of Mach number can be seen in figure 57. Note that no damping ratio estimates were reported in the vicinity of the observed aeroelastic resonance, because the forcing could no longer be considered broad-band. This violated a key assumption of the Random Decrement technique, and results in erroneous damping ratio estimates.

It can be observed that the aerodynamic damping was negative for the first two modes at Mach numbers below

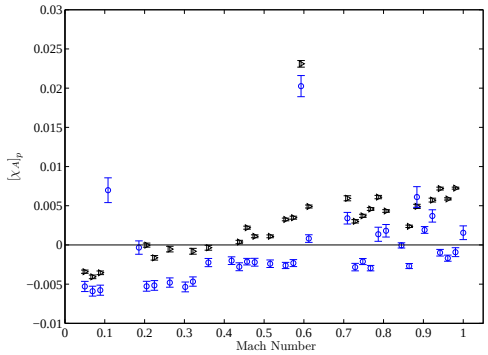

Figure 57: Estimated linear damping ratio for the aluminum blade as a function of Mach number. Note that the end-wall was present and $\alpha_0 = 5^o$. $\triangleright$ $[\chi_A]_1$; $\circ$ $[\chi_A]_2$.

approximately 0.45. The total damping was positive due to the large structural damping. The increase in $[\chi_A]_1$ was nearly linear with respect to Mach number up to $\mathcal{M} \approx 0.6$. In contrast, at Mach between 0.7 and 1.0, $[\chi_A]_1$ oscillated. Local maxima in the oscillation occurred at $\mathcal{M} \approx 0.8$ and 0.95, whereas local minima could be observed for $\mathcal{M} \approx 0.72$ and 0.87. The origin of the spike in AD_1 at $\mathcal{M} \approx 0.6$ is currently unknown. However, it is interesting to note that the magnitude is similar to the aerodynamic damping estimated for the Aluminum blade without an end-wall at similar α_0 and $\mathcal{M}$.

The dependence of $[\chi_A]_2$ on the Mach number differed from the trends observed for $[\chi_A]_1$. The magnitude of $[\chi_A]_2$ in the interval $0.1 \leq \mathcal{M} \leq 0.3$ was nearly constant except for a spike at $0.1 \leq \mathcal{M} \leq 0.2$. With the exception of the spike $[\chi_A]_2 < 0$ over this range. A sudden increase in the magnitude of the damping was observed at $\mathcal{M} \approx 0.35$, followed by another plateau in the magnitude of $[\chi_A]_2$. A spike was observed at $\mathcal{M} \approx 0.6$, which suggests that the increase in estimated damping for both modes was similar. Finally, it should be noted that the aerodynamic damping at $\mathcal{M} > 0.7$ oscillated. The local maxima and minima occurred at similar Mach numbers as those observed for $[\chi_A]_1$. Note however that there was a significant decrease in $[\chi_A]_2$ at $\mathcal{M} > 0.95$.

A comparison with the mean-squared modal amplitude 48 suggests the following. The increase in the modal amplitudes observed at low Mach numbers were due to an increase in the aerodynamic forcing. Note that within this range, all of the energy was dissipated by mechanical friction associated with the blade mount. There was a slight decrease in the slope of $\left[\boldsymbol{\sigma}_{\boldsymbol{\zeta}}^{\mathbf{2}}\right]_1$ at $\mathcal{M} \approx 0.5$, which coincided with positive aerodynamic damping. No such change in slope was observed for the second mode, presumably due to the negative aerodynamic damping at these flow speeds. The fluctuations in $[\chi_A]_1$ and constant $\left[\boldsymbol{\sigma}_{\boldsymbol{\zeta}}^{\mathbf{2}}\right]_1$ over $0.7 \leq \mathcal{M} \leq 0.9$ suggest that there were significant fluctuations in the aerodynamic excitation over this range of flow speeds. The decrease in $\left[\boldsymbol{\sigma}_{\boldsymbol{\zeta}}^{\mathbf{2}}\right]_1$ at Mach numbers larger than 0.85 correlated very well with the observed increase in $[\chi_A]_1$ over the same range. In contrast, the response and aerodynamic damping for the second mode over this range were not strongly correlated. It should be noted that the total damping over this range was between 0.005 and 0.015, which suggests that the structural damping may have been important in determining $\left[\boldsymbol{\sigma}_{\boldsymbol{\zeta}}^{\mathbf{2}}\right]_2$ at this set of flow conditions.

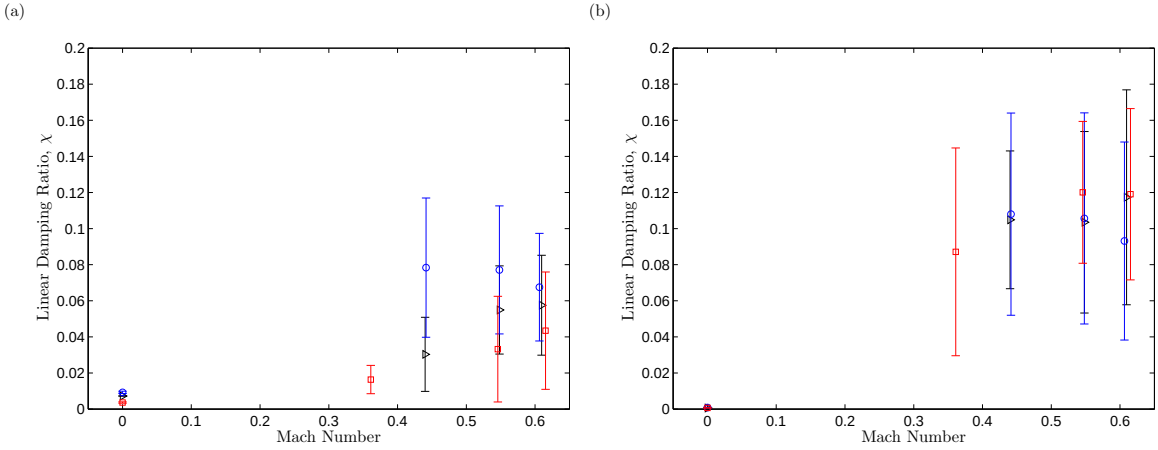

Figure 58: Estimated linear damping ratio of the first two modes vibration for the Aluminum blade in a uniform jet as a function of Mach number and zero flow angle of attack. $\triangleright$ – $\alpha_0 = 0.8^o$, $\circ$ – $\alpha_0 = 5.2^o$, $\square$ – $\alpha_0 = 10.1^0$. (a) Mode 1. (b) Mode 2.

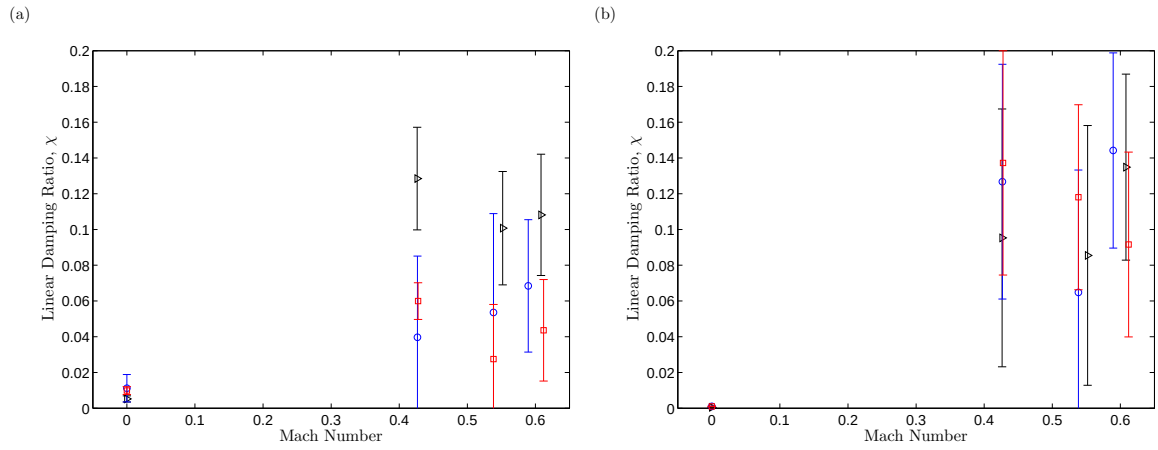

Figure 59: Estimated linear damping ratio of the first two modes vibration for the Steel blade in a uniform jet as a function of Mach number and zero flow angle of attack. $\triangleright$ – $\alpha_0 = 0.8^o$, $\circ$ – $\alpha_0 = 5.2^o$, $\square$ – $\alpha_0 = 10.1^0$. (a) Mode 1. (b) Mode 2.

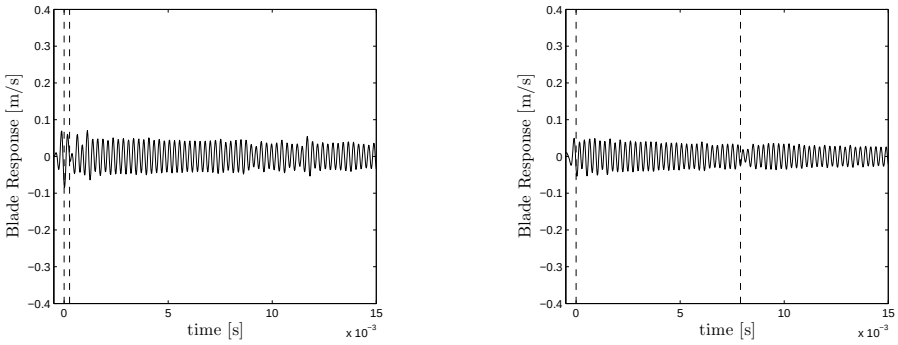

Figure 60: Two examples of an abrupt, transient reduction in impulse response amplitude for the Steel blade at $\alpha_0 = 0.8^o$ and $\mathcal{M} \approx 0.44$.

4.4.4 Response to a mechanical impulse

The structural response of an aeroelastic system can yield insight regarding the stability of the steady response to disturbances. The aeroelastic mechanisms which drives the system back to a state of equilibrium also reveal paths by which energy is removed from the system for a given set of flow parameters. In certain circumstances, a second stable equilibria has been revealed when the system is disturbed Schewe et al. (2003). Therefore, it is valuable to consider the response of the aeroelastic system to a disturbance.

The system was disturbed by applying an impulsive load to the blade using the mechanism shown in figure 32. The response of the blades to this load as a function of Mach number, reduced frequency and zero-flow angle of attack was investigated. The response was characterized by the equivalent linear damping ratio. The damping ratio was estimated using the same approach which was used to characterize the structural and internal damping. However, the impulse response function was truncated to include the response up to the point where the vibration amplitude had decayed to 1/2 the initial amplitude. This was done to differentiate between the vibration induced by the steady flow and the response due to the impulse. Figure 58 presents the estimated linear damping ratio for the Aluminum blade, while figure 59 presents the damping ratio for the Steel blade. Each data point represents the average from a 10 impulse response tests.

The data exhibit significant scatter. This is due, in part, to difficulties encountered in defining the extent of the structure's impulse response and the response due to aeroelastic excitation from the steady flow. In addition, it was found that the blade vibration amplitude would be briefly reduced nearly to zero at random points in the response. After such an event occurred, the blade would become re-excited and continue in a manner consistent with the original impulse-response. An example of this behavior is shown in figure 60 for the second mode response of the steel blade at $\alpha_0 = 0.8^o$ and $\mathcal{M} \approx 0.44$. The blade appeared to follow the same trajectory with respect to the envelope of decay after the amplitude was suddenly reduced. The duration of this reduction was usually a few cycles occurred at random points in the response.

The following trends can be observed. The presence of fluid moving over the blade resulted in a significant increase in the damping ratio, $[\chi_I]$, for both modes. Presumably, this is due to the transfer of structural vibration energy into vortical disturbances in the fluid. There are few statistically significant changes in the damping ratio due to either α_0 or M for the first mode response of the Aluminum blade. However, the highest observed value of $[\chi_I]_1$ at a given Mach

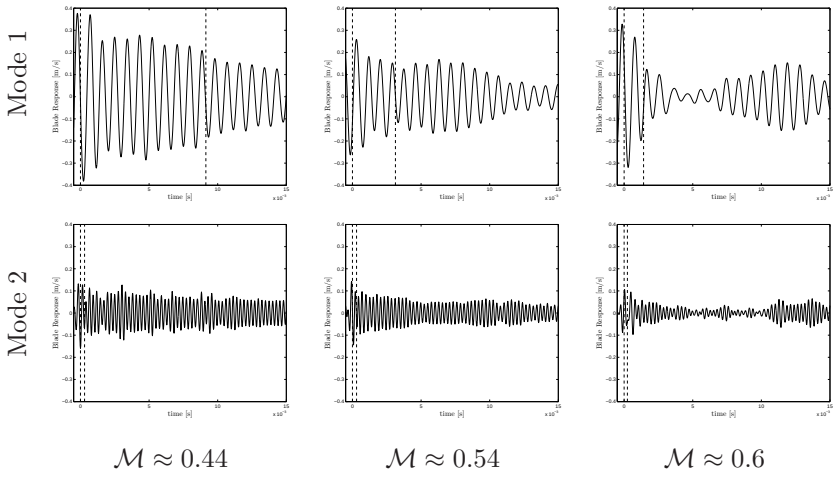

Figure 61: Aluminum impulse response for $\alpha = 0.8^o$

number consistently occurred at $\alpha_0 = 5.2^o$. An increase in blade stiffness resulted in an increase in χ for the first mode response at $\alpha_0 = 0.8^o$ and $\mathcal{M} \approx 0.44$. Furthermore, the damping ratio at this angle was consistently higher than at $\alpha_0 = 10.1^o$ and appeared to have a similar dependence with respect to Mach number. The damping ratio for the second mode response showed little dependence on either Mach number, α_0 or blade stiffness.

The time-dependent impulse response of the blades, filtered to isolate the modes of interest, are presented in figures 61 - 63. Three cases were selected which best elucidate the dynamic response of the blade subject to a mechanical impulse and flow excitation. It should be noted that the impulse response functions for α_0 not presented here display qualitatively similar behavior.

The response of the Aluminum blade to an impulse as a function of Mach number for $\alpha_0 = 0.8^o$ is presented in figure 61. The damping was positive for all combinations of α_0 and $\mathcal{M}$, indicating a stable aeroelastic system. The blade exhibited an increase in damping for the first mode response as the Mach number was increased. The blade never stopped vibrating during the response. It was observed that at low Mach numbers and low α_0, the blade impulse response would decay to the original steady amplitude. This was observed for conditions where the intermittency of the steady vibration was low. However, at higher Mach number and α_0 the blade vibration would decay to an amplitude significantly lower than the steady value. Once it had reached this point, the flow would re-excite the structure up to the steady vibration amplitude. This is shown for $\alpha_0 = 0.8^o$ and $\mathcal{M} \approx 0.54$ and 0.6 for the first mode. This type of response was also observed for the second mode.

The impulse response functions for the Aluminum blade at $\alpha_0 = 10.1^o$ are shown in figure 62. The dependence of $[\chi_I]_1$ on Mach number and reduced frequency was not a strong as was observed for $\alpha_0 = 0.8^o$. The response for the second mode was qualitatively similar between the two α_0. In addition, the decay of the response for the first mode at high Mach number showed a similar under-shoot and re-excitation as was observed at $\alpha_0 = 0.8^o$. This suggest that the mechanism which causes this response is weakly dependent on α_0.

The effect of increased blade stiffness at $\alpha_0 = 0.8^o$ on the impulse response is shown in figure 63. The damping in the first mode response showed a noticeable increase. In addition, it was found that $[\chi_I]_1$ was weakly dependent on Mach number. The impulse response in the second mode was qualitatively similar to the Aluminum blade at the same Mach number.

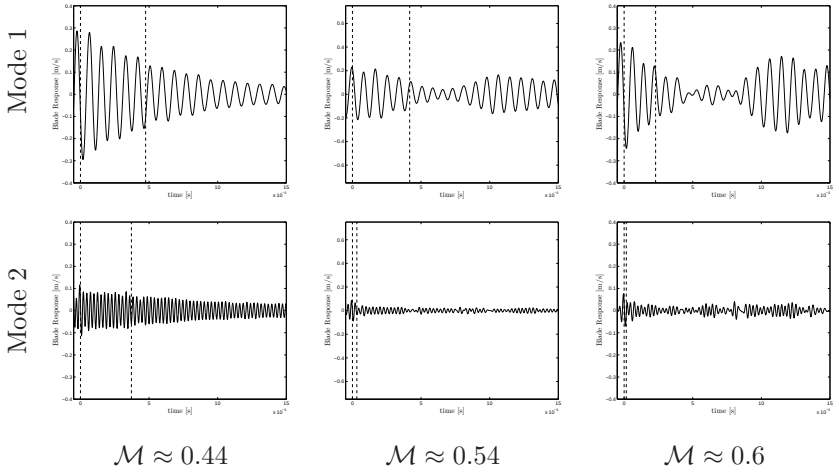

Figure 62: Aluminum impulse response for $\alpha = 10.1^{\text{o}}$

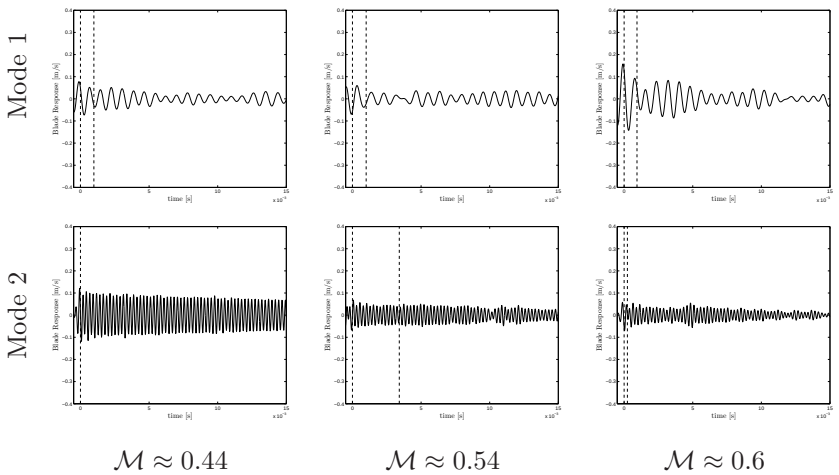

Figure 63: Steel impulse response for $\alpha = 0.75^{\text{o}}$

4.5 Summary

The dynamics of a cantilevered blade in a high Mach number flow were presented. The effect of Mach number, reduced frequency, angle of attack, blade stiffness and the presence of an end-wall were investigated. Three aspects of the system were considered: the steady response to a uniform flow, the aerodynamic damping associated with this steady flow and the transient response due to a mechanical impulse.

The steady response of the blade in the first mode to a uniform flow without an end-wall was found to have a strong dependence on all parameters investigated. Specifically, it was found that the dependence of $\boldsymbol{\zeta}$ on Mach number and reduced frequency was strongly dependent on the zero-flow angle of attack and blade stiffness. The response appeared to become independent of α_0 at angles above 5^o and Mach numbers above 0.54 for both blade materials investigated. In addition, the largest response at all Mach numbers investigated occurred when $\alpha_0 = 5.2^o$. These observations were consistent between blades of differing stiffness. There was a quasi-periodic amplitude modulation of the first mode response at these flow conditions. The frequency of this amplitude modulation increased with increasing Mach number and decreasing reduced frequency. These observations suggest that the structural excitation may be due to a region of separated flow whose location on the blade surface varies with time. It is thought that the frequency at which vorticity is shed from the separated flow is related to the frequency of the observed amplitude modulation. However, detailed fluid measurements are necessary to confirm this hypothesis.

The response in the second mode was also dependent upon both α_0, Mach number and reduced frequency. The mean-squared amplitude of the response showed a similar dependence on stiffness as was observed for the first mode response. However, the lowest response for a given Mach number was consistently found to be at $\alpha_0 = 5.2^o$. The time-dependent structural velocity was found to be highly intermittent for this mode.

An analysis of the flow field about the Aluminum blade at 84% span was performed using PIV. The blade angle of attack was fixed at $\alpha_0 = 0.5^o$ and no end-wall was present. The analysis revealed a region of flow separation which may have had a significant contribution to the observed blade response at low α_0.

The effect of an end-wall was investigated at a single angle of attack for the Aluminum blade. A large range of Mach numbers were investigated. It was discovered that the presence of an end-wall reduced the mean-squared modal amplitude by nearly an order of magnitude for the first two modes in the range of $0.4 \leq \mathcal{M} \leq 0.6$. An aeroelastic resonance was discovered at $\mathcal{M} \approx 0.65$. This resonance resulted in large amplitude excitation of both modes.

The damping of the blade was investigated. The magnitude of internal (material) damping and structural damping were quantified using an impulsive loading mechanism. The aerodynamic damping was estimated using the Random Decrement method for a range of Mach numbers, angles of attack, blade stiffness and for the presence of an end-wall. The aerodynamic damping in the first mode for the Aluminum blade showed a strong dependence on Mach number and relatively little dependence on angle of attack. An increase in blade stiffness reduced the aerodynamic damping for this mode. It was discovered that the aerodynamic damping for the second mode was strongly influenced by the Mach number and blade stiffness. The aerodynamic damping for the aluminum blade was reduced when the Mach number was increased for $\alpha_0 \leq 5.2^o$. An increase in blade stiffness resulted in a decrease in the aerodynamic damping and its dependence on Mach number.

The influence of an end-wall on the aerodynamic damping was also investigated. It was found that the end-wall reduced the aerodynamic damping. Furthermore, it was revealed that the aerodynamic damping for both modes was

slightly negative at $\mathcal{M} \leq 0.4$. Note that the structural damping was sufficient to ensure that the aeroelastic system was stable. The aerodynamic damping increased with Mach number for both modes, but at Mach numbers greater than 0.7 the increase oscillated with Mach number. The local maxima and minima of the aerodynamic damping in this Mach number range were comparable between both modes.

The response of the blade to an impulsive load was also investigated. It was found that the internal damping and structural damping of the blade mount was negligible compared to the damping ratio. An increase in blade stiffness increased the estimated linear damping ratio for the first mode only for $\alpha_0 = 0.8^{\text{o}}$.

The damping ratio due to an impulse of the system for all the combinations of α_0, blade stiffness, Mach number and reduced frequency which were investigated was positive. The damping in the first mode increased with Mach number. An increase in blade stiffness caused an increase in the damping ratio for the first mode at $\alpha_0 = 0.8^{\text{o}}$. It was found that at low Mach number and α_0 the blade vibration amplitude due to a mechanical impulse decayed back to the steady-state amplitude of vibration. At higher Mach number and α_0, this response decayed to an amplitude significantly lower than the steady-state value. After it had reached this point, the flow then re-excited the structure back to the steady-state vibration amplitude.

5 Conclusions and Future Work

The motivation for this research program was to improve the understanding of the aeroelastic phenomena which influence the dynamics of modern compressor blades. An understanding of these phenomena will lead to more accurate prediction of blade structural loads with improvements in compressor performance, durability and efficiency. A review of the specific research objectives and a summary of the findings will be presented. This will be followed by a discussion of future work.

5.1 Conclusions

The specific objectives of this research program were to develop novel measurement technology for the empirical characterization of the aeroelastic interactions typical of modern axial compressors and to apply these technologies to several canonical systems. The systems which were studied were designed to isolate the effects of various aspects common to modern axial compressors, such as compressibility, three-dimensional flow and annular cascade effects. The progress in meeting these objectives will be summarized briefly.

The novel measurement technology which was developed was termed Blade Image Velocimetry (BIV). This measurement technique utilized equipment common to PIV systems and is capable of measuring both fluid and structural velocity simultaneously. This capability is critical in the characterization of the non-linear aeroelastic system typical of modern axial compressors because of the coupled nature of the fluid and structure. Section 2 described the fundamental theory of the BIV technique and provided a practical demonstration of the simultaneous acquisition of fluid and structural velocity. The practical demonstration of combined PIV and BIV linked torsional oscillations of a flat plate at a large angle of attack to a moving separation point. A theory was proposed for the estimation of the amplitude of vibration of a cantilevered blade using observations of the tip velocity. An analysis of measurement error was presented in which two sources of error were considered. The first source of error was due to uncertainty in estimating the true blade velocity when using an image correlation based approach. The magnitude of this error was related to the sub-pixel accuracy of the correlation algorithms and the peak displacement of the blade between the two images and resulted in a positive bias error in the modal amplitude estimate. The second error was related to the estimation of a sinusoidally varying velocity using displacement measurements. This error was related to the time delay between the two images and the temporal frequency of oscillation of the tip velocity. The error resulted in a negative bias in the modal amplitude estimate. The theoretical error analysis was experimentally validated against Laser Doppler Vibrometer (LDV). Good agreement was obtained between the theory and the experimental error.

The BIV technique was applied to a high-speed axial compressor in section 3. The unique challenges associated with this application, such as uncertainty in estimating the magnitude of the noise and the validity of the assumptions used in the theoretical derivation of the measurement error were discussed. An estimate of the noise in the measurement system could be obtained from the statistics of the observed tip motion. This estimate helped to reduce the bias error associated with the sub-pixel accuracy of the correlation algorithms. The effects of noise which was spatially correlated to the tip motion of the blade and non-orthogonal (but linearly independent) tip modes were investigated. Both these effects resulted in significant positive bias errors in the modal amplitude estimates. The application of the BIV technique to a high-speed axial compressor detected low amplitude vibrations at 50% and 98% speed. In addition, the accuracy

of the technique was investigated by varying the time between two images, Δt. It was determined that the accuracy improved when the Δt was increased. The improved accuracy was related to the increase in blade displacement relative to the accuracy of the correlation algorithms. Good agreement in the time-averaged tip speed was obtained for blade tip displacements up to 300 pixels.

An investigation of the aeroelastic response of a canonical compressor blade in a uniform, high Mach number jet was presented in section 4. This investigation studied the effect of Mach number, angle of attack, blade stiffness and tip gap on the amplitude of blade vibration, the effective aerodynamic damping and the response of the system to a mechanical impulse. The response of the blade revealed a complex interdependence on all the parameters investigated. A summary of the general trends which were observed can be described as follows. The amplitude of the first eigen-mode of blade vibration (first flexure) due to steady flow without an end-wall (infinite tip gap) decreased as the Mach number was increased from 0.4 to 0.6 at moderate angles of attack for an Aluminum blade. A Steel blade (whose natural frequencies were comparable to the Aluminum blade) reduced the variation with Mach number and the overall magnitude of the response. The observed modal amplitude at $\alpha_0 = 10.1^o$ had a similar trend with Mach number for both blades. The amplitude of the second eigen-mode (first torsion) increased as the Mach number was increased from 0.4 to 0.6. The modal amplitude for the aluminum blade was sensitive to both Mach number and angle of attack, whereas the amplitude for the Steel blade showed little variation with angle of attack at $\alpha_0 \geq 5.2^o$. The presence of an end-wall with a tip gap equal to 2% of the blade chord resulted in a reduction in the amplitude of vibration for both modes at Mach numbers between 0.4 and 0.6 when the blade angle of attack was at 5^o.

The variation in aerodynamic damping with the parameters investigated can be described as follows. The damping for the first mode for an Aluminum blade increased with Mach number for all angles of attack investigated. There was little dependence on angle of attack at Mach numbers below $\mathcal{M} \approx 0.5$. The effect of increasing blade stiffness resulted in a reduction of the aerodynamic damping for the first mode at large angles of attack and high Mach numbers. The damping for the second mode of the Aluminum blade decreased with increasing Mach number at moderate angles of attack. The aerodynamic damping showed little variation with Mach number at large angles of attack. Similar behavior was observed at all angles of attack when the blade stiffness was increased. The effect of an end-wall decreased the aerodynamic damping for both modes over the range of Mach numbers investigated.

The response of the aeroelastic system to a mechanical impulse was characterized using an equivalent linear damping ratio. The damping ratio that was estimated was much larger than the aerodynamic damping ratio. This indicates that the mechanisms of energy exchange between the fluid and structure for an impulsive mechanical load differed from those associated with the steady flow. The effects of Mach number, angle of attack and blade stiffness could not be distinguished due to difficulties in estimating the extent of the impulse response. Specifically, the transition from the impulse response to the response due to steady flow could not be reliably determined using structural vibration measurements alone.

5.2 Future Work

Many of the topics which were addressed in this report are not fully understood. A brief review of some of the active and future areas of research will be presented.

5.2.1 Optimization of BIV

The suitability of the BIV technique in the estimation of axial-turbomachinery blade vibrations has been established. However, there are aspects of the measurement technique which require further study. One such area is the empirical validation of the estimated blade vibration on high-speed turbomachinery. The results presented in section 3, while encouraging, require validation using an independent estimate of the blade vibration. Comparison of the vibration amplitude estimates provided by BIV with the "true" blade vibration will provide insight into the issues which were raised in section 3. In addition, verification of the BIV error-analysis is necessary to establish the technique's reliability in the estimation of blade vibration. This is currently an active area of research at Hessert Laboratory.

Another aspect which requires further development is optimization of the BIV technique. The results presented in section 3 demonstrated that accurate velocity estimates could be obtained for large blade tip displacement. This observation along with the fact that the blade tip features are invariant suggest that similar accuracy can be obtained using a single-frame, double-exposure image recording approach. The use of a single-frame, double exposure recording approach allows for the use of a conventional CCD camera to be used in lieu of a high-performance PIV camera. This allows for an increase in spatial resolution which will increase measurement accuracy. The implementation and optimization of this recording approach in the context of axial tubomachinery blade vibration measurement will be a topic of future research.

5.2.2 Investigation of the non-linear aeroelasticity a canonical compressor blade

The response of a canonical compressor blade to a uniform flow presented in section 4 revealed a complex interdependence of the blade response upon the flow Mach number, blade angle of attack, blade stiffness, and presence of an end-wall. A thorough understanding of the interaction between the fluid and the structure is necessary to explain the variations in steady vibration amplitude, aerodynamic damping and aeroelastic response when a mechanical impulse is applied to the blade. Detailed measurements of both the unsteady flow field and the structural dynamics is an area of ongoing research. An understanding of the mechanisms of energy exchange for this canonical system may provide insight into interactions between the fluid and compressor blades at off-design conditions.

5.2.3 Investigation of adverse aeroelastic resonance on a modern axial compressor

The investigation of aeroelastic interactions present in high-speed compressors will be an area of future research. Provisions have been made for the design and construction of a new compressor facility. This facility will be capable of conducting fundamental research on high-speed, high pressure ratio axial compressors. The specific compressor for which this facility is being designed is a scale model of a single stage of a civil jet engine. A strong non-synchronous blade vibration was discovered. The investigation of the aeroelastic interactions which result in this vibration will be a major priority. Measurement techniques such as combined BIV/PIV will be utilized in this investigation.

References

Abdel-Rahim, A., Sisto, F., and Thangam, S. (1993). Computational study of stall flutter in linear cascades. *J. of Turbomachinery*, 115.

Akai, T. and Atassi, H. (1980). Aerodynamic and aeroelastic characteristics of oscillating loaded casscades at low mach number, part 2: Stability and flutter boundaries. *J. Engineering for Power*, 102.

Al-Bedoor, B. (2002). Blade vibration measurement in tubomachinery: current status. *Shock and vib. digest*, 34(6).

Alayli, Y., Topçu, S., Wang, D., Dib, R., and Chassagne, L. (2004). Applications of a high accuracy optical fiber displacement sensor to vibrometry and profilometry. *Sensors and Actuators A*, 116.

Atassi, H. and Akai, T. (1980). Aerodynamic and aeroelastic characteristics of oscillating loaded casscades at low mach number, part 1: Pressure distribution, forces and moments. *J. Engineering for Power*, 102.

Bell, J. and Rothberg, S. (2000). Laser vibrometers and contacting transducers, target rotation and six degree-of-freedom vibration : what do we really measure? *J. Sound and Vibration*, 237(2).

Belz, J. and Hennings, H. (2006). *Unsteady Aerodynamics, Aeroacoustics and Aeroelasticity of Turbomachines*, chapter Experimental flutter investigations of an annular compressor cascade: influence of reduced frequency on stability. Springer.

Bendat, J. and Piersol, A. (2000). *Random Data*. Wiley Interscience.

Bisplinghoff, R., Ashley, H., and Halfman, R. (1996). *Aeroelasticity*. Dover.

Bouhadji, A. and Braza, M. (2003). Organized modes and shock-vorteex interaction in unsteady viscous transonic flows around ana aerofoil part 1: Mach number effect. *Computers and Fluids*, 32.

Breuer, K., Bird, J., Han, G., and Westin, J. (2001). Infrared diagnostics for the measurement of fluid and solid motion in micromachined devices. In *2001 ASME Mechanical Engineering Congress and Exposition*, New York, NY. ASME.

Buffum, D., Capece, V., King, A., and EL-Aini, Y. (1996). Oscillating cascade aerodynamics at large mean incidence. Technical Memo 107247, NASA.

Burner, A., Liu, T., and DeLoach, R. Uncertainty of videogrammetric techniques used for aerodynamic testing. In *22nd Aerodynamic Measurement Technology and Ground Testing*. AIAA.

Cameron, J. (2007). *Stall inception in a high-speed axial compressor*. PhD thesis, The University of Notre Dame.

Cameron, J., Gendrich, C., Morris, S., and Corke, T. (2006). A transonic axial compressor facility for fundamental research and flow control development. In *44th AIAA Aerospace sciences meeting and exhibit*, Reno, NV. AIAA.

Carrington, I., Wright, J., Cooper, J., and Dimitriadis, G. (2001). A comparison of blade tip timing data analysis methods. *Proc. Instn. Mech. Engrs.*, 125G.

Chen, T., Vasanthakumar, P., and He, L. (2002). Analysis of unsteady blade row interaction using nonlinear harmonic approach. *J. Propulsion and Power*, 17(3).

Claveau, F., Fortier, P., Lord, S., and Gingras, D. (1996). Mechanical vibration analysis using an optical sensor. Canadian Conference on Electrical and Computer Engineering, IEEE.

Day, I. (1993). Stall inception in axial flow compressors. *J. Turbomachinery*, 115.

Dib, R., Alayli, Y., and Wagstaff, P. (2004). A broadband amplitude-modulated fibre optic vibrometer with nanometric accuracy. *Measurement*, 35.

Dietz, G., Schewe, G., and Mai, H. (2006). Amplification and amplitude limitation of heave/pitch limit-cycle oscillations close to the transonic dip. *J. of Fluids and Structures*, 22.

Dowell, E., editor (2005). *A modern course in aeroelasticity*. Kluwer, 4 edition.

Farhat, C., Lesoinne, M., and LeTallec, P. (1998). Load and motion transfer algorithms for fluid/structure interaction problems with non-matching discrete interfaces: momentum and energy conservation, optimal discretization and application to aeroelasticity. *Computer methods in applied mechanics and engineering*, 157.

Ferrand, P., Boudet, J., and Caro, J. (2006). Analysis of urans and les capabilities to predict vortex shedding for rods and turbines. In Hall, K., Kielb, R., and Thomas, J., editors, *Unsteady Aerodynamics, Aeroacoustics and Aeroelasticity of Turbomachines*. Springer.

Gallego-Garrido, J., Dimitriadis, G., and Wright, J. (2007). A class of methods for the analysis of blade tip timing data from bladed assemblies undergoing simultaneous resonances - part 1: theoretical development. *Int. J. of Rotating Machinery*, 2007. Article ID 27247.

Gill, J., Capece, V., and Fost, R. (2004). Experimental methods applied in a study of stall flutter in an axial flow fan. *Shock and vibration*, 11.

Goldstein, M., Braun, W., and Adamczyk, J. (1977). Unsteady flow in a supersonic cascade with strong in-passage shocks. *J. Fluid Mech.*, 83.

Gomes, J. and Lienhart, H. (2006). *Fluid-Structure Interaction*, volume 53, chapter Experimental Study on a Fluid-Structure Interaction Reference Test Case. Springer.

Gorrell, S. and Copenhaver, W. (2006). Dpiv measurements of the flow field between a transonic rotor and an upstream stator. In Hall, K., Kielb, R., and Thomas, J., editors, *Unsteady Aerodynamics, Aeroacoustics and Aeroelasticity of Turbomachines*. Springer.

Grüber, B. and Carstens, V. (2001). The impact of viscous effects on the aerodynamic damping of vibrating transonic compressor blades - a numerical study. *J. of Turbomachinery*, 123.

Hall, K. and Ekici, K. (2005). Multistage coupling for unsteady flows in turbomachinery. *AIAA*, 43(3).

Hall, K., Thomas, J., and Clark, W. (2002). Computation of unsteady nonlinear flows in cascades using a harmonic balance technique. *AIAA*, 40(5).

Harris, C. and Piersol, A. (2002). *Harris' Shock and Vibration Handbook*. McGraw-Hill, fifth edition.

Heath, S. (2000). A new technique for identifying synchronous resonances using tip-timing. *J. Gas Turbines and Power*, 122.

Heath, S. and Imregun, M. (1998). A survey of blade tip-timing measurement techniques for turbomachinery vibration. *J. Gas Turbines and Power*, 120.

Hild, F. and Roux, S. (2006). Digital image correlation: from displacement measurement to identification of elastic properties - a review. *Strain*, 42.

Hoying, D., Tan, C., Vo, H., and Greitzer, E. (1999). Role of blade passage flow structures in axial compressor rotating stall inception. *Journal of Turbomachinery*, 121.

Japikse, D. and Baines, N. (1994). *Introduction to Turbomachinery*. Concepts ETI.

Kielb, J. and Abhari, R. (2003). Experimental study of aerodynamic and structural damping in a full scale rotating turbine. *J. Gas Turbines and Power*, 125.

Kielb, J., Abhari, R., and Dunn, M. (2001). Experimental and numerical study of forced response in a full-scale rotating turbine. 2001-GT-0263.

Kobayashi, H. (1990). Annular cascade study of low back-pressure supersonic fan blade flutter. *Journal of turbomachinery*, 112.

Lawson, C. and Ivey, P. (2005). Turbomachinery blade vibration amplitude measurement through tip timing with capacitance tip clearance probes. *Sensors and Actuators*, 118.

Lee, B. (2001). Self-sustained shock oscillations on airfoils at transonic speeds. *Progress in Aerospace Sciences*, 37.

Liu, T., Cattafesta, L., and Radeztsky, R. (2000). Photogrammetry applied to wind-tunnel testing. *AIAA*, 38(6).

Marshall, J. and Imregun, M. (1996). A review of aeroelasticity methods with emphasis on turbomachinery applications. *J. of fluids and structures*, 10.

Mikrut, P., Bennington, M., Morris, S., and Cameron, J. (2010). Blade image velocimetry: development and uncertainty analysis. *Meas. Sci. Tech.*, 21.

Pappa, R., Black, J., Blandino, J., Jones, T., Danehy, P., and Dorrington, A. (2003). Dot-projection photogrammetry and videogrammetry of gossamer space structures. *J. Spacecraft and Rockets*, 40(6).

Platzer, M. and Carta, F., editors (1987). *AGARD manual on Aeroelasticity in axial-flow turbomachines. Volume 1: unsteady turbomachinery aerodynamics*. NATO. AGARDograph No. 298.

Platzer, M. and Carta, F., editors (1988). *AGARD manual on aeroelasticity in axial-flow turbomachines. Volume 2: structural dynamics and aeroelasticity*. NATO. AGARDograph No. 298.

Raffel, M., Willert, C., Wereley, S., and Kompenhans, J. (2007). *Particle Image Velocimetry : A Practical Guide*. Springer, 2 edition.

Sanders, A., Hassan, K., and Rabe, D. (2004). Experimental and numerical study of stall flutter in a transonic low-aspect ratio fan blisk. *Journal of Turbomachinery*, 126.

Schewe, G., Mai, H., and Dietz, G. (2003). Nonlinear effects in transonic flutter with emphasis on manifestations of limit cycle oscillations. *J. of Fluids and Structures*, 18.

Sieverding, C., Arts, T., Dénos, R., and Brouckaert, J.-F. (2000). Measurement techniques for unsteady flows in turbomachines. *Experiments in fluids*, 28.

Srinivasan, A. (1997). Flutter and resonant vibration characteristics of engine blades. *Journal of engineering for gas turbines and power*, 119.

Thermann, H. and Niehuis, R. (2006). Unsteady navier-stokes simulation of a transonic flutter cascade near-stall conditions applying algebraic transition models. *J. of Turbomachinery*, 128.

Tropea, C., Yarin, A., and Foss, J., editors (2007). *Springer handbook of experimental fluid mechanics*. Springer.

Vahdati, M., Syama, A., Marshall, J., and Imregun, M. (2001). Mechanisms and prediction methods for fan blade stall flutter. *J. Propulsion and Power*, 17(5).

Vandiver, J., Dunwoody, A., Campbell, R., and Cook, M. (1982). A mathematical basis for the random decrement vibration signature analysis technique. *J. Mechanical Design*, 104.

Verdon, J. and Caspar, J. (1984). A linearized unsteady aerodynamic analysis for transonic cascades. *J. Fluid Mech.*, 149.

Walker, S. (1997). *Experiments characterizing nonlinear shear layer dynamics in a supersonic rectangular jet undergoing screech*. Dissertation, The University of Notre Dame.

Wernet, M. (1997). Piv for turbomachinery applications. Technical Memo 107525, NASA.

Westerweel, J. (2000). Theoretical analysis of the measurement precision in particle image velocimetry. *Exp. in Fluids*, 29(7).

Yamasaki, M., Isogai, K., Uchida, T., and Yukima, I. (2004). Shock-stall flutter of a two-dimensional airfoil. *AIAA*, 42.

Zellinski, M. and Ziller, G. (2000). Noncontact vibration measurements on compressor rotor blades. *Meas. Sci. Tech.*, 6.

A DERIVATION OF THE STATISTIC τ

This section present the details of the simplification of the statistic

$$\tau \equiv \frac{1}{N}\sum_{n=1}^{s}\frac{1}{M-1}\sum_{i=1}^{M}\left(\boldsymbol{\Upsilon}-\mathbf{1}\frac{1}{M}\sum_{i=1}^{M}\boldsymbol{\Upsilon}\right)\left(\boldsymbol{\Upsilon}^{\mathrm{T}}-\frac{1}{M}\left(\sum_{i=1}^{M}\boldsymbol{\Upsilon}^{\mathrm{T}}\right)\mathbf{1}^{\mathrm{T}}\right), \tag{52}$$

where $\boldsymbol{\Upsilon}$ is an $[M\times N]$ matrix of the ensemble of observed tip velocities $\boldsymbol{\mathcal{V}}$,

$$\begin{aligned}\boldsymbol{\Upsilon} &\equiv \left[\begin{array}{ccccc}\boldsymbol{\mathcal{V}}(t_1) & \boldsymbol{\mathcal{V}}(t_2) & \boldsymbol{\mathcal{V}}(t_3) & \cdots & \boldsymbol{\mathcal{V}}(t_N)\end{array}\right] = \boldsymbol{\Phi}\boldsymbol{\xi}+\boldsymbol{\eta}^{\mathrm{T}}, &(53)\\ &= \sum_{p=1}^{q}\left([\boldsymbol{\Phi}]_{(i,p)}\,[\boldsymbol{\xi}]_{(p,n)}\right)+[\boldsymbol{\eta}^{\mathrm{T}}]_{(i,n)}\\ \boldsymbol{\xi} &\equiv \left[\begin{array}{ccccc}\boldsymbol{\zeta}(t_1) & \boldsymbol{\zeta}(t_2) & \boldsymbol{\zeta}(t_3) & \cdots & \boldsymbol{\zeta}(t_N)\end{array}\right], &(54)\end{aligned}$$

and $\boldsymbol{\Phi}$ is an $[M\times q]$ matrix whose columns represent the chordwise shape of the tip projection of a mode of vibration for a cantilevered blade. $\boldsymbol{\zeta}(t)$ is an $[q\times 1]$ vector of time-varying modal amplitudes and $\boldsymbol{\eta}$ is an $[N\times M]$ matrix of additive noise. Note that $\mathbf{1}$ is a $[M\times 1]$ vector whose elements are equal to 1. This is included to make the dimensions of the matrices which compose equation 52 consistent. **It will be assumed that the noise is zero-mean, Gaussian and statistically independent of both $\boldsymbol{\zeta}$ (and consequently $\boldsymbol{\xi}$) and $\boldsymbol{\Phi}$. Furthermore, $\boldsymbol{\zeta}$ will be assumed zero mean** (IE $\boldsymbol{\zeta}(t_n)_p$ is sinusoidal with respect to t_n). **Finally, η is assumed ergodic and IID[§]along the chord.**

Consider the chordwise average of $\boldsymbol{\Upsilon}$,

$$\begin{aligned}\frac{1}{M}\sum_{i=1}^{M}\boldsymbol{\Upsilon} &= \frac{1}{M}\sum_{i=1}^{M}\left[\sum_{p=1}^{q}\left([\boldsymbol{\Phi}]_{(i,p)}\,[\boldsymbol{\xi}]_{(p,n)}\right)+[\eta]_{(i,n)}\right]\\ &= \sum_{p=1}^{q}\left(\frac{1}{M}\sum_{i=1}^{M}[\boldsymbol{\Phi}]_{(i,p)}\right)[\boldsymbol{\xi}]_{(p,n)}+\frac{1}{M}\sum_{i=1}^{M}[\boldsymbol{\eta}]_{(i,n)}\\ &= \sum_{p=1}^{q}[\boldsymbol{\mu}_{\boldsymbol{\phi}}]_{(1,p)}\,[\boldsymbol{\xi}]_{(p,n)}\\ \frac{1}{M}\sum_{i=1}^{M}\boldsymbol{\Upsilon} &= \boldsymbol{\mu}_{\boldsymbol{\phi}}\boldsymbol{\xi} &(55)\end{aligned}$$

where

$$[\boldsymbol{\mu}_{\boldsymbol{\phi}}]_{(1,p)} \equiv \frac{1}{M}\sum_{i=1}^{M}[\boldsymbol{\Phi}]_{(i,p)}, \tag{56}$$

is the chordwise average of the p^{th} mode shape. Note that the chordwise average of $\boldsymbol{\Upsilon}$ yields a vector of dimension $[1\times N]$, hence the necessity of pre-multiplying by the $[M\times 1]$ vector $\mathbf{1}$. Using this result, equation 52 can be expressed as

$$\tau \equiv \frac{1}{N}\sum_{n=1}^{s}\frac{1}{M-1}\sum_{i=1}^{M}\left(\boldsymbol{\Phi}\boldsymbol{\xi}+\boldsymbol{\eta}^{\mathrm{T}}-\mathbf{1}\boldsymbol{\mu}_{\boldsymbol{\phi}}\boldsymbol{\xi}\right)\left(\boldsymbol{\xi}^{\mathrm{T}}\,\boldsymbol{\Phi}^{\mathrm{T}}+\boldsymbol{\eta}-\boldsymbol{\xi}^{\mathrm{T}}\,\boldsymbol{\mu}_{\boldsymbol{\phi}}{}^{\mathrm{T}}\,\mathbf{1}^{\mathrm{T}}\right)$$

[§]Independent and Identically Distributed.

It can be observed that there are 9 terms which contribute to τ, but only 6 are distinct. Three terms are matrix transposes which upon summation contribute identically to τ as their un-transposed counterparts. The 6 distinct terms are

1. $\frac{1}{N}\sum_{n=1}^{s}\frac{1}{M-1}\sum_{i=1}^{M}\boldsymbol{\Phi}\boldsymbol{\xi}\boldsymbol{\xi}^{\mathrm{T}}\,\boldsymbol{\Phi}^{\mathrm{T}}$
2. $\frac{1}{N}\sum_{n=1}^{s}\frac{1}{M-1}\sum_{i=1}^{M}\boldsymbol{\Phi}\boldsymbol{\xi}\boldsymbol{\eta}$
3. $-\frac{1}{N}\sum_{n=1}^{s}\frac{1}{M-1}\sum_{i=1}^{M}\boldsymbol{\Phi}\boldsymbol{\xi}\boldsymbol{\xi}^{\mathrm{T}}\,\boldsymbol{\mu_\phi}^{\mathrm{T}}\,\mathbf{1}^{\mathrm{T}}$
4. $\frac{1}{N}\sum_{n=1}^{s}\frac{1}{M-1}\sum_{i=1}^{M}\boldsymbol{\eta}^{\mathrm{T}}\,\boldsymbol{\eta}$
5. $\frac{1}{N}\sum_{n=1}^{s}\frac{1}{M-1}\sum_{i=1}^{M}\boldsymbol{\eta}^{\mathrm{T}}\,\boldsymbol{\xi}^{\mathrm{T}}\,\boldsymbol{\mu_\phi}^{\mathrm{T}}\,\mathbf{1}^{\mathrm{T}}$
6. $\frac{1}{N}\sum_{n=1}^{s}\frac{1}{M-1}\sum_{i=1}^{M}\mathbf{1}\boldsymbol{\mu_\phi}\boldsymbol{\xi}\boldsymbol{\xi}^{\mathrm{T}}\,\boldsymbol{\mu_\phi}^{\mathrm{T}}\,\mathbf{1}^{\mathrm{T}}$

The three non-distinct terms correspond to items 2, 3 and 5. The simplification of each term will now be considered in the following sections.

Term 1

The first term can be expressed as

$$\begin{aligned}
&\frac{1}{N}\sum_{n=1}^{s}\frac{1}{M-1}\sum_{i=1}^{M}\left(\sum_{p=1}^{q}[\boldsymbol{\Phi}]_{(i,p)}\,[\boldsymbol{\xi}]_{(p,n)}\,[\boldsymbol{\xi}^{\mathrm{T}}]_{(n,p)}\,[\boldsymbol{\Phi}^{\mathrm{T}}]_{(p,i)}\right)\\
&=\frac{1}{M-1}\sum_{i=1}^{M}\left(\sum_{p=1}^{q}[\boldsymbol{\Phi}]_{(i,p)}\,\frac{1}{N}\sum_{n=1}^{s}\left([\boldsymbol{\xi}]_{(p,n)}\,[\boldsymbol{\xi}^{\mathrm{T}}]_{(n,p)}\right)[\boldsymbol{\Phi}^{\mathrm{T}}]_{(p,i)}\right)\\
&=\frac{1}{M-1}\sum_{i=1}^{M}\left(\sum_{p=1}^{q}[\boldsymbol{\Phi}]_{(i,p)}\,\frac{1}{N}\sum_{n=1}^{s}\left([\boldsymbol{\xi}]_{(p,n)}\,[\boldsymbol{\xi}^{\mathrm{T}}]_{(n,p)}\right)[\boldsymbol{\Phi}^{\mathrm{T}}]_{(p,i)}\right)
\end{aligned}$$

Now, the term $\frac{1}{N}\sum_{n=1}^{s}\left([\boldsymbol{\xi}]_{(p,n)}\,[\boldsymbol{\xi}^{\mathrm{T}}]_{(n,p)}\right)$ has diagonal elements which are equal to the mean-squared amplitude of $\boldsymbol{\zeta}$. The assumption that $\boldsymbol{\zeta}$ was zero mean implies that the mean-squared amplitude is equal to the **biased** estimate of the variance of $\boldsymbol{\zeta}$. **It is assumed that N is sufficiently large such that this bias error is small (IE $N-1\approx N$).** Now, the formulation used in the definition of τ was such that summation over p extracts the diagonal of this term. As such, the notation

$$\left[\boldsymbol{\sigma}_{\boldsymbol{\zeta}}^{\mathbf{2}}\right]_{(p,p)}\equiv\frac{1}{N}\sum_{n=1}^{s}\left([\boldsymbol{\xi}]_{(p,n)}\,[\boldsymbol{\xi}^{\mathrm{T}}]_{(n,p)}\right),\tag{57}$$

will be used. This allows for further simplification,

$$\begin{aligned}
&\frac{1}{N}\sum_{n=1}^{s}\frac{1}{M-1}\sum_{i=1}^{M}\left(\sum_{p=1}^{q}[\boldsymbol{\Phi}]_{(i,p)}\,[\boldsymbol{\xi}]_{(p,n)}\,[\boldsymbol{\xi}^{\mathrm{T}}]_{(n,p)}\,[\boldsymbol{\Phi}^{\mathrm{T}}]_{(p,i)}\right)\\
&\qquad=\frac{1}{M-1}\sum_{i=1}^{M}\left(\sum_{p=1}^{q}[\boldsymbol{\Phi}]_{(i,p)}\left[\boldsymbol{\sigma}_{\boldsymbol{\zeta}}^{\mathbf{2}}\right]_{(p,p)}[\boldsymbol{\Phi}^{\mathrm{T}}]_{(p,i)}\right).
\end{aligned}$$

Expanding the summation over p yields

$$\begin{aligned}\frac{1}{M-1}\sum_{i=1}^{M} \quad & \left\{ [\mathbf{\Phi}]_{(i,1)} \left[\boldsymbol{\sigma}_{\boldsymbol{\zeta}}^{\mathbf{2}}\right]_{(1,1)} [\mathbf{\Phi}^{\mathrm{T}}]_{(1,i)} \right\} \\ & + \left\{ [\mathbf{\Phi}]_{(i,2)} \left[\boldsymbol{\sigma}_{\boldsymbol{\zeta}}^{\mathbf{2}}\right]_{(2,2)} [\mathbf{\Phi}^{\mathrm{T}}]_{(2,i)} \right\} \\ & + \left\{ [\mathbf{\Phi}]_{(i,3)} \left[\boldsymbol{\sigma}_{\boldsymbol{\zeta}}^{\mathbf{2}}\right]_{(3,3)} [\mathbf{\Phi}^{\mathrm{T}}]_{(3,i)} \right\} \\ & + \dots \end{aligned}$$

which is equivalent to

$$\begin{aligned} & \left[\boldsymbol{\sigma}_{\boldsymbol{\zeta}}^{\mathbf{2}}\right]_{(1,1)} \left\{ \frac{1}{M-1}\sum_{i=1}^{M} [\mathbf{\Phi}]_{(i,1)} [\mathbf{\Phi}^{\mathrm{T}}]_{(1,i)} \right\} \\ + & \left[\boldsymbol{\sigma}_{\boldsymbol{\zeta}}^{\mathbf{2}}\right]_{(2,2)} \left\{ \frac{1}{M-1}\sum_{i=1}^{M} [\mathbf{\Phi}]_{(i,2)} [\mathbf{\Phi}^{\mathrm{T}}]_{(2,i)} \right\} \\ + & \left[\boldsymbol{\sigma}_{\boldsymbol{\zeta}}^{\mathbf{2}}\right]_{(3,3)} \left\{ \frac{1}{M-1}\sum_{i=1}^{M} [\mathbf{\Phi}]_{(i,3)} [\mathbf{\Phi}^{\mathrm{T}}]_{(3,i)} \right\} \\ & + \dots \end{aligned}$$

The terms inside the braces can be recognized as

$$\left\{ \frac{1}{M-1}\sum_{i=1}^{M} [\mathbf{\Phi}]_{(i,p)} [\mathbf{\Phi}^{\mathrm{T}}]_{(p,i)} \right\} = \left[\boldsymbol{\sigma}_{\mathbf{\Phi}}^{\mathbf{2}}\right]_{p} + \frac{M}{M-1} [\boldsymbol{\mu}_{\boldsymbol{\phi}}]_{p}^{2} \tag{58}$$

where $\left[\boldsymbol{\sigma}_{\mathbf{\Phi}}^{\mathbf{2}}\right]_{p}$ is the unbiased estimation of the chordwise variance of the p^{th} mode shape, and $[\boldsymbol{\mu}_{\boldsymbol{\phi}}]_{p}^{2}$ is the square of the chordwise average of the p^{th} mode shape (cf equation 56). To make the dimensions consistent, it will be assumed that $\left[\boldsymbol{\sigma}_{\mathbf{\Phi}}^{\mathbf{2}}\right]$ is a $[q \times 1]$ vector. Using this relation,

$$\begin{aligned} & \left[\boldsymbol{\sigma}_{\boldsymbol{\zeta}}^{\mathbf{2}}\right]_{(1,1)} \left\{ \left[\boldsymbol{\sigma}_{\mathbf{\Phi}}^{\mathbf{2}}\right]_{1} + \frac{M}{M-1} [\boldsymbol{\mu}_{\boldsymbol{\phi}}]_{1}^{2} \right\} \\ & + \left[\boldsymbol{\sigma}_{\boldsymbol{\zeta}}^{\mathbf{2}}\right]_{(2,2)} \left\{ \left[\boldsymbol{\sigma}_{\mathbf{\Phi}}^{\mathbf{2}}\right]_{2} + \frac{M}{M-1} [\boldsymbol{\mu}_{\boldsymbol{\phi}}]_{2}^{2} \right\} \\ & + \left[\boldsymbol{\sigma}_{\boldsymbol{\zeta}}^{\mathbf{2}}\right]_{(3,3)} \left\{ \left[\boldsymbol{\sigma}_{\mathbf{\Phi}}^{\mathbf{2}}\right]_{3} + \frac{M}{M-1} [\boldsymbol{\mu}_{\boldsymbol{\phi}}]_{3}^{2} \right\}, \\ = & \sum_{p=1}^{q} \left[\boldsymbol{\sigma}_{\boldsymbol{\zeta}}^{\mathbf{2}}\right]_{(p,p)} \left(\left(\boldsymbol{\sigma}_{\mathbf{\Phi}}^{\mathbf{2}}\right)_{(p,1)} + \frac{M}{M-1} [\boldsymbol{\mu}_{\boldsymbol{\phi}}]_{(p,1)}^{2} \right). \end{aligned}$$

Therefore, the first term can be expressed as

$$\begin{aligned} & \frac{1}{N}\sum_{n=1}^{s} \frac{1}{M}\sum_{i=1}^{M} \left(\sum_{p=1}^{q} [\mathbf{\Phi}]_{(i,p)} [\boldsymbol{\xi}]_{(p,n)} [\boldsymbol{\xi}^{\mathrm{T}}]_{(n,p)} [\mathbf{\Phi}^{\mathrm{T}}]_{(p,i)} \right) \\ & \qquad = \sum_{p=1}^{q} \left[\boldsymbol{\sigma}_{\boldsymbol{\zeta}}^{\mathbf{2}}\right]_{(p,p)} \left(\left[\boldsymbol{\sigma}_{\mathbf{\Phi}}^{\mathbf{2}}\right]_{p} + \frac{M}{M-1} [\boldsymbol{\mu}_{\boldsymbol{\phi}}]_{p}^{2} \right) \end{aligned} \tag{59}$$

It should be noted that equation 59 yields a scalar quantity.

Term 2

The second term is

$$\frac{1}{N}\sum_{n=1}^{s}\frac{1}{M-1}\sum_{i=1}^{M}\left(\sum_{p=1}^{q}[\boldsymbol{\Phi}]_{(i,p)}\,[\boldsymbol{\xi}]_{(p,n)}\right)[\boldsymbol{\eta}^{\mathrm{T}}]_{(n,i)}\,. \tag{60}$$

Expanding the summation over p yields

$$\frac{1}{N}\sum_{n=1}^{s}\frac{1}{M-1}\sum_{i=1}^{M}\left\{[\boldsymbol{\Phi}]_{(i,1)}\,[\boldsymbol{\xi}]_{(1,n)}+[\boldsymbol{\Phi}]_{(i,2)}\,[\boldsymbol{\xi}]_{(2,n)}+\dots\right\}[\boldsymbol{\eta}^{\mathrm{T}}]_{(n,i)}$$

Exchanging the order of summation yields

$$\frac{1}{M-1}\sum_{i=1}^{M}\left\{[\boldsymbol{\Phi}]_{(i,1)}\left(\frac{1}{N}\sum_{n=1}^{s}[\boldsymbol{\xi}]_{(1,n)}\,[\boldsymbol{\eta}^{\mathrm{T}}]_{(n,i)}\right)+[\boldsymbol{\Phi}]_{(i,2)}\left(\frac{1}{N}\sum_{n=1}^{s}[\boldsymbol{\xi}]_{(2,n)}\,[\boldsymbol{\eta}^{\mathrm{T}}]_{(n,i)}\right)+\dots\right\}$$

Note that the term $\frac{1}{N}\sum_{n=1}^{s}[\boldsymbol{\xi}]_{(p,n)}\,[\boldsymbol{\eta}^{\mathrm{T}}]_{(n,i)}$ is the ensemble expected value of the product of the time-varying modal amplitude ζ and additive noise η. Recall that the noise η and the modal amplitude ζ were assumed to be statistically independent. Furthermore, it was assumed that η was zero mean. Therefore, this quantity is zero for all values of p. Hence,

$$\frac{1}{N}\sum_{n=1}^{s}\frac{1}{M-1}\sum_{i=1}^{M}\left(\sum_{p=1}^{q}[\boldsymbol{\Phi}]_{(i,p)}\,[\boldsymbol{\xi}]_{(p,n)}\right)[\boldsymbol{\eta}^{\mathrm{T}}]_{(n,i)}=0 \tag{61}$$

Term 3

The third term is

$$\begin{aligned}
&-\frac{1}{N}\sum_{n=1}^{s}\frac{1}{M-1}\sum_{i=1}^{M}\boldsymbol{\Phi}\boldsymbol{\xi}\boldsymbol{\xi}^{\mathrm{T}}\,\boldsymbol{\mu_\phi}^{\mathrm{T}}\,\mathbf{1}^{\mathrm{T}}\\
&=-\frac{1}{N}\sum_{n=1}^{s}\frac{1}{M-1}\sum_{i=1}^{M}\sum_{p=1}^{q}[\boldsymbol{\Phi}]_{(i,p)}\,[\boldsymbol{\xi}]_{(p,n)}\,[\boldsymbol{\xi}^{\mathrm{T}}]_{(n,p)}\,[\boldsymbol{\mu_\phi}^{\mathrm{T}}]_{(p,1)}\,[\mathbf{1}^{\mathrm{T}}]_{1,i}\\
&=-\frac{1}{M-1}\sum_{i=1}^{M}\sum_{p=1}^{q}[\boldsymbol{\Phi}]_{(i,p)}\left(\frac{1}{N}\sum_{n=1}^{s}[\boldsymbol{\xi}]_{(p,n)}\,[\boldsymbol{\xi}^{\mathrm{T}}]_{(n,p)}\right)[\boldsymbol{\mu_\phi}^{\mathrm{T}}]_{(p,1)}\,[\mathbf{1}^{\mathrm{T}}]_{1,i}\\
&=-\frac{1}{M-1}\sum_{i=1}^{M}\sum_{p=1}^{q}[\boldsymbol{\Phi}]_{(i,p)}\left[\boldsymbol{\sigma}_{\boldsymbol{\zeta}}^{\mathbf{2}}\right]_{(p,p)}[\boldsymbol{\mu_\phi}^{\mathrm{T}}]_{(p,1)}\\
&=-\sum_{p=1}^{q}\left[\boldsymbol{\sigma}_{\boldsymbol{\zeta}}^{\mathbf{2}}\right]_{(p,p)}\frac{1}{M-1}\sum_{i=1}^{M}[\boldsymbol{\Phi}]_{(i,p)}\,[\boldsymbol{\mu_\phi}^{\mathrm{T}}]_{(p,1)}\,[\mathbf{1}^{\mathrm{T}}]_{1,i}\\
&=-\frac{M}{M-1}\sum_{p=1}^{q}\left[\boldsymbol{\sigma}_{\boldsymbol{\zeta}}^{\mathbf{2}}\right]_{(p,p)}[\boldsymbol{\mu_\phi}]_{(p,1)}^{2}
\end{aligned} \tag{62}$$

Term 4

The fourth term is

$$\frac{1}{N}\sum_{n=1}^{s}\frac{1}{M-1}\sum_{i=1}^{M}\boldsymbol{\eta}^{\mathrm{T}}\,\boldsymbol{\eta}$$

which can be recognized as the ensemble average of the chordwise mean-squared value of the noise, η. This is equivalent to the chordwise variance of the noise, which, because of the assumption of ergodicity is equal to σ_η^2. Thus, the fifth term is

$$\frac{1}{N}\sum_{n=1}^{s}\frac{1}{M-1}\sum_{i=1}^{M}\left(\left[\boldsymbol{\eta}^{\mathrm{T}}\right]_{(i,n)}\left[\boldsymbol{\eta}\right]_{(n,i)}\right) = \sigma_\eta^2. \tag{63}$$

Term 5

The fifth term is

$$\frac{1}{N}\sum_{n=1}^{s}\frac{1}{M}\sum_{i=1}^{M}\boldsymbol{\eta}^{\mathrm{T}}\,\boldsymbol{\xi}^{\mathrm{T}}\,\boldsymbol{\mu_\phi}^{\mathrm{T}}\,\mathbf{1}^{\mathrm{T}} = 0 \tag{64}$$

which can be deduced in a similar manner as that presented for the second term.

Term 6

the sixth term is

$$\begin{aligned}
&\frac{1}{N}\sum_{n=1}^{s}\frac{1}{M-1}\sum_{i=1}^{M}\mathbf{1}\boldsymbol{\mu_\phi}\boldsymbol{\xi}\boldsymbol{\xi}^{\mathrm{T}}\,\boldsymbol{\mu_\phi}^{\mathrm{T}}\,\mathbf{1}^{\mathrm{T}}\\
&= \frac{1}{N}\sum_{n=1}^{s}\frac{1}{M-1}\sum_{i=1}^{M}\left(\sum_{p=1}^{q}\left[\mathbf{1}\right]_{(i,1)}\left[\boldsymbol{\mu_\phi}\right]_{(1,p)}\left[\boldsymbol{\xi}\right]_{(p,n)}\left[\boldsymbol{\xi}^{\mathrm{T}}\right]_{(n,p)}\left[\boldsymbol{\mu_\phi}^{\mathrm{T}}\right]_{(p,1)}\left[\mathbf{1}^{\mathrm{T}}\right]_{(1,i)}\right)\\
&= \frac{1}{M-1}\sum_{i=1}^{M}\sum_{p=1}^{q}\left[\mathbf{1}\right]_{(i,1)}\left[\boldsymbol{\mu_\phi}\right]_{(1,p)}\left(\frac{1}{N}\sum_{n=1}^{s}\left[\boldsymbol{\xi}\right]_{(p,n)}\left[\boldsymbol{\xi}^{\mathrm{T}}\right]_{(n,p)}\right)\left[\boldsymbol{\mu_\phi}^{\mathrm{T}}\right]_{(p,1)}\left[\mathbf{1}^{\mathrm{T}}\right]_{(1,i)}\\
&= \frac{1}{M-1}\sum_{i=1}^{M}\sum_{p=1}^{q}\left[\mathbf{1}\right]_{(i,1)}\left[\boldsymbol{\mu_\phi}\right]_{(1,p)}\left[\boldsymbol{\sigma_\zeta^2}\right]_{(p,p)}\left[\boldsymbol{\mu_\phi}^{\mathrm{T}}\right]_{(p,1)}\left[\mathbf{1}^{\mathrm{T}}\right]_{(1,i)}\\
&= \frac{1}{M-1}\sum_{i=1}^{M}\sum_{p=1}^{q}\left[\boldsymbol{\sigma_\zeta^2}\right]_{(p,p)}\left[\mathbf{1}\right]_{(i,1)}\left[\boldsymbol{\mu_\phi}\right]_{(1,p)}\left[\boldsymbol{\mu_\phi}^{\mathrm{T}}\right]_{(p,1)}\left[\mathbf{1}^{\mathrm{T}}\right]_{(1,i)}\\
&= \sum_{p=1}^{q}\left[\boldsymbol{\sigma_\zeta^2}\right]_{(p,p)}\frac{1}{M-1}\sum_{i=1}^{M}\left[\mathbf{1}\right]_{(i,1)}\left[\boldsymbol{\mu_\phi}\right]_{(1,p)}\left[\boldsymbol{\mu_\phi}^{\mathrm{T}}\right]_{(p,1)}\left[\mathbf{1}^{\mathrm{T}}\right]_{(1,i)}\\
&= \frac{M}{M-1}\sum_{p=1}^{q}\left[\boldsymbol{\sigma_\zeta^2}\right]_{(p,p)}\left[\boldsymbol{\mu_\phi}\right]_{(p,1)}^{2}
\end{aligned} \tag{65}$$

Final Simplification

Using equations 59 - 65, the statistic τ can be simplified as

$$\begin{aligned}
\tau &\equiv \frac{1}{N}\sum_{n=1}^{s}\frac{1}{M}\sum_{i=1}^{M}\left(\boldsymbol{\Upsilon}-\frac{1}{M}\sum_{i=1}^{M}\boldsymbol{\Upsilon}\right)\left(\boldsymbol{\Upsilon}^{\mathrm{T}}-\frac{1}{M}\sum_{i=1}^{M}\boldsymbol{\Upsilon}^{\mathrm{T}}\right) \\
&= \left\{\sum_{p=1}^{q}\left[\boldsymbol{\sigma}_{\boldsymbol{\zeta}}^{\mathbf{2}}\right]_{(p,p)}\left(\left[\boldsymbol{\sigma}_{\boldsymbol{\Phi}}^{\mathbf{2}}\right]_{p}+\frac{M}{M-1}\left[\boldsymbol{\mu}_{\boldsymbol{\phi}}\right]_{p}^{2}\right)\right\} \\
&\quad +2\left\{-\frac{M}{M-1}\sum_{p=1}^{q}\left[\boldsymbol{\sigma}_{\boldsymbol{\zeta}}^{\mathbf{2}}\right]_{(p,p)}\left[\boldsymbol{\mu}_{\boldsymbol{\phi}}\right]_{(p,1)}^{2}\right\}+\left\{\sigma_{\eta}^{2}\right\} \\
&\quad +\left\{\frac{M}{M-1}\sum_{p=1}^{q}\left[\boldsymbol{\sigma}_{\boldsymbol{\zeta}}^{\mathbf{2}}\right]_{(p,p)}\left[\boldsymbol{\mu}_{\boldsymbol{\phi}}\right]_{(p,1)}^{2}\right\} \\
&= \sum_{p=1}^{q}\left[\boldsymbol{\sigma}_{\boldsymbol{\zeta}}^{\mathbf{2}}\right]_{(p,p)}\left[\boldsymbol{\sigma}_{\boldsymbol{\Phi}}^{\mathbf{2}}\right]_{p}+\sigma_{\eta}^{2} \\
&= \boldsymbol{\sigma}_{\boldsymbol{\zeta}}^{\mathbf{2}}\boldsymbol{\sigma}_{\boldsymbol{\Phi}}^{\mathbf{2}}+\sigma_{\eta}^{2} \qquad (66)
\end{aligned}$$